Département d'Astrophysique,
Géophysique et Océanographie
Université de Liège
Liège, Belgium

Année 2011-2012

Master Thesis

Optimization and application of a LOCI-type reduction pipeline to detect exoplanets

Author: Valentin Christiaens

Tutor: Dimitri Mawet

Co-Tutor: Olivier Absil

Reading committee: Serge Habraken
Jean Surdej
Jacques Verly

vchristiaens@student.ulg.ac.be

August 15, 2012

Abstract

Adaptive optics and coronagraphy are complementary key resources required to reach both *resolution* and *contrast* conditions for direct detection of exoplanets. However, instruments are never perfect, so that swarms of bright *quasi-static speckles* close to the central star in the image do curb the detection of companions. This noise can be lowered either actively by better non-common path aberrations *calibrations* on the instrument acquiring the images - it was the way explored during my internship at ESO, or passively by appropriate combination of observing strategy and *data reduction* technique. Among the various strategies of differential imaging, stress is put on angular differential imaging (ADI), whose main idea is to take profit of pupil tracking to freeze the quasi-static speckles of both the telescope and the instrument. In order to optimize even further the suppression of quasi-static speckles, a data post-processing algorithm called LOCI (Locally Optimized Combination of Images) has been proposed by Lafrenière, Marois, et al. (2007). The personal contribution of this thesis is aimed at implementing a personalized version of LOCI, based on the existing code of Dimitri, endeavoring algorithmic optimization of its parameters, computation of contrast curves taking into account the extinction of the companion by LOCI, and compilation of all the required steps of data reduction, from basic treatment to optimized LOCI, in a unique IDL code. Finally, the last part of this work is devoted to the reduction of different sets of images acquired by VLT/NACO with this code, attempting to detect exoplanets around specific young stars known to possess a debris disk.

Résumé

L'optique adaptative et la coronagraphie sont des outils clefs et complémentaires pour atteindre les conditions de *résolution* et de *contraste* nécessaires à la détection directe de compagnons plantaires. Cependant, les instruments n'étant jamais parfaits, des tavelures quasi-statiques à proximité de l'étoile dans l'image gênent la détection de ces compagnons. La réduction des tavelures peut se faire à deux niveaux: d'une part via de meilleures calibrations des aberrations de chemin non-commun sur l'instrument (la voie suivie durant mon *stage en industrie*), et d'autre part, via la combinaison adéquate d'une stratégie d'observation et d'une technique de traitement des données. Parmi les méthodes d'imagerie différentielle, l'accent est mis sur l'imagerie différentielle angulaire (ADI), dont le principe consiste à tirer profit du suivi de la pupille pour figer les tavelures quasi-statiques du télescope et de l'instrument. Dans le but d'optimiser la suppression des tavelures, un algorithme de post-traitement des images appelé LOCI (Combinaison d'Images Localement Optimisée) fut proposé par Lafrenière, Marois, et al. (2007). L'apport personnel de ce travail consiste en une optimisation de la version classique de LOCI, avec diverses autres améliorations, et en la compilation de toutes les étapes de traitement d'images dans un seul et unique code écrit en langage IDL. Finalement, la dernière partie de ce mémoire se consacre à l'application de ce code au traitement de deux jeux de données acquis par l'instrument VLT/NACO, pour la détection d'exoplanètes autour d'étoiles jeunes possédant un disque de débris.

Acknowledgments

I profoundly acknowledge my tutor Dimitri Mawet[1] for all its wise advice and suggestions, its patience in answering all my questions and careful rereading. Since the subjects of both my master thesis and my internship at ESO were intricated, I also thank my insternship supervisors Julien Girard[2] and Jared O'Neal[3] for the good atmosphere that they spread during my stay at ESO.

I also express my gratefulness to Olivier Absil and Charles Hanot, who helped me at the very first steps of the procedure to get this internship. Without them, I would never have met my tutor. I also acknowledge Olivier for the help provided to install softwares that I required for this thesis and for its rereading as well.

I am also very grateful to my relatives (merci Luc pour ta relecture), friends and flatmates that helped me in keeping my motivation untouched, in particular all the students (and non-students) that I met while working at ESO.

Last but not least, I acknowledge ESO, and particularly Michael West, for allowing me to carry out both my internship and master thesis, thereby achieving such a rewarding experience. Also, I am very grateful to Paulina Jiron, for all the actions undertaken to help me recovering my notebook which contained key information concerning my master thesis.

This research has made extensive use of (1) NASA's Astrophysics Data System, (2) ViZieR and SIMBAD databases, operated at CDS (Strasbourg, France), (3) the NASA/IPAC/NExScI Star and Exoplanet Database, which is operated by the JPL, Caltech, under contract with NASA, (4) NASA's WISE All-sky data Release, (5) the Exoplanets Encyclopaedia maintained by J. Schneider (2012), (6) IDL for the implementation part of this work and (7) LaTeX for its practical development.

[1]Operation staff astronomer, NaCo and Vizir second instrument scientist.
[2]Operation staff astronomer, NaCo instrument scientist.
[3]Instrumentation Engineer, NaCo instrument responsible.

Contents

List of Figures

List of Tables

Acronyms

4QPM	Four Quadrants Phase Mask
(c-, p-, r-) ADI	(classical, pseudo, radial) Angular Differential Imaging
AO	Adaptive Optics
CDI	Coherent Differential Imaging
CONICA	COudé Near-Infrared CAmera (Imager and Spectrograph)
DIT	Detector Integration Time
DM	Deformable Mirror
FOV	Field of View
FS	Field Selector
FWHM	Full Width at Half Maximum
HAR	High Angular Resolution
HC	High Contrast
HST	Hubble Space Telescope
IFS	Integral Field Spectrograph
IWA	Inner-Working Angle
LOCI	Locally Optimized Combination of Images
d-LOCI	Damped LOCI
p-LOCI	Personalized version of LOCI
MS	Main Sequence
NaCo	NAos-COnica
NAOS	Nasmyth Adaptive Optics System
NCPA	Non-Common Path Aberrations
NGS	Natural Guide Star
OTF	Optical Transfer Function
PD	Phase Diversity
PMS	Pre-Main Sequence
PV	Peak-to-Valley
PSF	Point Spread Function
RDI	Reference star Differential Imaging
Rms	Root mean square
RON	Readout Noise
RS	Reference Slopes
RV	Radial Velocity
S/N	Signal to Noise
SDI	Spectral Differential Imaging
SPHERE	Spectro-Polarimetric High-contrast Exoplanet Research
TTM	Tip/Tilt Mirror
VLT	Very Large Telescope
WFS	Wavefront Sensor

Physical parameters

α_*	Astrometric position of the parent star (2D)
β	Angular separation between the planet and its parent star
$\phi(t)$	Orbital phase factor given by $\phi(t) = 1 - \sin i_p \sin(2\pi t/P)$
ω	Argument of periapsis of the orbit
a_*	Radius of the parent star's orbit (around the common center of mass with its planet)
a_p	Semi-major axis of the detected planet's orbit
d	Distance of the detected planet from the Solar System
D_T	Duration of the transit
e	Eccentricity of the orbit
i_p	Inclination of the detected planet's orbit, relative to the plane perpendicular to the line-of-sight to the object
i_{rot}	Inclination of the star rotation axis
K	Radial velocity of the parent star
L_*	Brightness of the parent star
L_p	Brightness of the detected planet
M_*	Mass of the parent star
$M_\oplus$	Earth mass
M_J	Jupiter mass
M_p	Mass of the detected planet
P	Orbital period of the detected planet
R_*	Radius of the parent star
$R_\oplus$	Earth radius
R_J	Jupiter raidus
R_p	Radius of the detected planet
t_*	Time of arrival of signals of the parent star
T_*	Temperature of the parent star
T_p	Temperature of the detected planet
V_R	Radial velocity of the parent star

Units and physical constants

AU	Astronomical Unit	$1.496 \cdot 10^{11}$ m
c	Speed of light	299,792,458 m/s
Gyr	Gigayear	10^9 year
kpc	Kilo-parsec	1000 pc
mas	Milli-arcsecond	10^{-3} arcsec
μas	Micro-arcsecond	10^{-6} arcsec
Ly	Lightyear	$9.461 \cdot 10^{15}$ m
Myr	Megayear	10^6 year
pc	Parsec	$3.086 \cdot 10^{16}$ m
px	Pixel	
Sr	Strehl ratio	

Introduction

Existence of other worlds is one of the oldest well formulated scientific question. Invention and improvement of both telescopes and observation techniques have yielded poor results but plentiful speculations for centuries. The discovery of the first extra-solar planets in the nineties has spawned a new and rapidly growing field. In total more than 6000 papers have been published regarding exoplanets during the last 15 years, conveying the considerable craze inspired by the vision of finding other Earths and perhaps other life. Up to July 13, 2012, 777 exoplanets (J. Schneider, 2012) have been detected, mainly by indirect methods but also by *direct imaging*. The specific subject of this master thesis takes place in the latter domain.

Different detection techniques enabled the discovery of exoplanets in different parameter ranges (mass, radius, distance to the star). Since recently, our Solar system was the only prototype stellar system, but the wide diversity found seem to indicate that it is in reality not a standard one. Whereas the radial velocity technique unveiled the existence of unexpected hot Jupiters, imaging revealed long-period planets such as Beta Pic b (Lagrange et al., 2009, 2010), HR8799 b,c,d and e (Marois, Macintosh, et al., 2008; Marois et al., 2010) and 1RXS J160929.1-210524 b (Lafrenière et al., 2008, 2010).

Direct imaging of exoplanets faces two main limitations: *resolution* and *contrast*, so that current methods enabling the discovery of exoplanets are qualified as *high-contrast* (hereafter HC) and *high angular resolution* (hereafter HAR). Detections occur in priority for companions at the outskirts of systems, from the outside-in as techniques improve. As one pushes inwards, central star stray light prevents the detection of any companion whose magnitude would be several orders fainter than the star. Recently formed companions are warmer. Their luminosity contrast ratio with respect to their host star is thus more favorable. Young stellar systems constitute thereby a preferential scientific niche for high-contrast imaging.

Characterization of statistically significant young extra-solar planetary systems (exoplanets and circumstellar disks) provides constraints on formation models of stellar systems. Elaboration of these formation models constitute currently the main goal of studying young systems. A recent example is the use of HR8799 giants in simulations that allowed the determination of their formation mechanism, which, according to Dodson-Robinson et al. (2009), appears to be gravitational instabilities in the circumstellar disk. Probing distant young stellar systems simultaneously helps us understanding the formation mechanisms of our own Solar system and its planets.

To probe more and more closer to the central star and solve the contrast issue, one needs to use coronagraphs. Coronagraphy was first invented by Bernard Lyot and was initially used to observe the Solar corona (Lyot, 1930). Nowadays, it designates any technique used to enhance contrast

in astrophysical scenes. Adaptive optics (hereafter AO) systems are necessary to improve as best as possible the angular resolution and in some cases reach the diffraction limit. AO systems and coronagraphs are therefore complementary key resources for direct imaging of exoplanets.

The so-called *quasi-static speckles* constitute currently the main difficulty to direct detection of exoplanets. In contrast to short-lived speckles, quasi-static ones add themselves coherently in the image plane with exposure time. Since they are due to imperfections in the optics, an active way to deal with this noise consists in better non-common path aberrations (hereafter NCPA) calibrations. NCPA calibrations of instrument VLT/NACO was precisely the subject of my internship[4] at ESO (Christiaens, 2012).

Images can be taken following different observing strategies. In the case of companion detections, which are curbed by quasi-static speckles, differential imaging strategies such as reference star (hereafter RDI), spectral (hereafter SDI; Marois et al., 2000) and angular (hereafter ADI; Marois et al., 2006) differential imaging, roll subtraction (G. Schneider & Silverstone, 2003) are the most utilized. Combined to the observing strategy, adequate data reduction technique enables to reduce those quasi-static speckles including, for example ADI, c-ADI, r-ADI and LOCI. The latter stands for Locally Optimized Combination of Images. As its name suggests, it combines reference images so that the speckles substraction is locally optimal. While originally proposed by Lafrenière, Marois, et al. (2007), Pueyo et al. (2012) recently suggested an upgrade, called *damped-LOCI*, which has the further advantage of keeping photometry and spectroscopy unbiased after the locally optimal subtraction of speckles. The implementation part of this master thesis is aimed at improving the *damped-LOCI* algorithm by various ways, optimizing its parameters in an algorithmic way, computing the attenuation factor to putative exoplanets in the field through injection of fake companions, subsequently calculating contrast curves representing the real limit of detection achieved, and finally compiling all the steps of the data reduction, from basic treatments to improved LOCI, in a same, unique and comprehensive IDL code. Finally, this personal version of LOCI is used on two sets of images acquired with VLT/NACO in order to find exoplanets around young stellar targets, known to possess a debris disk.

The first chapter introduces the scientific context in which this master thesis takes place. It describes the science targets which are exoplanets and circumstellar disks, investigates the different ways, both indirect and direct, to detect them, and provides an overview of planetary formation, stressing the point of exoplanets in debris disks.

The second chapter details the four key aspects of HC and HAR direct imaging observations, which are adaptive optics (hereafter AO) systems, stellar coronagraphy, observing strategy and data reduction. For AO systems, the different topics developed are characterisation of atmospheric turbulences, guide stars, wavefront sensors (hereafter WFS), wavefront reconstruction, deformable mirrors and performances of AO systems. Eventually the importance of speckles, and more exactly quasi-static speckles, is highlighted. Main types of stellar coronagraphs are then presented, insisting on the distinction between amplitude masks and phase masks. Observing strategies are subsequently addressed in section 2.3, the concepts of parallactic angle, field-tracking and pupil-tracking are first explained and main differential imaging techniques (RDI, SDI, CDI, ADI and roll subtraction) are then reviewed. The different steps of data reduction are developed in section 2.4. Basic treatment

[4]Course of *Stage en industrie* (SPAT0016-2).

phases are briefly reminded and ADI-based reduction algorithms are discussed, focusing on LOCI and its recent upgrade *damped-LOCI*.

Personal implementation of the whole data reduction and post-reduction process is exposed in chapter 3. Improvements provided to classical-LOCI algorithm including the introduction of fake companions, the plot of contrast curves, the attempt of algorithmic optimization of LOCI parameters and other minor improvements are developed.

Finally, the last chapter is devoted to the application of the implemented code to two sets of images acquired with VLT/NACO instrument. The choice of both observation technique and science targets is first addressed. Determination of the parameters needed for LOCI is then briefly explained. Finally results are provided for the two sets of data, along with first interpretations and possible ways of further investigation.

Chapter 1

Exoplanets and circumstellar disks

Young stellar systems constitute the main science niche of high-contrast and HAR imaging. Their study provides crucial information that are used to constrain formation models. Since the detection of exoplanets and circumstellar disks is also the ultimate goal pursued in this master thesis, with the application of an optimized data reduction code, they are worth to be devoted a full-fledged chapter.

Definitions are first given along with a brief history of respective discoveries in both fields of exoplanets and circumstellar disks. The different indirect detection methods are developed in section 1.3, and eventually confronted to direct imaging. Formation of planetary systems is finally briefly summarized in section 1.4, with focus on the debris disk phase.

1.1 Exoplanets

1.1.1 History

As speculations about the existence of other worlds go back to Greek antiquity, the oldest attempt of planet research reported is attributed to Huygens (1698). Pioneering works of P. Van Der Kamp in the 30's are also noteworthy. However, instrumental lack of sensitivity prevented any detection. Announcements of discovery have been made, but all were sooner or later refuted until 20 years ago.

At scientists surprise, the two first exoplanets (PSR B1257+12 A and B[1]) ever to be detected (Wolszczan & Frail, 1992) and later confirmed (Wolszczan, 1994) were orbiting a pulsar. A few years later though, an exoplanet orbiting an MS star (51 Peg) was eventually discovered, using successfully the radial velocity (hereafter RV) technique (Mayor & Queloz, 1995).

The ten first years of exoplanets discoveries were then characterized by the supremacy of the radial velocity technique. More and more companions were rapidly revealed after 51 Peg b, almost exclusively by RV measurements ($\sim$ 170 exoplanets RV-detected vs. 3 transits as of 2004). After years of continuous improvements in the field of HAR and coronagraphic imaging, first directly imaged planetary companions have eventually been discovered (Chauvin et al., 2005).

[1]Please note that the nomenclature for companions around pulsars is different from exoplanets orbiting MS stars. They are ordered with increasing distance starting from A, instead of starting from b and following chronological order of the discovery.

Up to July 13, 2012, 476 exoplanets out of 777 ($\sim 60\%$) have been discovered through stellar radial velocity measurements (J. Schneider, 2012). Although this method is by far the one that provided the most detections, the proportion tends to balance over the last years thanks essentially to numerous transit detections by *Kepler* (W. Borucki et al., 2004) and *Corot* (Auvergne et al., 2009) ($\sim 30\%$ of all detections). Improving techniques for direct imaging also contribute; 31 exoplanets were discovered in 27 planetary systems (2 multi-planetary systems), which constitute 4% of all detections.

1.1.2 Definition

Extra-solar planets or exoplanets are planets orbiting other stars than our Sun. While this definition seems simple and intuitive to all, a more thorough look is needed to characterize their difference with brown dwarfs. The latter are sub-stellar objects too light for sustaining hydrogen-1 fusion reactions in their cores, but contrarily to mere planets, are heavy enough for fusion of deuterium.

Since the formation scenario of a detected companion is difficult to infer from current observables, a simple pragmatic criterion for their discrimination is needed. Mass happens to be the most suited one (J. Schneider et al., 2011). Up to recently, the commonly admitted mass limit was 13 M_{Jup} (Burrows et al., 2001). However, debate has arisen subsequently to the discovery of a second companion HD168443 c with minimum mass $M.sini = 18.1 M_{Jup}$ to the star HD168443 which has already a $M.sini = 8.2 M_{Jup}$ companion (Marcy et al., 2001).

Figure 1.1 shows that there is no reason to choose 13 M_{Jup}, since no overlap with the brown dwarfs distribution is visible in the mass spectrum of detected exoplanets (Udry, 2010). Moreover, the mass distribution of substellar objects shown in figure 1.2 highlight the lack of stars found with companions ranging from 25 to 40 M_{Jup} (Udry, 2010; Sahlmann et al., 2011). Based on these statistical results, J. Schneider et al. (2011) have suggested an *arbitrary* value of **25** M_{Jup} as the upper-limit of exoplanets minimum mass.

1.2 Circumstellar disks

Circumstellar disks are present around young stars. Among them, *debris disks* (also known as *regenerated disks*) have to be distinguished from *protoplanetary disks* (also known as *primordial disks*.

1.2.1 Protoplanetary disks

Protoplanetary disks are supposed to spawn planetary systems, hence their name. Long suspected by planetary system formation models, they were first confirmed by images in the Orion nebula with the HST (O'dell et al., 1993; McCaughrean & O'dell, 1996).

They are formed at the same time as the *protostar*, with the infall of a large quantity of gas from a molecular cloud. It has been shown that these clouds disperse within $\sim$3 Myr of star formation, removing the source of gas supplying the disks (L. Hartmann et al., 2001). Numerous phenomena are thought to cause their progressive disappearance from the initial protoplanetary disks including viscous accretion radially inward toward the star[2] (with some material subsequently ejected outward

[2]As an order of magnitude, T-Tauri stars of age shorter than 5 Myr have typical accretion rates of $\sim 10^{-7}$-10^{-9} $M_\odot$ yr^{-1} (Gullbring et al., 1998).

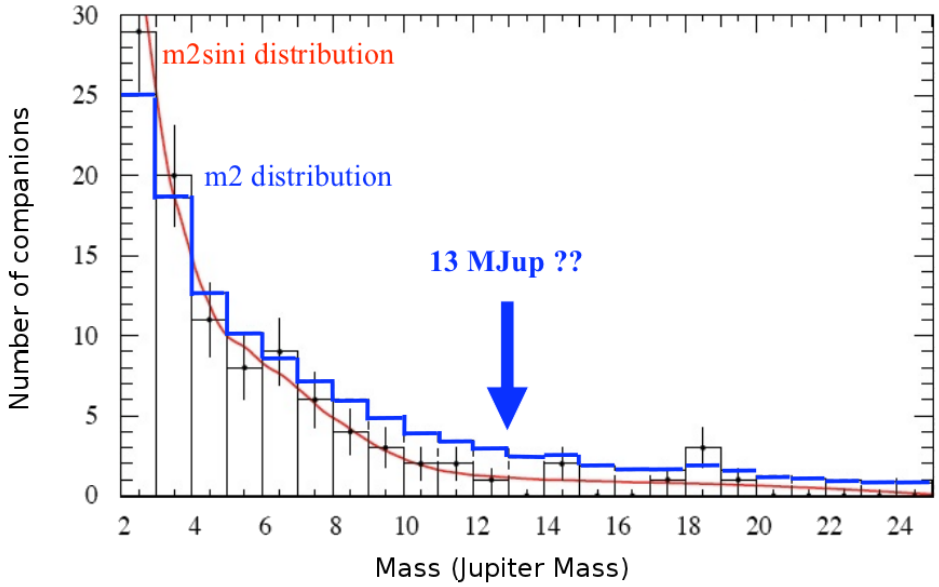

Figure 1.1: Mass spectrum of companions below 25 M_{Jup} (Udry, 2010).

via jets), outward viscous decretion through conservation of angular momentum, accretion into planets (see section 1.4), stellar wind and photoevaporation by the central star or by a neighbouring O-type star (Alexander et al., 2006).

Concerning the average lifetime of protoplanetary disks, Haisch et al. (2001) calculated the fraction of stars possessing protoplanetary disks in young clusters of different ages, establishing that younger clusters had statistically more circumstellar disks and also assessing that the overall disk lifetime was $\gtrsim$ 6 Myr in the surveyed cluster sample. Although (Haisch et al., 2001) has been well-cited for long, Mamajek (2009) has suggested another estimate for the characteristic lifetime of 2.5 Myr based on an exponential fit of the disk fraction vs. sample age plot (also known as *Haish-Lada plot*). Following different stellar parameters such as the stellar mass, multiplicity of the system and proximity to O-type stars, this value seems to span over ∼1.2 Myr for stars heavier than 1.3 $M_{\odot}$ and ∼3 Myr for brown dwarfs (see review by Mamajek, 2009 and references therein). It has also been shown that after 10 Myr, the amount of gas left was about tens of $M_{\oplus}$ and a few $M_{\oplus}$ respectively within a few AU and at 10-40 AU (Pascucci et al., 2006), which has to be compared with the initial mass of of order ∼5.10^{-3} $M_{\odot}$ (Andrews & Williams, 2005).

Protoplanetary disks possess at the beginning huge quantities of gas and are thereby optically thick. This gas consists mainly of hydrogen (∼73% in mass) and helium (∼25%), the main components of nebular clouds. Elements heavier than H_2 and He have higher condensation temperatures, and depending on the distance to the star, do or do not condensate. Large *condensate compounds* are commonly referred as *dust grains*. Those elements heavier than H_2 and He present in protoplanetary disks are oxygen (0.8 %), carbon (0.3%) and nitrogen (0.1 %). Combined with hydrogen, they form most of the *ices* including solid H_20, solid methane (CH_4), ammoniac (NH_3), carbon dioxide and monoxide (CO_2 and CO), and carbon hydrates which are cristalline solids composed of CH_4 or NH_3

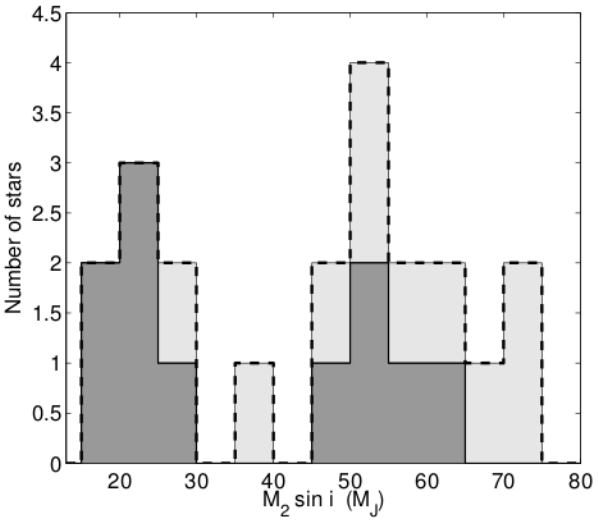

Figure 1.2: Mass distribution of substellar candidates of the CORALIE survey, zoom on the 20-75 M_{Jup} region. The light-grey histogram shows the distribution of all 21 candidates of the CORALIE survey whereas the dark-grey one represents the distribution of the 11 remaining candidates after removal of the 10 stellar companions (Sahlmann et al., 2011).

within water *cages*. All these compounds have a condensation temperature between 10 and 200 K at the common pressure found in protoplanetary disks and are thus called *volatiles*. The so-called *snow line* is defined as the theoretical annulus surrounding a star inside which no *ice* can form. In the case of our Solar system, this line is located just inside Jupiter's orbit, at about 5 AU from the Sun. Material whose condensation temperature is comprised between 200 and 1500 K include on the one hand iron and nickel metallic alloys, and calcium, aluminium, iron, magnesium and sodium silicates on the other. As explained in section 1.4, these compounds are the fundamental bricks of rocky planets formation. Finally, some *refractory* materials can be distinguished including calcium oxyde and aluminium. Their condensation temperature is higher than 1500 K.

In view of its initial composition (mainly gas), dynamics in the disk is dominated by hydrodynamic processes and radiation transfer. The standard model of protoplanetary disks is detailed in (Papaloizou & Terquem, 1999). Figure 1.3 shows some protoplanetary disks that were revealed by HST in Orion nebula (McCaughrean & O'dell, 1996). Images indicate that they are typically a few hundred astronomical units (hereafter AU) in diameter.

1.2.2 Debris disks

Debris disks are usually found around stars of ∼10 Myr to several 100 Myr old, pre-main sequence (PMS) or zero-age main sequence (ZAMS). Principally composed of dust, planetesimals and protoplanetary objects subjected to ongoing mutual collisions (hence their name), they are optically thin by contrast with protoplanetary systems.

They are detected either through the infrared excess that they provide compared to the star unique contribution, or directly thanks to the reflected and scattered light from the star. On average, the

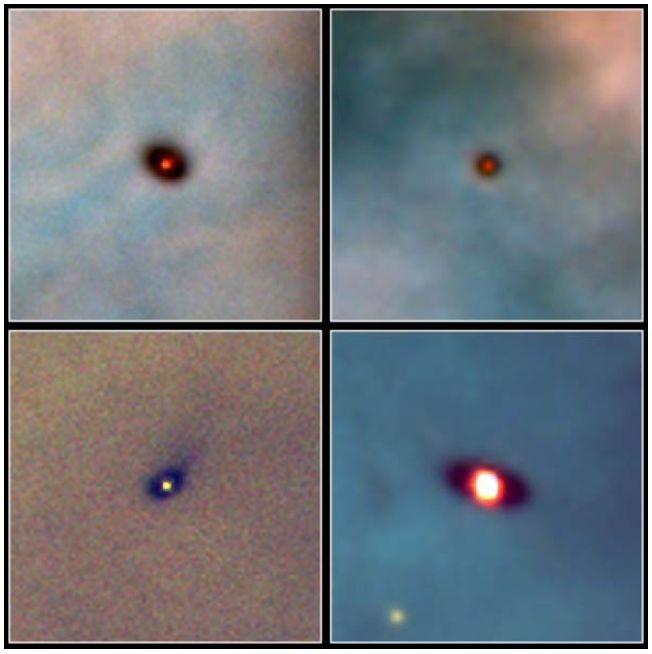

Figure 1.3: Protoplanetary disks observed with HST in Orion nebula. The protoplanetary disks are seen in silhouette against the background luminous gas, with length scales of 100's to 1000's of AU. The bright central spots are the light from the protostars (credit: NASA).

younger the star, the brighter the debris disk (Rieke et al., 2005). The former technique enabled to highlight the first debris disk, around Vega (figure 1.4, Aumann et al., 1984), while the latter allowed Smith and Terrile (1984) to manage the first resolved observation of a debris disk, it was the one around β Pictoris (figure 1.5).

Debris disks have very little amount of gas, which has disappeared through the various mechanisms mentioned in the previous paragraph. In consequence, dynamics of these disks is essentially gravitational, though radiation pressure, *Poynting-Robertson effect*[3] and sometimes wind pressure for late-type stars do also play a substantial role (Beust, 2006). Primordial particles are removed via radiation pressure, Poynting-Robertson drag, and collisional destruction (e.g. Backman & Paresce, 1993; Dominik & Decin, 2003) so that even if they are more evolved than protoplanetary disks, debris disks are not their *direct* remnants. More details about debris disks in the context of planet formation are provided in section 1.4.

1.3 Detection methods

The present section aims at describing briefly the different methods that have been developed for detecting exoplanets. Special attention is paid to the intrinsic physical parameters of the planet that can be deduced from each method. These parameters are: their mass M_p, their radius R_p, their

[3]Poynting-Robertson effect is a process by which dust particles slowly spiral toward the central star due to the non-radial component of radiation pressure (Poynting, 1904).

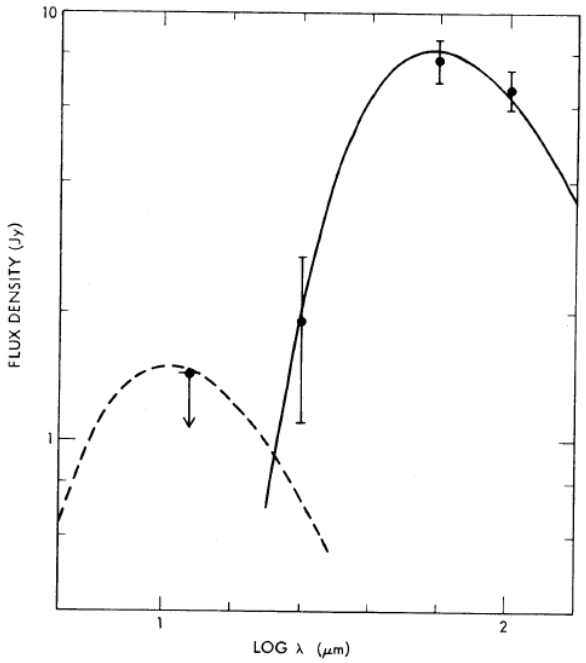

Figure 1.4: Spectral energy distribution of Vega obtained with IRAS. The far IR emission was correctly attributed to thermal dust emission from a disk of debris orbiting the star. It was the first direct evidence that stars can still have circumstellar disks after their - still unconfirmed at that time - protoplanetary disks dissipate. Since then, stars showing a similar IR excess due to a debris disk are qualified as *Vega-like* (Aumann et al., 1984).

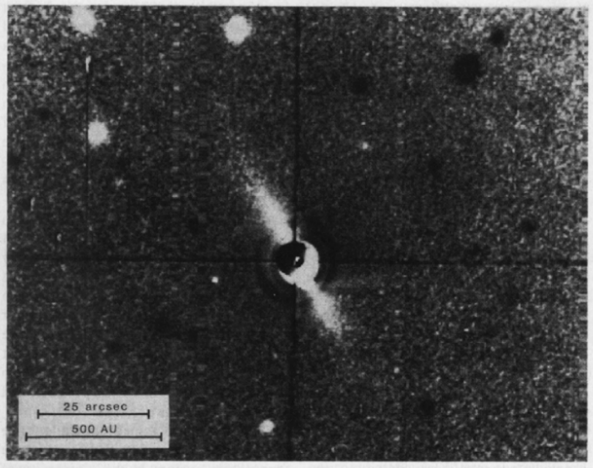

Figure 1.5: Beta Pictoris circumstellar disk imaged with IRAS. During 15 years, β Pic disk remained the only resolved debris disk known, as bright starlight complicates direct detection of the faint light scattered by the disk. (Smith & Terrile, 1984).

orbital period P, the semi-major axis of their orbit a_p, their temperature T_p, their brightness L_p, their distance to the Solar System D and the inclination of their orbit relative to the plane perpendicular to the line-of-sight to the object i_p [4].

The different methods probe different observables leading to these intrinsic parameters. In the case of indirect methods, these observables are parent star's variations in either radial velocity δV_R, astrometric position $\delta\alpha$, time of arrival of signals δt_* or luminosity L_*. The potential success of a given method depends on the instrument's limitation and accuracy concerning the determination of these observables.

1.3.1 Indirect methods

Because of the resolution and contrast difficulties implied in direct imaging, astronomers have generally had to resort with indirect methods for searching exoplanets. Up to 2012, July 13th, 96% of all 777 detections were made through these indirect techniques (J. Schneider, 2012). The latter rely on the fact that the presence of a planet implies to the parent star dynamical perturbations and, if the geometry of the system allows it, fluctuations of the incoming photometric flux.

The dynamical perturbations are due to the fact that stars and their planetary companions are all orbiting their common centre of mass. Therefore, considering the case of a unique companion, the star would follow a small circular orbit with radius $a_* = a_p M_p / M_*$ and period equal to the planet orbital period P. In terms of star's observables, this fact causes perturbations in radial velocity $\delta V_R = 2\pi a_*/P$, angular (or astrometric) angle $\delta\alpha$ and time of arrival of signals $\delta t_* = a_*/c$. These three observables are the ones used respectively in the so-called *radial velocity*, *astrometric* and *pulsar timing* methods.

The study of photometric variations of stars can also reveal the existence of planetary companions. *Transit*, *orbital phases* and *gravitational microlensing* methods are all based on the monitoring of this observable (L_*).

Radial velocity

The radial velocity (hereafter RV) is the velocity of a source projected on the line-of-sight to the observer. The presence of a planet implies reflex motion of the star, resulting in periodical wobbles of its RV. The measurement of these variations relies on the *Doppler effect*, which links the speed of a moving source to the wavelength it emits, applied to the photospheric lines of the host star:

$$\frac{\delta v}{c} = \frac{\delta\lambda}{\lambda} \tag{1.1}$$

Through this formula, the measurement of the absorption lines periodic shift in the spectrum of the parent star directly provides its RV. However, a very high accuracy down to some thousandths of Å (i.e. down to thousandths of spectral line's typical width) is necessary to highlight the presence of a planet. The observation of a large spectral domain at high resolution provides better precision. In particular, this method is very efficient for stars possessing plentiful of both thin and contrasting spectral lines (ie: *cold* dwarfs later than F5-type such as the Sun; Bouchy et al., 2001), though it has proved to detect exoplanets around a wide diversity of stars.

[4] Symbols used throughout this chapter are all summarized at page xii.

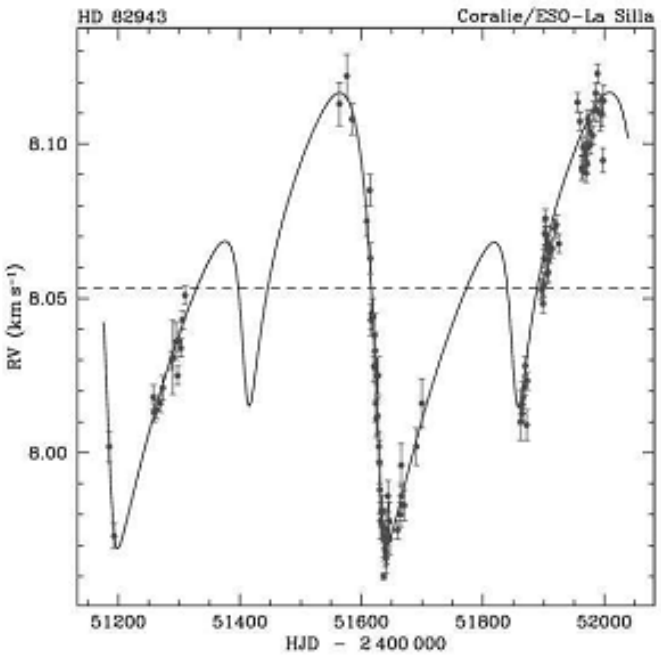

Figure 1.6: Radial velocity curve of the star HD 82943, which possesses two exoplanets in 2:1 resonance (Mayor et al., 2004).

Calculation of the spectrum's Doppler shift can be performed either through least squares fitting of the spectrum with a reference spectrum (real or synthetic), or through its cross-correlation with a binary numerical mask. In the latter case, the mask is designed thanks to libraries of synthetic or real spectra obtained at high spectral resolution, and its non-zero value zones correspond to position and width of theoretical absorption lines at null speed. The cross-correlation fonction is expressed in the velocity space and the position of its minimum provides the intended RV. This method has been described in detail by Baranne et al. (1996) and improved by Pepe et al. (2002).

Once the RV is derived, one has to subtract both the spectrograph drift and Earth movement components from it:

$$V_R = V_{spectrum} - V_{drift} - V_{\oplus} \tag{1.2}$$

The instrument drift is usually measured with a stable spectral source in the laboratory, whereas the speed component $V_{\oplus}$ due to the Earth speed should be derived from the ephemeris of the main bodies of the Solar system. The real RV V_{Rad} can then be expressed as follow:

$$V_{Rad} = V_0 + K.[\cos(\nu(t) + \omega) + e\cos\omega] \tag{1.3}$$

The RV curve (e.g. figure 1.6) thus directly provides the period P of the system, the velocity V_0 of the center of mass and the RV amplitude K of the star. Developing the expression of the two first Kepler laws enables to write the relation between RV amplitude and the different physical parameters

of the system[5]. The third Kepler law is then used to link the period P with the semi-major axis a_P of the orbit.

$$K = \frac{m \sin i_p}{(M_* + m_p)^{2/3} . \frac{(2\pi G)^{1/3}}{P^{1/3}\sqrt{1-e^2}}} = \frac{m_p \sin i_p}{(M_* + m_p)^{1/2}} . \frac{G^{1/2}}{a^{1/2}\sqrt{1-e^2}} \tag{1.4}$$

Assuming a circular orbit and neglecting the mass of the planet with respect to the parent star, equation (1.4) can be simplified:

$$K = \frac{m_p \sin i_p}{M_*^{2/3} . P^{1/3}} \tag{1.5}$$

Equations (1.4) and (1.5) show that provided the amplitude of the RV variation, one can derive the $m_p \sin i_p$ value. Only a lower mass limit can be deduced as far as the inclination of the orbit remains undetermined. Several ways exist to solve this uncertainty, in some cases a constrain upon the self-rotation of the star (thanks for example to its activity) and on its radius (through its spectral analysis) can be established. It is then possible to assess the self-rotation velocity v_{rot} and, knowing $v_{rot} \sin i_{rot}$, estimate i_p which can be supposed close to i_{rot}. Another approach consists in calculating the statistical distribution of masses from the distribution of $m_p \sin i_p$[6] (Jorissen et al., 2001). There is one case where the uncertainty on the inclination can be unambigously removed: when the exoplanets *transit* in front of their star (then $i_p \sim 90°$).

Further on, the entire fit of the RV curve (equation 1.3) leads to 5 (out of 6) parameters of a Keplerian orbit: P, a_P, T_P (the epoch of the passage at the periastron), e and ω. In addition, other by-products are obtained when analyzing the spectrum of the star: the projected self-rotation velocity $v_{rot} \sin i_{rot}$, the effective temperature T_{eff}, log g, the metallicity [Fe/H], as well as the activity index. In summary, an extensive load of parameters on both the planet and its parent star are obtained with the radial velocity method. These analyzes can then be used to establish statistic relations and correlations between exoplanets and parent stars properties (see e.g. Santos et al., 2003, 2004).

The case of multiple planets systems can be dealt with two different approaches, either sequentially or simultaneously[7]. With the first approach, the signals of the most influencing companions are sequentially deleted until no more detectable signal is found. A better approach, if possible, is to fit the RV curve directly with the right number of companions. Nevertheless, some exoplanetary systems possess orbits that are in resonance and cannot be considered independent (e.g. figure 1.6). The two bodies Kepler laws are then unsufficient, and one needs to take gravitational interactions between the different bodies into account.

Finally, as equation (1.4) indicates, the RV method is biased because it tends to favour the detection of planets that are both massive and close to their parent star, hence exerting a greater dynamical influence. The method allowed astronomers to unveil the existence of an unexpectedly large number of hot Jupiters, e.g. 51 Peg b (Mayor & Queloz, 1995) or HD 209458 b (aka *Osiris*, Charbonneau et al., 2000).

[5]We do not give the details of the developments, however the interested reader will find an exhaustive demonstration in the course of *Etoiles variables* (G. Rauw, 2010-2011).

[6]Using the fact that an isotropic distribution of the orbits orientation produces a statistical distribution of the inclinations $\sin i_p$.

[7]This is detailed in the course of *Analyse de séries temporelles* (Gosset, 2011-2012).

Pulsar timing

Exoplanets orbiting a pulsar were the first to be ever detected (Wolszczan & Frail, 1992) and confirmed (Wolszczan, 1994). Their method was based on the measurement of faint anomalies in the regular radio emission of the observed pulsar, albeit the search for exoplanets was not the primary purpose. In view of this primary detection, scientists were optimistic about the amount of companions that would orbit pulsars. On the contrary, twenty years after this finding, only 15 other pulsar systems were found to possess a companion (J. Schneider, 2012).

Pulsars being the extremely dense remnants of supernovas, they are considered of lesser scientific interest because life as we know it could probably not have survived neither the cataclysm, nor in the present environment still exposed to high-energy radiation. However, to date, pulsar timing is the most sensitive technique towards the detection of light planets, able to unveil those down to less than a tenth of $M_\oplus$. Such sensitivity makes it even capable of detecting mutual gravitational perturbations between the various members of a planetary system, enabling an extensive characterization of both planets and their orbital parameters.

Transit

When a planet passes in front of its star (ie: *transits*), it produces a shallow dip in the starlight flux arriving to the observer. The detection of a transit in the stellar lightcurve requires a correct orientation of the planet's orbital plane so that the observer-exoplanet-star alignment can occur. For random orientations, the geometric probability p only depends on the star radius and the semi-major axis of the planet's orbit: $p = R_*/a_p$. For a *Jupiter* (resp. an *Earth*) around a *Sun*, this probability is about 0.1 % (resp. 0.5 %). The transit method thus favors the detection of planets close to their star. Not only the p probability is larger for shorter a_p, but also the required time base for photometrical monitoring, which needs to span at least over an entire orbital revolution, is shorter.

Figure 1.7 represents the effect of the different phases of a planetary transit on its stellar lightcurve. Three main parameters in this stellar lightcurve are used to characterize the planetary system's physical parameters: its *depth*, its *duration* and its *shape*.

The *depth* of a transit provides directly the radius ratio between the exoplanet and the host star. Writing F_{off} (resp. F_{on}) the measured stellar flux out of (resp. during) transit, and assuming a uniform brightness of the disk[8], we have:

$$\Delta F = \frac{F_{off} - F_{on}}{F_{off}} = \left(\frac{R_p}{R_*}\right)^2 \tag{1.6}$$

This drop is about 1% (resp. 0.01%) for a 1 R_{Jup} (resp. 1 $R_\oplus$) planet.

The transit *duration*, assuming a circular orbit can be expressed in terms of orbital parameters and stellar radius (Seager & Mallén-Ornelas, 2003):

$$D_T = \frac{PR_*}{\pi a_p}\sqrt{\left(1 + \frac{R_p}{R_*}\right)^2 - \left(\frac{a_p}{R_*}\cos i_p\right)^2} \tag{1.7}$$

[8]Ie: neglecting the fact that stars appear slightly brighter in the center of their disk then on the edges (also called *limb darkening effect*).

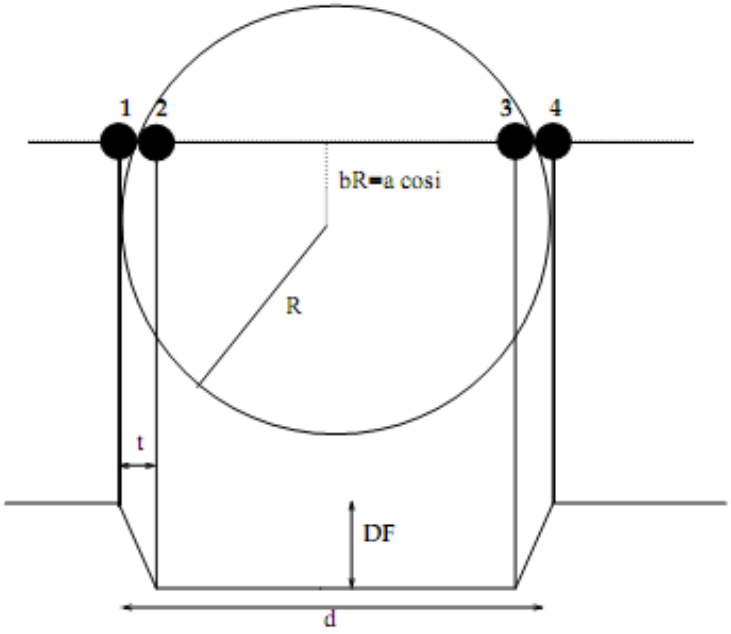

Figure 1.7: Sketch of a planetary transit. The phase between contact 1 (resp. 3) and 2 (resp. 4) are called *ingress* (resp. *egress*). The latitude of the transit on the stellar disk defines the U- (long flat bottom part, latitude close to stellar equator) or V-shape (short flat bottom part, latitude close to the stellar poles) of the lightcurve. Taking the *limb darkening* effect into account would imply a more rounded shape to the lightcurve.

with $b{=}a_p/R_* \cos i_p$ being the so-called *impact parameter*, i.e. the projected distance of the planet's center to the star's equator. We have assumed a circular orbit, which is not an irrelevant assumption since the transit method tends to detect exoplanets close to their star, and whose orbit is thus more likely to have been circularized by tidal effects. However, even close orbits do sometimes show an eccentricity greater than 0.1 (e.g. Mercury in our Solar System). Moreover, missions such as *Kepler* are now able to detect long-period exoplanets, thanks to longer time bases. In the case of non-zero eccentricities, the transit duration depends additionally on the star-planet distance at the time of the transit, on the phase angle, and (obviously) on the eccentricity (Tingley & Sackett, 2005). It is noticeworthy that the eccentricity can be accurately determined with the observation of the secondary eclipse when it is discernible (see e.g. Charbonneau et al., 2000; Allen, 2005).

The *shape* of the lightcurve, more exactly the ratio of the durations of the *flat bottom* part (D_f) over the total transit (D_T) can also be used to constrain physical parameters:

$$\left(\frac{D_f}{D_T}\right) = \frac{\left(1-\frac{R_p}{R_*}\right)^2 - \left(\frac{a_p}{R_*}\cos i_p\right)^2}{\left(1+\frac{R_p}{R_*}\right)^2 - \left(\frac{a_p}{R_*}\cos i_p\right)^2} \tag{1.8}$$

In summary, equations ((1.6), (1.7) and (1.8)) enable to constrain the value of b, R_p, R_* and M_*, though the two latter can be determined with other methods such as high-resolution spectroscopy, or with stellar evolution models. Some additional parameters such as the effective temperature of the planet, its atmospheric composition, and escape rate of its extended atmosphere, its albedo or the presence of rings or satellites can be assessed through the study of secondary effects (secondary eclipses, thermal emission) in some specific favorable cases, typically short period planets around bright stars.

Combination of transit and RV methods is well-suited, particularly in order to provide mutual complementary observations for the rejection of impostors, including grazing binaries (e.g. Drake, 2003), small-radius stellar companions (e.g. Pont et al., 2005, 2006), eclipsing binaries in triple systems (e.g. Torres et al., 2004; Mandushev et al., 2005) and false positives due to stellar activity or instrumental features.

However, the probability of observing a transit around a star is very low (about 0.1% for a short period planet). Photometric precision in ground-based observations is further limited by atmospheric extinction, seeing variations, photon noise and stellar activity noise. Only the two latter do also apply for space-borne observations, which have the additional advantage of long and continuous acquisition series. These facts explain the sending of spatial observatories CoRoT and Kepler. Up to July 13, 2012, a total of 239 exoplanets distributed in 205 planetary systems have been discovered by transit (J. Schneider, 2012).

Orbital phases

Similarly to Venus phases in our own Solar system, planets in close orbits around their star undergo reflected light variations changes. Although the planet is not resolved, it is the small periodical variations in the incoming combined light from the host star and the planet that enable to highlight this phenomenon. The photometric precision required for a Jupiter-sized exoplanet close to its star is

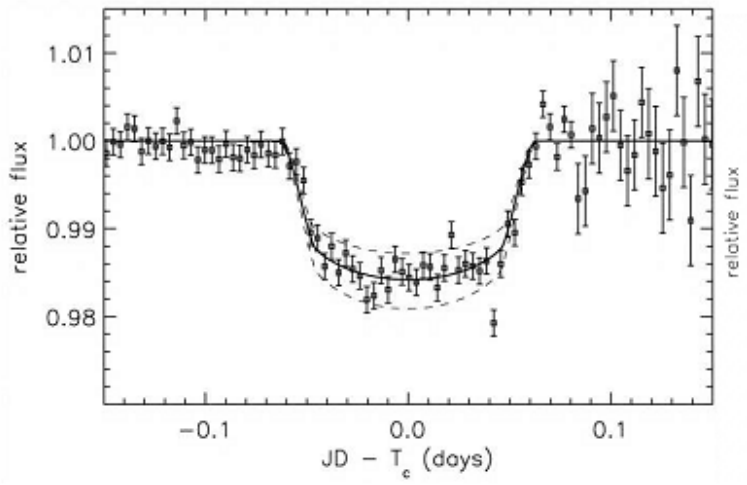

Figure 1.8: Lightcurve of the first successful exoplanetary transit: HD 209458 b (Charbonneau et al., 2000).

about the same as to detect an Earth-sized planet in transit across a solar-type star, which is nowadays possible (e.g. Batalha et al., 2011; Fressin et al., 2012).

This effect has first been measured around detected exoplanets known to transit in front of their star, both by Corot (Snellen et al., 2009) and by Kepler (W. J. Borucki et al., 2009). Since then, several planets have been discovered by Kepler thanks to this method. In the long run, orbital phases measurements are expected to find the most planets because the reflected light variation with orbital phase is largely independent of orbital inclination of the planet's orbit and does not require the planet to pass in front of the disk of the star.

Gravitational microlensing

In general relativity, the presence of matter distorts spacetime and thereby deflects any lightbeam passing in its proximity. The principle of gravitational lensing relies on the alignment of a background *source*, a foreground *lens* and the *observer* so that the light from the source is focused and hence amplified at the location of the latter.

This phenomenon is not only used in the field of exoplanets so that different regimes are usually distinguished, among which *microlensing* is characterized by unresolved multiple images. In the case of microlensing applied to the search for exoplanets[9], a distant star in our Galaxy (typically about 8 kpc away) acts as the source, while the star with its planetary companion play together the role of the foreground lens, typically located at half way. The order of mass for the lens star is 1 $M_{\odot}$, whereas the two images of the background source are only separated of about 1 mas (ie: unresolved by the typical instruments searching for gravitational occurences).

The method consists first in monitoring a large number of faint potential sources, both frequently and simultaneously, because the probability of the observer-host star-background source exact align-

[9]Indeed, it can also be used for the detection of quasars.

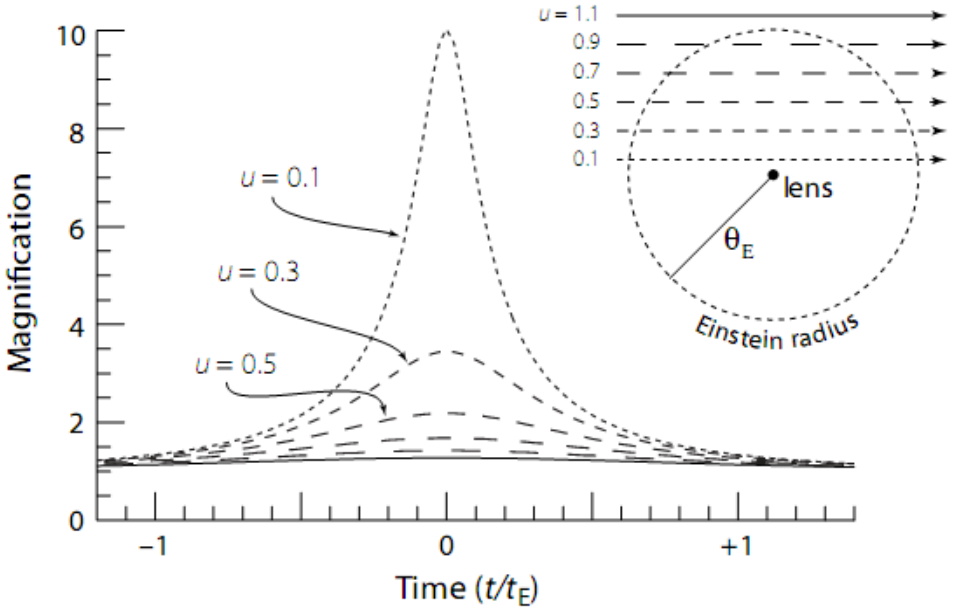

Figure 1.9: Theoretical microlensing lightcurve giving the theoretical evolution of magnification with time, for different values of $u = \theta_S/\theta_E$ where θ_S is the angular distance between the lens and the source, and θ_E corresponds to the angular Einstein radius which is about $\sim$1 mas for the lens stars observed. Magnification is more pronounced for decreasing u (Paczynski, 1996).

ment (within the *angular Einstein radius* [10], which is around 1 mas) is very low. The Galactic bulge is therefore the ideal target region. If there is a slight rising in a particular lightcurve, it can be the sign for a favorable alignment development. Theoretical microlensing lightcurves for a point source passing at different projected angular separations u from a single lens star (ie: without planetary companion) is given in figure 1.9.

The total duration T_G for the whole variation, in the middle of which the maximum magnification A_G is reached, is about several weeks, depending on the transverse velocity V_G (Mao & Paczynski, 1991). Several weeks are usually sufficient to discern the presence of a planetary companion from the additional magnification it would provide to one of these theoretical curves. A geometrical and relativistic approach of gravitational microlensing applied to exoplanets detection is out of the topic of this thesis. The interested reader may refer to (Wambsganss, 2006) for wider developments about microlensing.

Nonetheless, the lightcurve being the observational signature of both the geometry and mass

[10]The *angular Einstein radius* is the characteristic angle of the situation and is defined as:

$$\theta_E = \left(2R_S \frac{D_{LS}}{D_L D_S}\right)^{1/2} = \left(\frac{4GM_L}{c^2}\frac{D_{LS}}{D_L D_S}\right)^{1/2}$$

Similarly, the Einstein physical radius is given by $R_E = \sqrt{4GM_* d}$, when the system lies at mid-distance d from the source.

distribution of the planetary system, physical parameters that are the exoplanet's mass M_p[11], the separation d to its star and system's distance to the Earth D_L can be induced from it, in particular from A_G and T_G. The accuracy of these estimates depends essentially on the exactitude of the alignment, since angular proximity provides a greater magnification. This magnification can be as high as ∼3000 (Dong et al., 2006), and may be even better for an even more aligned configuration.

Compared to other methods, gravitational microlensing probes exoplanets orbiting stars located at 1-8 kpc, thus far beyond the Solar neighbourhood probed by other methods. For a typical host star located 4 kpc away and with a mass $\sim 1\ M_\odot$, the physical Einstein radius is about 4 AU. This value is precisely the lengthscale for the orbit of exoplanets probed. In view of the magnifying factor, the method has the advantage of being also sensitive to low-mass exoplanets at further distance from their star, exploring thus a much wider region in the mass-semi-major axis diagram hardly accessible by other techniques: masses down to below 10 $M_\oplus$ at 0.5-10 AU. However, in view of their extremely weak probability, gravitational microlensing events present the drawback of occuring only once, preventing any additional study of the system. Up to August 4, 2012, 16 exoplanets have been discovered thanks to this technique (J. Schneider, 2012).

Other possible indirect methods

The following techniques have also been proposed in order to find exoplanets. Though theoretically possible, they have not led to successful detection yet.

Astrometry Similarly to the RV method, detections by astrometry (or *narrow-angle* astrometry in the specific case of exoplanet research relies on the gravitational perturbation of the planet on the star's position. The principle is simple and was the first technique to be proposed, as suggest statements made by W. Herschel in the late 18th century. Paradoxically, it has not led to successful discovery yet, although numerous announcements from the 19th century up to the recent VB 10b candidate (Pravdo & Shaklan, 2009) whose existence was finally ruled out by RV measurements (Bean et al., 2009). However, astrometry has already been used in order to confirm and further characterize known planetary systems (e.g. Gl876 with HST (Benedict et al., 2002)). In particular, when a planetary candidate is found by direct imaging, it must be re-imaged later to be confirmed. An astrometric measurement of the star is thus necessary to establish if there is indeed a commmon motion.

Future *GAIA* mission, cornerstone project of ESA, is expected to be capable of astrometric detection of thousands of M_{Jup} exoplanets up to 200 pc away thanks to its high accuracy (1 to a few μas)[12]. A potential advantage of this technique is that it is most sensitive to (massive) planets with large orbits. It is thus complementary to the biased RV and transit methods. As a consequence, the drawback is that very long observation times, years or decades, will be needed.

Eclipsing binary minima timing Similarly to the first pulsar detections, this technique proposed by Deeg et al. (2000) is based on timing of an event known to be highly periodic at relatively short timescale: eclipsing binaries. The presence of a companion, either a third unseen stellar companion or

[11] As a matter of fact, it is the mass ratio q that is determined. an estimate of the mass of the star is needed to obtain the exoplanet's mass.

[12] More details about GAIA on http://smsc.cnes.fr/GAIA/index.htm

a planet, will imply a slight periodic offset of the binary's centre of mass. As the stars in the binary are displaced by the planet back and forth, the eclipse minima will vary in time (e.g on time, too late, on time, too early and so on). At present state, this method seems the most appropriate to probe the presence of planets around close binary systems.

Auroral radio emissions The recent study of Nichols (2011) has led to the conclusion that auroral radio emissions from giant planets with plasma sources could be detected in the future by upcoming radio-telescopes. A typical example of auroral radio emissions in our Solar system occurs in Jupiter's strong magnetic field due to its volcanic moon Io.

1.3.2 Direct imaging

Direct imaging of exoplanets presents attractive advantages. *Seeing* literally planets in other systems allows orbital parameters to be determined. Indeed, providing the distance of the star, the semi-major axis a_p can be infered from the angular separation β through the direct formula $\beta = a_p/d$. As the planet moves forward onto its orbit, observations separated in time do also reveal the orbit's inclination i_p (e.g. for β Pic, Lagrange et al., 2010). Spectroscopy of the light from the companion can further be used to characterize its albedo, temperature and chemical composition. Direct imaging is furthermore complementary to both RV and transit methods since, by contrast, it probes preferentially giant planets with long periods, at great angular distance from their star. It is also appropriate for studying exoplanets around young stars, around which exoplanets have not cooled down yet and are hence intrinsically brighter. However, to deserve all these advantages, one has to overcome two considerable obstacles, which are discussed in the next paragraph.

Difficulties of direct imaging

Tiny angular separation $\beta = a_P/D$ and luminosity contrast L_p/L_* are the two main hurdles that have to be overcome while endeavouring the direct imaging of exoplanets.

Angular separation has to be confronted against the angular resolution θ of the telescope. For a mono-pupil telescope of diameter D, it is theoretically given for a planar wavefront by the angular radius of the central peak in the diffraction pattern:

$$\theta \simeq \sin\theta = 1.22\frac{\lambda}{D} \tag{1.9}$$

where λ is the wavelength of the observation. If the angular separation is smaller than θ, the planet cannot be resolved. For example, in order to observe a planet at 1 AU from its star located 10 pc away, at the wavelength of 10 μm, relation (1.9) says that a 25m telescope is theoretically needed. However, atmospheric turbulences affect the incoming wavefront, so that the angular resolution is in practice limited by the *seeing* (see next chapter). In order to push the angular resolution at its best, one has typically to use *adaptive optics*, described in the next chapter. Table 1.1 provides typical angular resolutions and corresponding techniques used to deal with it. Ground-based mono-pupil telescopes fitted with AO systems are typically limited to an angular resolution of 50 mas. Multi-telescopes interferometry are complementary as they can be used to reach close regions to the star (a $\geq$ 1 AU) or for distant stars.

	0.1 AU	1 AU	5 AU	30 AU	
3 pc	30 mas	0.3"	1.5"	9"	*Ground-based AO*
10 pc	10 mas	0.1"	0.5"	3"	*or*
25 pc	4 mas	40 mas	0.2"	1.2"	*spatial telescope*
100 pc	1 mas	10 mas	50 mas	0.3"	
	Interferometry				

Table 1.1: Required angular resolutions in order to resolve the exoplanet for various combinations of planet distance to its star (0.1 AU: *hot Jupiter*, 1 AU: Earth, 5AU: Jupiter, 30AU: Neptune) and system's distance to the Sun (3-25 pc: close stars, star formation regions are typically at ∼100 pc).

The second difficulty comes from the luminosity contrast involved between the planet and its star. Planets incoming light L_p divides into two distinct contributions: their illumination by the parent star $L_{p,ref}$ and their intrinsic emission $L_{p,int}$. The brightness acquired by reflection of the central star light is given by

$$L_{p,ref} = \frac{AL_*}{8}\left(\frac{R_p}{a_p}\right)^2 \phi(t) \tag{1.10}$$

where $\phi(t)$ is an orbital phase factor given by $\phi(t) = 1 - \sin i_p \sin(2\pi t/P)$. This reflected luminosity increases with the square of the radius R_p of the planet, but decreases with the square of the semi-major axis a_p of its orbit, so that this luminosity is dominant for short separations (typically up to 1.5 AU for a G5 star). In the case of a Solar-type star ($T_{eff} \simeq 5800$ K), the maximum of $\lambda N(\lambda)$ is around 0.6 μm[13] (figure 1.10). The intensity of the planet's intrinsic emission depends on its effective temperature (hence on the distance to its star) and on the square of its radius. For example, the Earth ($T_{eff} \simeq 300$ K) has its maximum $\lambda N(\lambda)$ around 12 μm (figure 1.10). Therefore, the contrast between a Solar-type star and an Earth-size planet at 1 AU is of order 5 10^{-9} in the visible domain (0.4-0.7 μm), and about 7 10^{-6} in thermal infrared (8-15 μm). For a Jupiter-size planet orbiting at 5 AU from its star, the contrast in visible is also about 10^{-9}, whereas it drops to about 10^{-5} for a *hot Jupiter* at 0.05 AU. In thermal infrared, although Jupiter is farther to the Sun, it has a surface 100 times greater than the Earth, so that it is still brighter at 12 μm.

The faint partner lies in the photon noise $\sigma = \sqrt{N_{ph}}$ of the rings of the diffraction pattern. The brightness L_p has thus to be compared with the typical brightness of the diffraction ring at angular distance β from the parent star:

$$L_{ring} = L_*(\beta/\theta)^{-3} \tag{1.11}$$

In the case of a Jupiter-Sun system seen at 10 pc, it is possible to infer from equations (1.9), (1.10) and (1.11) that the planet to star's wings brightness ratio is around 5 10^{-6} for an 8m telescope at a wavelength of 3.8 μm (which is the wavelength used in our observations). A way to deal with

[13] As a reminder, the relation between the temperature of a black body T_{eff} and the wavelength of its maximum photon emission λ_{max} is given by Wien's displacement law:

$$\lambda_{max} = \frac{3.6698\ 10^{-3}}{T_{eff}}$$

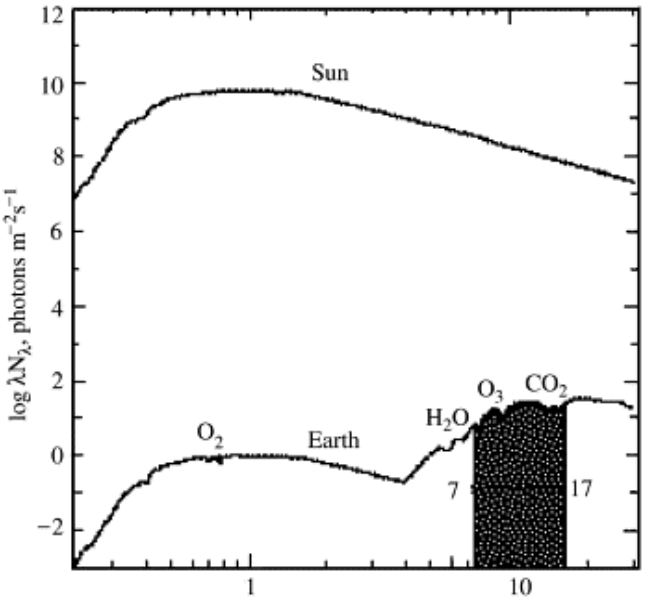

Figure 1.10: Spectral energy distribution of the Sun and the Earth as seen from 10 pc. The contrast ratio is more favorable in thermal infrared (Beichman et al., 1999).

this contrast issue is stellar coronagraphy which is detailed in section 2.2. However, it should be stressed that in practice, the main limitation comes from speckles (see section 2.1.7), rather than from diffraction wings.

Since the contrast ratio lowers at longer wavelengths, it seems *a priori* logical to observe at the planet's thermal emission wavelength. However, an additional difficulty for ground-based telescopes consists in the fact that as the contrast ratio lowers, both the atmospherical absorption and the atmospheric background (due to this same thermal emission!) globallly increases with wavelength. Figure 1.11 shows the different bands in wavelength not affected by absorbing molecules (essentially water vapor and carbon dioxyde) in our atmosphere. Ground-based direct research has thus to span an intermediate range of wavelength bands (J, H, K, Ks, L, L' and M). The specific observations used in this work were taken in the L-prime band, which is the transmission window centered on 3.7-3.8 μm, $\delta\lambda = 0.5\mu$m. In NIR wavelengths, the most appropriate targets are giant exoplanets in young planetary systems. Models for giant planets of about 100 Myr predict a contrast ratio of of order 10^7 in J, H and K bands (Chabrier et al., 2000; Baraffe et al., 2002). According to these models, older objects would be an order of magnitude fainter.

On the contrary, IR space-borne telescopes seem *a priori* indicated for exoplanet research, since the absence of atmosphere would allow spectra of the exoplanets to be taken. In particular, the composition of their atmosphere (CO_2, NH_3, CH_4) and perhaps *bio-signatures* (CO_2, H_2O, O_2/O_3 in specific temperature and pressure conditions, Selsis et al., 2003) could be highlighted. However, it is again the two first limitations, angular resolution and contrast, that curb direct detections from space.

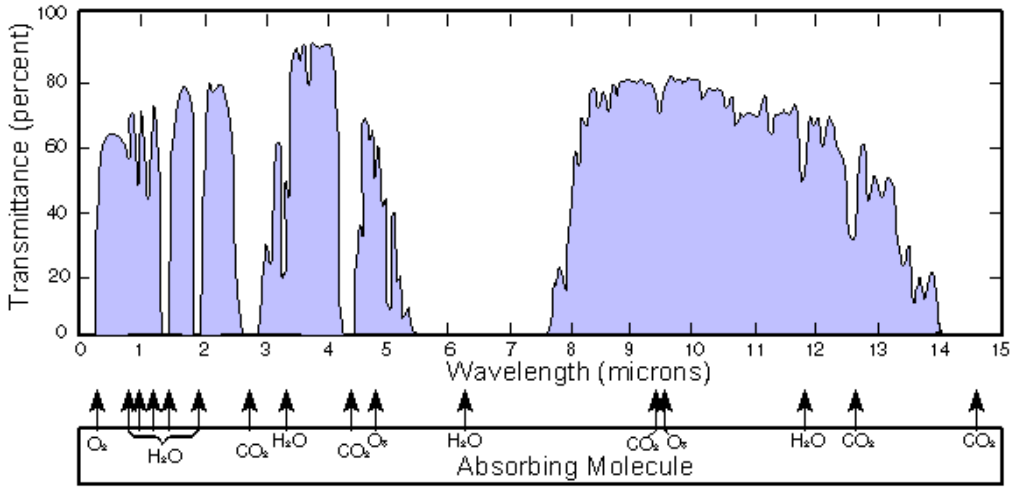

Figure 1.11: Transmittance of the atmosphere as a function of wavelength and the corresponding absorbing molecules. J-band is centered on 1.25μm with bandwith (FWHM) $\delta\lambda = 0.38\mu$m, H-band is centered on 1.65μm with $\delta\lambda = 0.48\mu$m, K-band is centered on 2.2μm, $\delta\lambda = 0.7\mu$m, L-band is centered on 3.5μm with a $\delta\lambda = 1.2\mu$m, L' band is centered on 3.8μm with a $\delta\lambda = 0.6\mu$m and M-band is centered on 4.8 μm with a $\delta\lambda = 5.7\mu$m (Sterken & Manfroid, 1992).

Multi-telescope interferometry

An alternative solution to reach sufficient angular resolution resides in using multi-aperture interferometers instead of large mono-pupil telescopes. In that case, the D parameter of equation (1.9) has to be replaced with $2B$, B being the baseline of the array. As baselines up to several hundred meters can be used, they provide the best angular resolutions, down to ~ 1 mas in the NIR, hence enabling to investigate the innermost parts of circumstellar discs in nearby star forming regions. Two types of interferometry are distinguished in the field of exoplanet direct imaging: *phase-closure interferometry* and *nulling interferometry*.

Interferometry measures the interferences between telescopes acting as *Young holes*. A slightly shifted planet relative to the star adds a contribution to the interferogram of the unique star. The *closure phase* method (Monnier, 2003) is typically used to highlight this effect (see e.g. Absil et al., 2011). If in addition a chromatic dependency is detected, then it is more than likely that a planet is indeed present, as it is brighter at longer wavelengths. However, as this technique allows high angular resolutions to be reached, the main drawback is that contrasts typically greater than 10^{-4} are needed to detect the amplitude of the planet's contribution to the interferogram. Again, regarding the contrast issue, optimal ground-based interferometric observations are to be carried out in NIR and mid-IR wavelengths. An example of differential interferometer recently implemented is the instrument PIONIER on the VLTI, which has provided among the best dynamical ranges (1:500) yet (Absil et al., 2011).

Projects of IR-interferometers in space have been proposed, such as ESA's *Darwin*, NASA's *TPF*, or later *Darwin-TPF* in partnership. The latter would have been based on the principle of *nulling*

interferometry, an idea first proposed by Bracewell and MacPhie (1979). Considering for simplicity the case of two telescopes, separated by a distance l, the light coming from them can be made interfered destructively in the focal plane. This can be done by adding to one of the wavefront phase a quantity π. At the interference point, the total wave amplitude for the star is $A_* + A_* \exp(i\pi) = 0$. For the planet, which has a slight angular shift β relative to the star, the amplitude is

$$(A_p)_{total} = A_p + A_p \exp(i(\pi + \beta(l/\lambda))$$

The separation between telescopes can then be arranged so that $\pi + \beta(l/\lambda) = 2n\pi$, and thereby maximizes the total amplitude of the planet: $(A_p)_{total} = 2A_p$. The central star light is thus suppressed whereas the planet's flux is theoretically doubled. Nulling-interferometry solves thus at the same time the contrast and angular resolution problems. Numerical simulations carried out by Mennesson and Mariotti (1997) have led to very optimistic results, as both the map of the inner Solar system placed at 10 pc showing Venus, the Earth and Mars, and their spectra testify. Current limitation in the practical implementation of a Darwin-type project resides in accuracies involved for nulling-interferometry (nm precision), flight in formation technologies are currently not able to meet this high accuracy.

Examples

High dynamic range and high angular resolution limitations caused the first exoplanet to be directly imaged only in 2005 (Chauvin et al., figure 1.12). Conditions were particularly optimal for this first detection, as 2M1207b is both young (∼8 Myr old) and massive ($\sim 5M_{Jup}$), and its parent star, being a brown dwarf, is intrinsically relatively faint. This first detection was made thanks to observations with the VLT/NaCo instrument.

Eleven exoplanets have then been imaged between this first detection and 2008 (J. Schneider, 2012). However, all of them were orbiting at several hundred (between 100 and 800 AU). Similarly to the surprise generated by the discovery of exoplanets with periods as short as 51 Peg b (Mayor & Queloz, 1995), the first images of extrasolar planets were for objects at astoundingly large separations.

For more *interesting* (ie: planets less massive and closer to their star) discoveries, one has to wait the quasi-simultaneous imaging of a sheperding planet around Fomalhaut (Kalas et al., 2008) and three planets around HR8799 (Marois, Macintosh, et al., 2008), followed a bit later by β Pic b (Lagrange et al., 2009). Since then, a fourth planet has also been unveiled in the HR8799 system (Marois et al., 2010). Figure 1.12 provides the images of their detection. All these examples are further discussed in section 1.4 since these systems are also harboring a debris disk.

Up to August 5, 2012, 31 candidates among 27 planetary systems have been imaged (J. Schneider, 2012).

1.3.3 Lessons to be drawn

In conclusion, different techniques probing different scales enabled to discover an astounding diversity in the newly discovered extra-solar world. Depending on their size and distance to their star, they are classified in *hot/cold Jupiters*, *hot/cold Neptunes*, *super-Earths*, *sub-Earths* and Earth-like planets.

Those different methods are complementary. Combination of radial velocity and transit techniques allows a large number of physical parameters to be determined, triggering thereby the most exhaustive characterizations of known systems. The radial velocity technique is biased towards massive planets

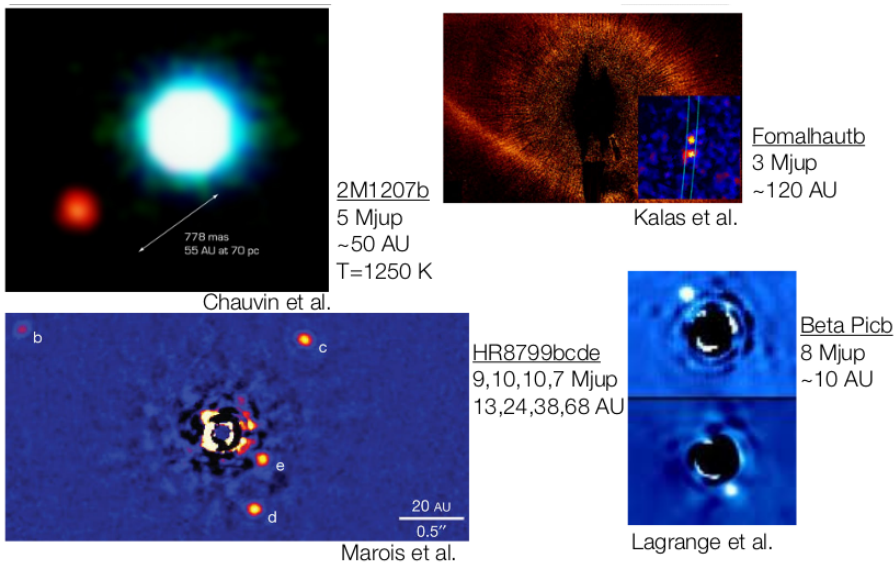

Figure 1.12: Overview of the outstanding imaged systems. Upper left: First direct image of an exoplanet: 2M1207b (Chauvin et al., 2005). Upper right: Fomalhaut's debris disk with the announced Fomalhaut b (Kalas et al., 2008). Lower left: HR8799 b, c, d and e (Marois, Macintosh, et al., 2008; Marois et al., 2010). Lower right: β Pic b in (Lagrange et al., 2009, 2010).

with short orbital periods, and thus a surprising number of Hot Jupiters have been seen. This is also true for transit, which is in addition biased toward the inclination. Gravitational microlensing happens to be less biased, able to provide statistical information about planetary systems, generally at further distance. Gravitational microlensing surveys have recently revealed that it was the rule rather than the exception, for stars in our Galaxy to host at least one planet. *Super-Earths* are the most abundant type, being associated with around 62% of stars; 52% host *cold Neptunes*; and 17% host *Jupiters* (Cassan et al., 2012). However, this technique is limited by the low probability for favorable events and its parallactic distance bias (the ideal population of sources lying in the galactic center).

Direct imaging detects preferentially massive exoplanets on large orbits and exoplanets in young planetary systems, being capable of feeding and constraining formation models. However, with the improving performances of small-angle coronagraphy (see e.g. the vector vortex coronagraph, Mawet et al., 2005, 2010), the large orbit bias will probablly tend to soften in the future. Direct imaging have proved that planetary systems extend not only much closer to, but also much farther from, their host stars than what was expected exclusively from our Solar system. It is thus complementary to RV and transit methods which achieved the most discoveries so far.

In view of the wide range of exoplanets that have been discovered so far, there is no *best* method, though when astronomers using different techniques gather, each would strongly argue in favor of their own technique! All those different methods reveal in fact different fragments of the big puzzle. In order to get a more comprehensive picture, one needs to push from all directions.

1.4 Planetary formation

Since exoplanets in debris disk are the primary targets of our implemented reduction pipeline, a section is devoted to them after a (not so short) summary of current planetary formation theory.

From the middle of the 18th century to the middle of the 20th, two fundamentally different, competing scenarios have been suggested to account for the planetary formation. The nebular hypothesis, initially proposed by Swedenborg (1734) and further developed by Kant in 1755 and Laplace in 1796, argued for the formation of planets from residual (or, in earlier versions, spin-ejected) circumstellar material and suggested that planetary systems may be common. Other theories flourished as supporters of the nebular hypothesis could not explain the fact that 99% of the Solar system's angular momentum resides in planets. The catastrophic *tidal hypothesis* for example, proposed by Jeans and Jeffreys in 1918, by contrast, regarded planets as condensates from material torn out of a star by a close encounter or collision with another star, and implied that the Solar system may be exceptional.

The nebular hypothesis is now unanimously accepted by the scientific community. The gravitational collapse of a dense interstellar cloud of gas gives birth to about hundred stellar clouds. Each of them is spheroidal, relatively large (up to 2 light-years in diameter, hereafter Ly) and slowly rotating. As it condenses, conservation of the angular momentum leads to faster rotation rate and formation of an increasingly flattened disk of gas and dust around the central newborn star, the *protoplanetary disk* discussed in section 1.2. Temperature in these disks spans the range of more than 1000 K close to the star, to a few tens of Kelvin in its outer parts. The type of elements which condenses in it depends thus on the distance to the star. At this point, we distinguish the cases of rocky planets and giant gaseous ones.

Before summarizing the two scenarios, it is noteworthy that though formation models were based on the unique example of our Solar system for long, the recent discovery of a wide diversity of other planetary systems (including the unexpected *hot Jupiters*) has not fundamentally challenged them. This diversity is assumed to be caused by interactions occuring between the different planets both with the disk during their formation and after their maturation, resulting for example in inward orbital migration, rather than requiring various formation models. Evidence is indeed mounting that catastrophic events, involving planets being pushed into radically different orbits or even expelled altogether out of the system, is a common, and perhaps universal, aspect of planet formation (Lissauer, 1993).

1.4.1 Formation of telluric planets

Rocky planets form from aggregation of solid material present in the protoplanetary disk. Since the inner part of these disks is characterized by hot temperatures, only material whose condensation temperature is above ~ 200 K accrete to form planets. In particular, combinations of iron, magnesium, silicium and sulfur each other and with oxygen represent about 91% in mass of the *rocky* material constituting telluric planets.

Several steps can be distinguished in the process. First, during the *protoplanetary disk* phase, very small *dust grains*, that were already present in the nebula, *sediment* around the median plane of the disk. The action of the central star's gravitational force triggers oscillation of the small dust grains around the median plane of the disk, while frictions with environment gas pull them towards the inner part of the disk, where they sediment. Numerical models assuming no turbulence show that

sedimented grains form objects ranging from a few centimeters to about a meter in size, within a few thousands of years (Weidenschilling, 1980; Nakagawa et al., 1981). However, if turbulence is present, Weidenschilling (1980) showed that sedimentation could not occur, the size of the objects being limited to $\sim$ 1 cm, though they were obtained faster. Recently, Birnstiel et al. (2011) have quantified which conditions, in terms of grain properties, gas pressure gradient, and amount of turbulence were favorable for growth beyond the meter size barrier.

The next step, leading from these objects of the protoplanetary disk to *planetesimals* with size spanning 0.1-1 km is still uncertain, though growth by successive collisions (Dullemond & Dominik, 2005) simultaneous to gas depletion by photo-evaporation (Clarke et al., 2001; Alexander et al., 2006) is the most commonly admitted scenario. Magneto-rotational instabilities have also recently been invoked (Chiang & Murray-Clay, 2007). This phase is known as *transition disk*.

Assuming objects have reached the planetesimal size, collisions are facilitated since their mass is now sufficient to gravitationally deviate their mutual trajectories. Moreover, friction with environing gas is now minor and the corresponding orbital drift can now be neglected in front of mutual gravitational influence. Interactions between planetesimals to form *protoplanets* (size between 10-100 km) are typically studied with the same tools as in *gas kinetics theory* such as the *particle in a box* approximation. Simulations showed that *runaway accretion* around the most massive objects is favoured, they accumulate all the smaller planetesimals of their sphere of influence and become protoplanets.

The last step that leads from protoplanets to rocky *planets* with radius ranging between 1000-10000 km is also dominated by collisions. However, as the number of objects is significantly smaller, N-bodies numerical models can be used. An extensive amount of them has been developed, in particular by Wetherill (1980). Results show that between 2 to 5 telluric planets are usually formed, whether the initial number of protoplanets was 30 (of $10^{-2} M_{\oplus}$ each) or 500 (of $10^{-3} M_{\oplus}$). Timescale for the whole formation process has been estimated to last up to several Gyr, in view of the large number of *debris disks* detected around young stars (Wyatt, 2008).

Although main intervening processes of these different steps seem to be understood, a lot of uncertainties remain.

1.4.2 Formation of giant planets

In outer regions of disks, where the temperature is low enough, volatiles can condense and planetesimals are thought to grow up within a few million years thanks to the large quantities of ices. Two main scenarios are competing concerning their exact formation: the so-called *core accretion* and *gravitational fragmentation* models.

Historically, the latter was first proposed. In this model, giant planets spawn directly from the *gravitational fragmentation* and collapse of the massive proto-planetary disk surrounding the newborn star. Similar to the model proposed by Laplace in 1796, modern version of this theory has been supported by G. Kuiper in the 50's and A. G. Cameron in the 60's and 70's, before he turned to the core accretion scenario.

On the contrary, in the former scenario first quantatively suggested by Cameron (1973) and further comprehensively developed by Pollack et al. (1996), the future core of the giant planet is the product of accretion of solid material (hence the name *core accretion*), in a process relatively similar to rocky planets formation, but with *ices* (i.e. beyond the *snow line*). As the mass of these icy planetesimals raises, so do their gravitational pull. Their mass becomes eventually sufficient to bind some of the

surrounding nebular gas[14], forming a developing *envelope*. Perri and Cameron (1974) have shown that both the gaseous *envelope* and the core grow in mass. During this growing phase, the envelope can be considered in quasi-static and thermal equilibrium as its radiated energy of the gas is supplied by energy released from the core accretion. When the core reaches a critical mass[15], the energy radiated by the gas begins to outpass the accretion energy. As a result, the envelope starts to contract, which in turn augments the gas accretion rate, hence further increasing the radiative energy losses. The process is *running away*, and leads very quickly to a planet with a massive envelope: a *gaseous giant*.

In this model, the formation timescale of giant planets is thus limited by the core accretion phase. A relatively fast core accretion rate is needed before the gas in the disk vanishes and could then not be used to create giant gaseous planets, i.e. within 1.2 to 3 Myr (Mamajek, 2009). The timescale of core formation having to be equal to or shorter than protoplanetary disks lifespan, a rapid growth of the core to reach the critical mass value is thus essential. It is this required fastness that has aroused debate.

Two possibilities exist for the *core accretion* paradigm: either cores grow faster, or disks have longer lifetimes. Fast accretion was thought to occur in priority beyond the *snow line* because more solid material is available for growing (Lodders, 2003) and furthermore explains the dichotomy at 3 AU in our Solar system between the telluric and icy-gaseous giant planets. However, it has also been shown that the core accretion rate is much greater if they are allowed to migrate (Alibert et al., 2004) or in turbulent disks (Rice et al., 2003; Nelson & Papaloizou, 2003), so that giant planets could form well within the disk lifetime. Taking these facts into account, Ida and Lin (2004)'s simulations led to the formation of a relatively wide variety of planets even with the timescale constraint.

While this second theory is more commonly admitted by astrophysicists, the *gravitational fragmentation* model has been dug up by Boss (1997) and further developed as it allows for a quick core formation. It is very difficult to morcelate a disk in order to form planets, as rotating systems are stabilized by pressure forces at small scale and rotation at all scales, preventing thereby gravitational collapse. Disk fragmentation can nevertheless occur when gravitational instabilities in massive protoplanetary disks form, either through dynamical interactions with a passing bare star or surrounded by a disk, or spontaneously through tidal or spiral instabilities. Dynamical simulations of Watkins et al. (1998a, 1998b); Boss (2000) have all shown that this process was possible, provided an initial massive ($\sim 1\ M_\oplus$) disk. Moreover, following the recent discovery of HR 8799b,c and d giants by direct imaging (Marois et al., 2010), Dodson-Robinson et al. (2009)'s simulations have shown that only gravitational instability leading to fragmentation of the protoplanetary disk could succeed at creating massive gas giants on wide, near-circular orbits. However, this last point has to be confirmed by further observations in order to permit the exclusion of the planet dynamical expulsion possibility. More recently, gravitational fragmentation simulations managed to recreate for example both Fomalhaut b and the outermost planets of HR8799 (Nero, 2010). They account thus for giants at extremely large radii, but has failed yet for the innermost ones. On the contrary, core accretion does not allows for the formation of outermost exoplanets detected, as dynamical times involved at very large distance do not provide sufficiently fast accretion rates.

[14]When their thermal motion velocity becomes lower than the escape velocity of the protoplanet. Thermal motion velocity depends on the temperature of the planet, whereas escape velocity depends on the planet's mass. Gases will thus be preferentially kept around both massive and distant planets (relative to their star).

[15]This critical value depends on several physical parameters including the solid accretion rate onto the core. it has been assessed to be of order 15 $M_\oplus$) at 5 AU (Stevenson, 1982).

Examples and simulations in favour of both paradigms have thus not led to consensus yet, though quantitavely more evidence seems to favour core accretion. However, as pointed by Boley (2009), both are not mutually exclusive since one allows for planets in the inner- and the other in the outer- part of systems. Additional observations of disks are in any case needed for better constraints on depletion mechanisms and also to further clarify the relation between disk's timescale and stellar parameters. Additional statistical data would also (as always) be very valuable for better constraints about those formation models. For a comprehensive review of the impact of HC and HAR imaging techniques on the formation and evolution of planetary systems, one should refer to (Absil & Mawet, 2010).

1.4.3 Exoplanets within debris disks

Debris disks are signposts of planets in formation, as confirmed by the imaged exoplanets that came to light in 2008 found in systems hosting bright debris disks. Moreover, the debris disks that have been resolved (e.g. Stapelfeldt et al., 2004; Lagrange et al., 2012) have exhibited asymmetries such as gaps, clumps, truncations or spiral arms, conveying the fact that planets and/or stellar companions are involved. Indeed, gaps in disks are created by planets direct passings, but their presence can also induce clumps and gaps through the phenomenon of resonances, comparable to the Kirkwood gaps in our Solar system's asteroids main-belt. The presence of a stellar companion can truncate the disk or slim it down to a thin annulus. Through tidal effect or secular interactions, it can also spawn spiral patterns in the disk (Beust, 2010).

The most outstanding examples are presented in the next paragraphs. However in most cases, what is seen is only the dust and better characterization requires typically the resolution of inversion problems: inversion of the brightness pattern to determine the dust distribution and then, from the derived structure, calculation of the perturbators (unseen companion, planetoids, planetesimals) position. A typical way of dealing with these inversion problems is the use of specific symplectic integrators [16] (e.g. Beust, 2003).

Fomalhaut b

Fomalhaut is an 200 Myr old A4V star. After the observation of its Kuiper belt-type (outer) debris disk by HST (Kalas et al., 2005) and Spitzer (Stapelfeldt et al., 2004), Quillen (2006) predicted quantitatively the presence of two protoplanetary mass objects to account for the asymmetries observed. Three years later, it was effectively announced from HST observations in optical wavelength taken between 2004 and 2006 (figure 1.12, Kalas et al., 2008). The inner debris disk that has also been predicted was brought to light by NIR interferometry with VLT/VINCI (Absil et al., 2009).

However, one has to be careful with planet *Fomalhaut b*. As dynamical models support the existence of two planets, one at the inner (Fomalhaut b) and another at the outer edge of the outer disk, neither observations in NIR wavelengths, where they are precisely supposed to have their bulk emission, with Spitzer spatial telescope (Janson et al., 2012) nor with ALMA (Boley et al., 2012) have confirmed its existence. It is noteworthy that Janson et al. (2012) used a point-spread function subtraction technique based on angular differential imaging and Locally Optimized Combination of Images, thereby

[16] A symplectic integrator is a numerical method that solves specific differential equations. For planetary systems, this technique takes advantage of the fact that the mass of the central body is much larger than all the other ones. It is not applicable in the case of massive bodies that all have comparable masses, such as in multiple stellar systems.

using similar tools as presented in this work, in order to substantially improve the Spitzer contrast at small separations. The most probable scenario to account for the HST observations is the existence of an extended source such as an exozodiacal disk (Absil et al., 2011) or a transient/semi-transient dust cloud (Janson et al., 2012) which scattered light from the star.

Nevertheless, observed dust particles in the dist must be kept within the dist by the gravitational effect of two planets, so that the closer to the star must have approximately the same orbit as the announced Fomalhaut b. Though none of these two planets have been imaged for sure, we will refer to Fomalhaut b as the object, albeit smaller, orbiting at the same distance than the previously announced one.

Beta Pictoris b

As mentioned in section 1.2, the disk of A6V type β Pic was the first one to be resolved (Smith & Terrile, 1984), and the only one for about 15 years. Its extensive study has led to an accumulation of evidence indicating the presence of a planet such as the 5 warp seen in the inner disk up to ∼80 AU (Heap et al., 2000) and presence of a bright mid-infrared clump (Telesco et al., 2005). Dynamical models of Freistetter et al. (2007) have then predicted the presence of a Jupiter-sized planet oriting at about 12 AU from the star.

At this stage, the only thing lacking was the image which was eventually provided by Lagrange et al. (2009), who revisited VLT/NACO deep L-prime band images (figure 1.12). The planetary companion is the bright spot on the upper-left of the image and is calculated to be orbiting at about 8 AU from its star. A year later the prediction turned out to be correct, with the reappearance of β Pic b on the other side of the star (figure 1.12, Lagrange et al., 2010). Its mass has been evaluated to $\sim 8\ M_J$ and the semi-major axis of its orbits has been refined to ∼9.55 AU. not in the main disk but in its inclined component (Lagrange et al., 2012). Its L' magnitude of 11.2 suggests a temperature of approximately 1500 K.

HR8799 b, c, d and e

HR8799 is the directly imaged system possessing the most important number of exoplanets. The three first ones, *b*, *c* and *d*, were announced by Marois, Macintosh, et al. (2008). They orbit respectively at 68, 43 and 27 AU from their A5V star. The most recent estimates of their masses and radii provide respectively 7.0 M_{Jup} / 1.1 R_{Jup}, 10.0 M_{Jup} / 1.3 R_{Jup} and 10.0 M_{Jup} / 1.2 R_{Jup} (Marley et al., 2012). Since then, a fourth planet, *e*, has also been unveiled in the HR8799 system, whose orbital distance and mass are estimated respectively to 14.5 AU and 9 M_{Jup} (Marois et al., 2010).

Su et al. (2009)'s thorough study of the HR8799 disk with Spitzer highlights the existence of an inner dust ring, a dust-free region from 20 to 90 AU within which planets b, c and d orbit, and outer ring extending to 300 AU, and an additional exterior distribution produced by radiation pressure expelling small grains from the outer ring. This work shows the synergism achieved by studying a system known to have both a debris disk and several planets. These results were also used to test and constrain models of the dynamics and evolution of young planetary systems (see e.g. Dodson-Robinson et al., 2009).

The examples listed hereabove had a huge impact on the scientific community[17], conveying the importance of imaging additional exoplanets around young stars, especially when they are displaying debris disk, as they enable to improve our understanding of the processes governing the evolution of planetary systems. These facts justify the choice of the different targets of our study, presented in section 4.1.

[17] As e.g. the 406 articles citing the discovery of HR8799 (Marois, Macintosh, et al., 2008) testify (ADS, as of August 5, 2012).

Chapter 2

Observation techniques

High-dynamic range and high-angular resolution imaging with a mono-pupil telescope requires specific tools in order to achieve the performances required to detect planets. In this chapter, we present an overview of adaptive optics systems, enabling to reach high angular resolution, stellar coronagraphy, used to achieve high-dynamic range acquisitions, and the different observing strategies optimized for HC and HAR imaging from the ground. Finally we discuss the topic of data reduction focusing on LOCI.

2.1 Adaptive optics

The general trend about telescopes is that astronomers always want them larger. Not only a larger primary mirror enables to collect more light, but as it is showned by equation (1.9), angular resolution is inversely proportional to the diameter of the telescope. However, as this angular resolution seems to be governed by the theoretical diffraction limit, in practice *atmospheric turbulences*, if not treated, will perturb the incoming wavefront in such a way that the performances of the largest telescopes can be reduced down to those of a simple 20-cm amateur device. AO systems are a way to deal with these turbulences, in real-time, in order to restore the full resolution of the telescope. The only other way to solve the atmosphere issue is to go in space, which explains the craze about space-borne observatories (HST, Spitzer, the upcoming JWST to cite but a few those in the relevant wavelength range of this work).

Before exploring in detail of what AO systems are constituted, we define what it is not. Adaptive optics has not to be confused with *active optics*, which is also an indispensable tool of 8m-class telescopes. The latter is the technology used to prevent deformations of the primary mirror and operates to compensate larger amplitude aberrations. These distortions can be due to mechanical shearing, temperature variations or wind. The timescale of these corrections is relatively longer ($\sim$ 1 s) as those variations are slower than atmospheric turbulences.

Figure 2.1 provides a sketch of the different components of an adaptive optics system. Incoming wavefronts from the observed target is first distorted by the turbulences operating in the different layers of the Earth's atmosphere. When they arrive in the telescope, they are reflected by the primary and secondary mirror (M1 and M2). Then begins the AO loop. The tip-tilt mirror (TTM) and the deformable mirror (DM) correct respectively the overall WF tilt wobbles and higher orders fluctuations.

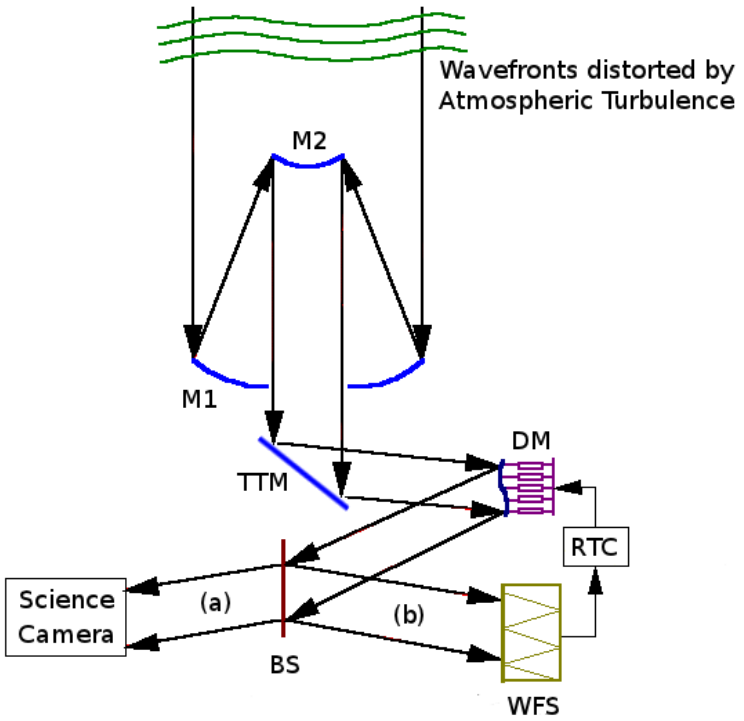

Figure 2.1: Simplified diagram of an AO System. Distorted wavefronts arrive in the telescope, they are reflected by the primary and secondary mirror (M1 and M2), the tip-tilt mirror (TTM) and the deformable mirror (DM). The light is then separated by a beam splitter (BS). The transmittive part goes to the science camera, whereas the reflective part is used to feed the wavefront sensor (WFS). A real-time computer (RTC) allows to provide proper corrections to the DM.

The light is then separated by a beam splitter (BS). The transmittive part goes to the science camera, whereas the reflective part is used to feed the wavefront sensor (WFS). This WFS measures WF distortions and these measurements are processed by a Real-Time Computer (RTC), which allows then to provide proper corrections to the actuators of the DM.

2.1.1 Origin of the aberrations

Atmospheric turbulences

Atmospheric turbulences originate from wind shearing in two well-defined layers of the troposphere (0-12km): close to the ground and at the jet stream layer. Because of the random nature of turbulence, one needs a statistical approach to describe it. This statistical approach can be based on *structure functions*, which are the mean of the square of the refractive index difference between two locations separated by r :

$$D_n(r) = \langle \left[n(\mathbf{r} + \mathbf{r}') - n(\mathbf{r}') \right]^2 \rangle \tag{2.1}$$

where $n(r)$ is the refractive index and the angular brackets mean an ensemble average. One may notice the close similarity with the covariance function. Assuming Kolmogorov turbulence, the structure function takes on a particular form, *Obukhov's law* (Obukhov, 1959):

$$D_n(r) = C_n^2(z) r^{2/3} \tag{2.2}$$

where C_n^2 is the refractive index structure constant and r comprised between 1 to 12 km. C_n^2 is a measure of the strength of the turbulence, varying with seasons, nightly, hourly and with altitude z, thereby anything but constant. It is the vertical profile of the turbulence.

We do not attempt to provide a comprehensive picture of atmospheric turbulences as it is clearly out of the topic of this thesis. However, we define hereunder both spatial and temporal parameters that are relevant in the context of AO, and in particular to characterize the optical quality of a given sky.

Fried's parameter r_0 is defined in the Kolmogorov paradigm as (Fried, 1966):

$$r_0 = \left[0.423 k^2 X \int_{Path} C_n^2(z) \mathrm{d}z \right]^{-3/5} \tag{2.3}$$

where k is the angular wavenumber, equal to $\frac{2\pi}{\lambda}$, X is the airmass, equal to $\sec\zeta$ (with ζ the angle of the telescope measured from zenith) and C_n^2 is the above-described refractive index structure constant. The integral of $C_n^2(z)$ along the line of sight gives the integrated strength of the turbulence.

r_0 corresponds to the size of a region over which the phase variance $sigma^2$ is 1 rad. In other words, the incoming WF can be considered flat over an area of order r_0. In consequence, r_0 represents the size of a telescope which can operate at its diffraction limit. Any telescope with diameter larger than r_0 will have an angular resolution $\sim \lambda/r0$ instead of $\sim \lambda/D$. r_0 is about 10-20 cm at 500 nm and about 60 cm at 2.2 μm above good locations such as Paranal. Therefore, if atmosphere turbulences are not corrected, even the largest ground based telescopes have a resolution that is no better than a 20cm-telescope. We also see the polar importance of r_0 in the design of the AO system's DM, in particular for its number of actuator (see section 2.1.5). Since r_0 is proportional to $\lambda^{6/5}$, we also note that AO correction is *a priori* easier at IR wavelength than in optical (excluding the difficulty linked to less sensitive detectors).

The *seeing* β is directly related to r_0:

$$\beta = 0.98 \frac{\lambda}{r_0} \tag{2.4}$$

It provides the typical angular resolution that can be reached, without AO correction, for the given atmosphere conditions. A seeing of 1" is considered relatively good, and a seeing of 0.4-0.5" corresponds to the best observation conditions that can be found on Earth (La Palma, Mauna Kea, Paranal).

The *isoplanatic angle* θ_0 represents the angle above which the lightpath of 2 sources separated of θ_0 are considered uncorrelated, so that no *guide star* separated by an angular distance greater than θ_0 from the science target should be used for AO corrections. It is given by (F. Roddier et al., 1982):

$$\theta_0 = 0.314 \frac{r_0}{\bar{h}} \tag{2.5}$$

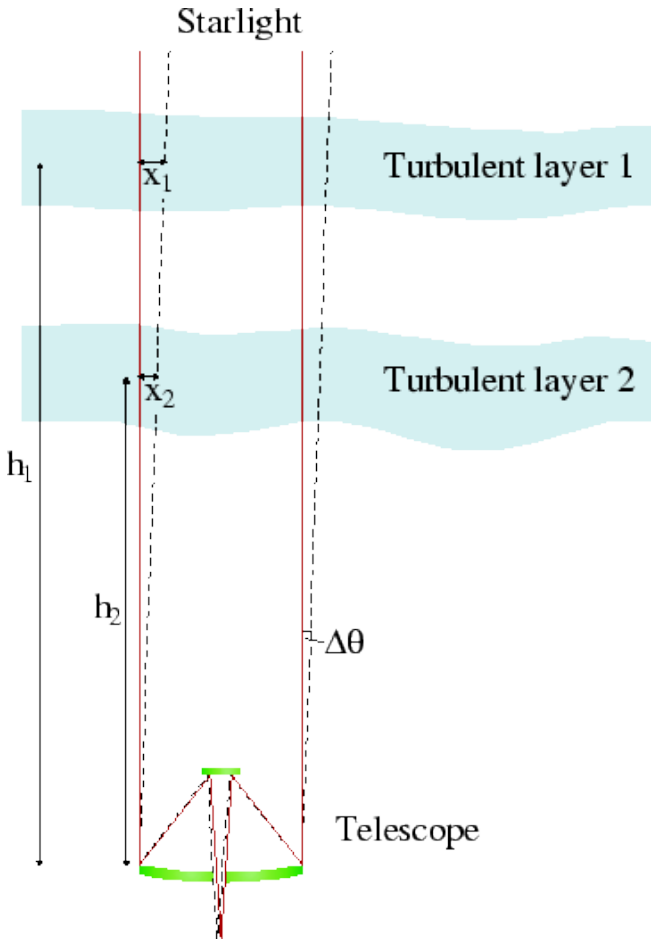

Figure 2.2: Sketch representing the concept of isoplanatic angle. The angular separation $\Delta\theta$ between guide star and science target has to be smaller than θ_0 in order to allow the guide star to be used for AO corrections.

where $\bar{h}$ is the weighted scatter of the turbulent layer heights h_1 and h_2 (figure 2.2). As r_0 depends on wavelength as $\lambda^{6/5}$, $theta_0$ varies with wavelength in the same way. Taking into account the hidden appearances of the airmass in r_0 and Δh, θ_0 depends on $X^{-8/5}$. In total, the average $theta_0$ in Paranal is about 15-30" at 2 μm.

If the turbulence moves over the telescope faster, the speed at which the wavefront needs also to be AO-corrected faster, and vice-versa. The *Greenwood frequency* is the frequency or bandwidth required for optimal correction. Its inverse is called the *coherence time* τ_0, or Greenwood time delay. It depends on the transverse windspeed and the turbulence strength in the atmosphere (Greenwood, 1977):

$$\tau_0 = 0.314\frac{r_0}{\bar{v}} \tag{2.6}$$

where $\bar{v}$ is the velocity weighted over the different turbulence layers. On Paranal, τ_0 is typically varying

at 2.2 μm from a few ms (high wind or jet-stream, bad conditions) to 60 ms (good conditions). r_0 depending on wavelength as $\lambda^{6/5}$, so does tau_0. Again, we notice that AO is easier at IR wavelengths.

In summary, both τ_0 and r_0 are critical parameters. The larger they are the more stable the atmosphere is and the better the performance of the AO system will be.

Optical aberrations

Aberrations, amplitude or phase errors, are not only introduced by the atmosphere, but also by the instrument. In the latter case, one is dealing with the *optical aberrations*, which are characterized by optical testings. Classical methods of optical testing mainly involve the measurement of the shape of the tested surface. Examples of *classical tests* are the Foucault test, the null test, the Ronchi test (Ronchi, 1964), the Hartmann test (J. Hartmann, 1900)[1] and the Roddier test (C. Roddier et al., 1990)[2].

In the case of instruments attached to the telescope, another point to be corrected consists in the mechanical flexures undergone by the the optical elements as the telescope rotates and hence triggers a variation of the gravity vector. The differential flexures between the WFS detectors and the science detector are usually the most critical issue to deal with. To correct for it, the AO loop pre-compensates for these flexures using calibrated pointing models.

Finally, the so-called *non-common path aberrations* have also to be corrected in order to reach the best image quality. These aberrations appear in the lightpath either between the BS and the science camera (part (a) in figure 2.1), or between the BS and the wavefront sensor (part (b) in figure 2.1). In the first case, they are not seen by the AO system as they are out of the *loop*. These aberrations can typically be due to collimator, masks, filters and camera of the science detector. In the second case, the aberrations are seen by the WFS but are *erroneously* corrected as the part of the beam that goes to the science camera is not affected by those aberrations. In that part of the system, aberrations are typically caused by the reflecting surface of the dichroic used or the mis-alignment of the WFS sub-pupils. Whereas aberrations introduced by the latter can be dealt with a calibration lamp located upstream, for the aberrations coming from optical elements in the optical path of the detector (i.e. after the dichroic), the WFS is of no use. A solution allowing to determine those residual aberrations directly on the science camera is therefore the most appropriate. This requires typically the use of *phase diversity* techniques (see e.g. Carreras et al., 1994; Kendrick et al., 1994 or the first calibration of NACO's static aberrations, Blanc et al., 2003; Hartung et al., 2003).

[1] The Hartmann test places a perforated screen in the lightpath, creating rays when the light goes through it, in order to perform a kind of *ray-tracing* analysis. Its evolution, the Shack-Hartmann sensor, can be used with very low illumination, using this time an array of lenslet (J. Hartmann, 1900; Shack & Platt, 1971). As it is also used as WFS, it is further detailed in section 2.1.3

[2] The Roddier test is based on the fact that a symmetric measurement of the intensity before (intra-focal) and after (extra-focal) the focal plane of the system should give same intensities in the case of a perfect system. This method also revealed usable to test optical surfaces, though first designed for adaptive optics wavefront sensing (C. Roddier et al., 1990). This method is further developed in section 2.1.3

Characterization of the aberrations

Aberrations can be expanded in polynomial series, whose sum constitutes the wavefront. A well-known basis of orthogonal polynomials was invented by Zernike (Zernike, 1934). His polynomials are particularly fitted to full circular pupils. Since most of modern telescopes are centrally obscured, the set of polynomials introduced by Mahajan (1981) may be more convenient. Zernike polynomials are characterized by two indices, however using the nomenclature introduced by Noll (1976), aberrations can be mathematically represented by a single index:

$$\phi(\mathbf{u}) = \sum_{i=2}^{k} a_i Z_i(\mathbf{u}) \tag{2.7}$$

Noll's notation labels the focus with i=4, the tangential and sagittal astigmatism with i=5 and 6, coma with i=7 and 8, and so on. In order to describe any wavefront form, k should in theory tend to infinity, but can in practice be truncated after a few dozens.

2.1.2 Guide stars

In figure 2.1, we assumed that the target star was bright enough in order to use a given percentage of its flux to supply the AO loop. However, it is more likely that this reference star is not the target object itself, but a close by star since science objects are often very faint, and required time samplings to correct for the turbulences would not provide enough photons in each sub-aperture of the WFS. The closeness of the reference star that can be taken is defined by the so-called *isoplanatic angle* (figure 2.2). The probability that a sufficiently bright star is located within the isoplanatic angle is relatively low. To overcome this difficulty, AO module may sometimes be fed by an artificial sodium *laser guide star* (hereafter LGS), such as the one that equips VLT/UT4.

This LGS is focused at 90 km altitude in the mesosphere and specifically tuned to 589.2 nm in order to excite the sodium layer, naturally present in the mesosphere at this altitude. It provides a V$\sim$ 12$\pm$1 artificial star positioned on sky on top of the science target allowing high-order AO corrections. Due to the bright artificial star that is created near the centre of the field, the probability to achieve a given minimum AO correction on an arbitrary astronomical target, goes e.g. to obtain corrected images with at least a 20 % K-band Strehl ratio, from 3 % with an NGS to 65 % with an LGS (Girard, 2011).

Nevertheless, an NGS is still required to correct for the tip/tilt motions. Indeed, they are not sensed by the LGS because the paths of the light rays are the same on the way up as on the way down, triggering an apparent stationary centroid of the artificial light spot in the sky, while the apparent position of an astronomical source suffers lateral motions (the so called *tip/tilt*). Therefore, the simplest solution is to supplement the AO system using the LGS with a tip/tilt corrector set on a faint close (V=17 or brighter) star. Performance is then limited by the poor photon statistics for correcting the tip/tilt error. This tip/tilt star can be as far away as 40 arcsec from the science target (depending on the wavelengths used), but with decreasing performance with increasing distance. This necessity for an NGS for tip-tilt sensing accounts for the impossibility to get 100 % of sky coverage, even for LGS-AO.

2.1.3 Wavefront sensors

In order to correct the phase aberrations introduced by the atmosphere, a wavefront sensor (WFS) is required. Direct sensing of a wavefront is not possible at optical frequencies, because the wavefront *phase* does not interact with matter in any measurable way, instead, the wavefront must be deduced from intensity measurements at one or more planes.

As for AO systems, one can distinguish interferometric and non-interferometric WFS. The former employs a direct approach where there is an explicit determination of the phase or OPD (optical path difference) of the wave using interferometry with narrow-band lasers. The latter, on which we focus in the framework of this thesis, can in turn be classified in two main groups: slope and curvature based sensors. The main representatives of the two groups are respectively the aforementioned Shack-Hartmann and Roddier wavefront sensors, although another type of slope sensing WFS has appeared recently: the *Pyramid* WFS (Ragazzoni & Farinato, 1999). In the case of small-angle coronagraphy, an additional low-order WFS is also needed (Mawet, Pueyo, et al., 2012).

A WFS channel does generally not only include the WFS unit(s) but also a *field selector* (hereafter FS) and, in the case of different units, a WFS selector mirror. The role of the FS is to select the NGS described in previous section. For example, VLT/NAOS, the AO system of NACO, is composed of two WFS units: one infrared (0.8-2.5 μm) and one visual (0.45-1.0 μm) Shack-Hartmann WFS.

Shack-Hartmann WFS

The *Shack-Hartmann WFS* is born from the necessity to perform wavefront testing with very low illumination. Based on the Hartmann method, Shack and Platt (1971) proposed to replace the screen with an array of small lenses, and the photographic plates with a CCD camera (figure 2.3). Each sub-pupil causes a spot to form on the detector. The calculation of the exact angular displacement α of the position of each of these spots (or centroids) then provides a slope estimate for the wavefront of each sub-aperture. In the x direction, we have:

$$\alpha_x = \frac{c_x}{fM} = \frac{\lambda}{2\pi A_{sa}} \int_{sa} \frac{\delta\phi}{\delta x} \mathrm{d}x\mathrm{d}y \tag{2.8}$$

where c_x is the spot displacement, f the lenslet focal length, M the magnification between the lenslet plane and the telescope entrance plane and $A_s a$ the subaperture area. The same equation can be written for the y-axis. The integration allow then to recover the phase.

The Shack-Hartmann WFS is the most used WFS among AO systems. Examples include COME-ON (Kern et al., 1989), ADONIS (Beuzit et al., 1994), Gemini AO system (Herriot & Morris, 1997), Keck AO system (van Dam et al., 2004), VLT/NACO/NAOS (Rousset et al., 2003) and VLT/SPHERE/SAXO (Fusco et al., 2006). In the case of NaCo, both visible and infrared Shack-Hartmann WFSs include two lenslet array pupil samplings: 14x14 (144 valid subapertures) and 7x7 (36 valid subapertures). The reason of the choice between two different samplings is to cover a wider magnitude range. The 7x7 configuration allows to achieve a substantial correction with faint NGS while the 14x14 subaperture configuration is more adapted for bright NGS (Girard, 2011).

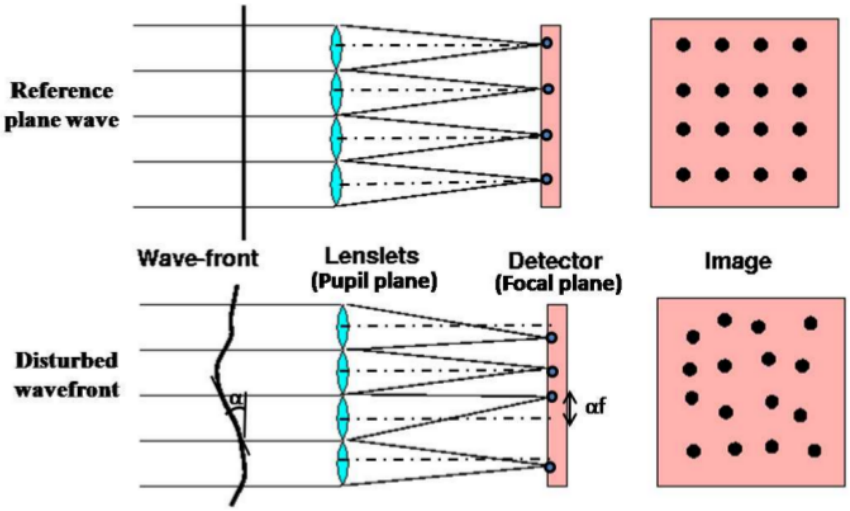

Figure 2.3: Simplified diagram of a Shack-Hartmann WFS. An array of lenslets divides the incoming WF in small local wavefronts. If the incoming WF is planar, each local wavefront will be focused on its lens axis. On the other hand, if the incoming front is distorted, the lenses will focus the local front somewhere else. The position of the spots is related to the slopes of the corresponding local wavefront.

Pyramid WFS

The pyramid wavefront sensor was introduced by (Ragazzoni & Farinato, 1999). It is based on the same principle as the Foucault knife-edge test used for optical lens testing. The principle of operation is shown in figure 2.4. The wavefront coming from the telescope is focused into the focal plane, where a four-face pyramidal prism is placed with its vertex at the focal point. The four faces of the pyramid deflect the light in slightly different directions. A lens relay placed after the pyramid is used to produce four images of the exit pupil on a CCD detector allowing the adjustment of the scaling (number of pixels across the pupils). The vertex angle of the pyramid must be slightly less than 180 to avoid overlap between the pupil images. The differential intensity between pairs of pupils is related to the wavefront gradient along the x and y axes. Again, the integration enables finally to recover the phase.

The main drawback of this technique, as one can guess, is the difficulty to design such WFS. In particular, the vertex must show no imperfection. The LBT is currently using a Pyramid WFS in its AO system (Esposito et al., 2011).

Curvature WFS

The curvature wavefront sensor was developed by F. Roddier (1988). A schematic diagram is provided in figure 2.5. Two intensity measurements are recorded in the planes $P1$ and $P2$, at a distance l respectively before and beyond the focal plane (figure 2.5). A local curvature of the wavefront modifies the rays convergence and divergence in the respective planes, leading to a local excess of illumination in plane $P1$ and a lack of illumination at the corresponding position in $P2$, or vice-versa. As the relation between the two illuminations and the WF curvature is linear, their difference gives

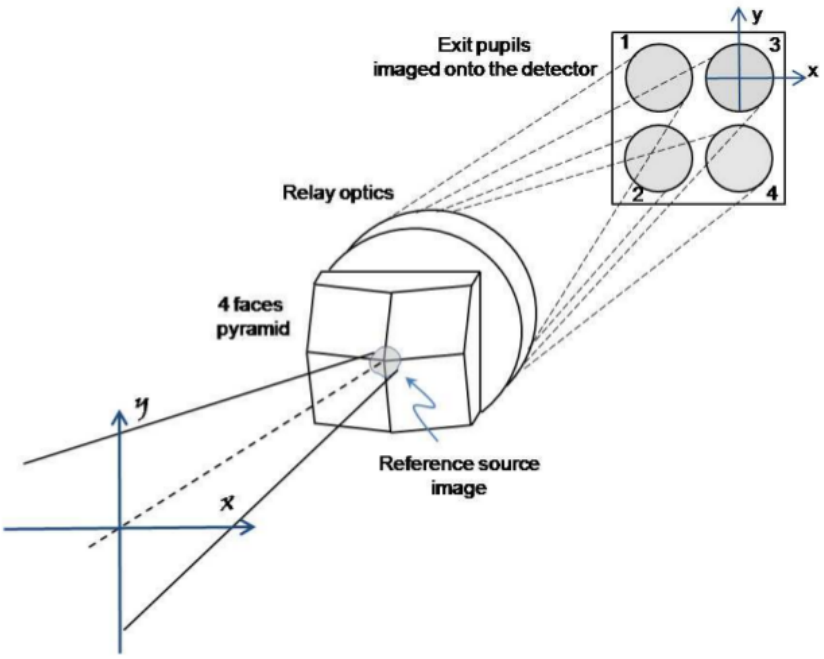

Figure 2.4: Simplified diagram of a Pyramid WFS. The reference source is imaged on the pyramid vertex, which deflects the light in four directions. The relay optics enables to reimage the deflected wavefronts in four exit pupils (Ragazzoni & Farinato, 1999).

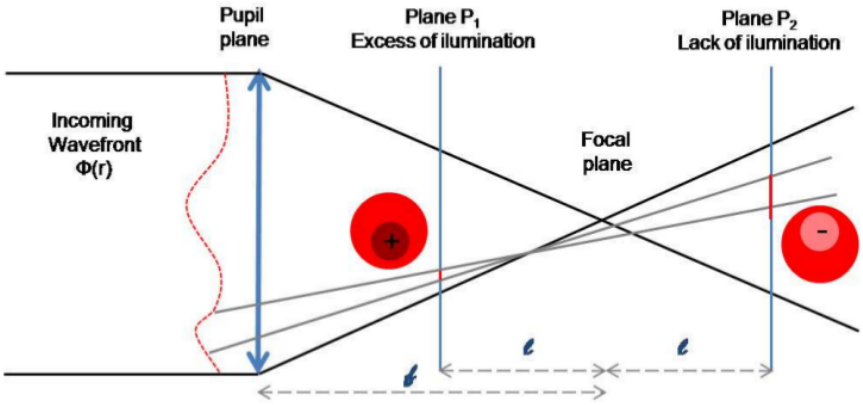

Figure 2.5: Simplified diagram of a curvature WFS (inspired from F. Roddier, 1988).

directly the local WF curvature.

Practical implementation of this method makes use of a vibrating membrane mirror placed at the telescope focus, followed by a collimating lens, and a lens array. The defocused distance can be chosen by adjusting the vibration amplitude in order to conjugate the defocalized sensing planes on the lenslet array. ESO's MACAO system currently uses curvature WFS (Bonnet et al., 2003).

2.1.4 Wavefront reconstruction

As we mentioned that most WFS were of Shack-Hartmann type, we focus on this unique case for the reconstruction. At this stage of the optical path, the WFS has thus gathered WF slopes. Now, they have to be converted into commands for the DM:

$$\mathcal{S}_{x,y} \xrightarrow{\mathcal{R}} \mathcal{V} \tag{2.9}$$

where $\mathcal{S}_{x,y}$ represents the slope space, $\mathcal{V}$ the voltage (or commands) space, and $\mathcal{R}$ is a linear application that goes from slope to commands space. This linear relation can be expressed using matricial formalism as:

$$\mathbf{v} = \mathbf{R}\mathbf{s} \tag{2.10}$$

where $\mathbf{s}$ is the slopes vector $\{s_x^1, ..., s_x^{ns}; s_y^1, ..., s_y^{ns}\}$, ns the number of subapertures, $\mathbf{v}$ the vector of voltages $\{c^1, ..., c^{na}\}$, na the number of actuators and $\mathbf{R}$ is the reconstructor or control matrix. The mathematical computation of $\mathbf{R}$ and the conversion between slopes and commands is known as *wavefront reconstruction*.

The inverse of $\mathbf{R}$ is the interaction matrix $\mathbf{M}$, of dimension $2ns$ x na. The latter is determined during the calibration of the AO system by pushing one by one the different actuators of the DM and looking at the slopes on the WFS. In practice, several actuators defined by Hadamard matrices can be pushed at the same time in order to allow a faster computation. The determination of $\mathbf{R}$ from $\mathbf{M}$ is an *inversion problem*. The linear system that represents actuators and slopes is overdetermined (there are more WFS signals than actuators). Hence, matrix $\mathbf{M}$ is not invertible since it is not square

and usually bad conditioned. The most common way to invert $\mathbf{M}$ is to use the so-called *singular value decomposition*, whose description is however out of the topic of this thesis.

Assuming $\mathbf{R}$ is known, according to *control theory*, we can now express an AO system as a *servo loop*, where the input is the wavefront phase perturbation and the output is the residual correction. In most cases, a first-order servo-loop containing an integrator as feedback law is used. In a discrete time system, this integrator corresponds to summation:

$$\mathbf{v}(i) = \mathbf{v}(i-1) + \alpha \mathbf{R}\mathbf{s}(i) \tag{2.11}$$

where $\mathbf{v}(i)$ is the vector of voltages for the current iteration i, $\mathbf{v}(i-1)$ is the vector of voltages applied on the previous iteration, $\mathbf{s}(i)$ is the slopes vector on the current iteration and $\mathbf{R}$ is the reconstructor. α is a scalar gain between 0 and 1 used to lower the global matrix gains in the closed loop, giving stability but reducing performance. This gain is adjusted depending on the observing conditions. Indeed, considering the readout time of the camera and the RTC computation time, the provided correction by the AO system exhibits generally a delay of order 2 ms[3], which can be not negligible in the case of short coherence time (defined in section 2.1.1) due to bad or average observing conditions.

The output residual phase ϕ_{res} in each iteration is given by:

$$\phi_{res} = \phi_{turb} - \phi_{corr}$$

with ϕ_{turb} being the input turbulent phase and ϕ_{corr} the corrective phase provided by the AO system.

Since the beginning of this chapter, we have assumed an AO system working in closed-loop. Nevertheless, AO control may also use open-loop, i.e. the WFS is before the DM in the optical path. However, we will focus only on the latter case, as the large majority of systems are implemented with closed-loop. As pictured in figure 2.1, the first component in the optical system is the DM. which compensates the wavefront errors on the incoming beam before it is sampled and measured by the WFS. Therefore, the WFS only sees the residual error; that is, the difference between the current incoming wavefront and the last correction applied to the DM. This error is processed to update the control signals applied to the DM. On this arrangement, the WFS only needs to detect small deviations (which makes this configuration more advantageous than the open-loop).

2.1.5 Deformable mirrors

Provided a wavefront reconstruction system, a phase correction device is needed in order to compensate for the distortions in the wavefront. The easiest way consists in using both a tip-tilt (TTM) and a deformable mirror (DM), which correct respectively the low-[4] and high-order aberrations. Such devices introduce an optical phase shift ϕ by producing an optical path difference δ, through $\phi = 2\pi\delta/\lambda = 2\pi\ ne/\lambda$, with n the refractive index and e the geometrical path, which is modified by *poking* the actuators of the DM.

DMs basically consist of a segmented or continuous reflective faceplate (i.e. surface mirror) coupled to an array of actuators that perform the deformation. These actuators are either piezo-electrical, electrostatic or electromagnetic. The main characteristics which determine the performance of a

[3]For example, VLT/NAOS can run at 480 Hz at its most (Girard, 2011).

[4]The so-called *tip* and *tilt*, which are terms associated respectively to $i = 2$ and 3 in Noll's decomposition of the aberrations in the Zernike basis (equation (2.7)).

wavefront corrector are the number of actuators, the stroke of each actuator, influence functions, actuator coupling and temporal frequency response.

The *number of actuators* represents the degrees of freedom within the active area and is the basic descriptor. The actuator pitch d in relation to the value of r_0 determines the fitting error. Full wavefront compensation requires an effective actuator spacing of 1-1.5 r_0. This implies that larger is the telescope, greater is the required number of actuators.

The *stroke* is the dynamic range of the deformation. We can distinguish two types of strokes: the interactuator stroke corresponds to the maximum displacement between two adjacent actuators (individual actuator stroke) and is always less than or equal to the mechanical stroke defined as the maximum range over which all of the actuators can move collectively, i.e., simultaneously applied with the same driving voltage. The stroke required is defined by the standard deviation of the turbulent wavefront σ. Note that the stroke of the mirror is half the phase change to be placed.

The shape of a deformable mirror surface, when it is pushed by an actuator, is called its *influence function* (hereafter IF). It defines the spatial response of each actuator and is a function of mirror faceplate parameters, as thickness, stiffness or modulus of elasticity. The shape of the IF determines how well the DM is able to take on the shape of the turbulence.

Actuator coupling shows how much the movement of one actuator will displace its neighbors. It is defined as the ratio of the faceplate deflection produced by an actuator A_i at the position of an adjacent actuator A_{i+1}, to that of the maximum peak deflection of A_i.

Finally, the *temporal response* of the deformable mirror is also important, as it is also to be taken into account in the total to be compared with the turbulence coherence time. Small mirrors usually have higher bandwidth.

2.1.6 Performances of AO systems

The main figure of merit used to quantify the performance of AO systems is the *Strehl ratio* (hereafter Sr). In a more general context than AO, it can also be used to estimate the quality of any image. It is defined as the peak intensity of a measured PSF to the peak intensity of a perfect diffraction limited PSF for the same optical system:

$$Sr = \frac{I(\mathbf{x} = 0)}{P(\mathbf{x} = 0)} \tag{2.12}$$

where $\mathbf{x}$ stands for the position vector, $I(\mathbf{x} = 0)$ for the maximum intensity of the measured PSF and $P(\mathbf{x} = 0)$ for the maximum of the diffraction limited PSF.

An equally often used way of estimating the Sr is the so-called Maréchal approximation, which gives an alternative expression based on wavefront errors:

$$S = \exp[-\sigma_\phi^2] \exp[-\sigma_\chi^2] \tag{2.13}$$

where σ_ϕ^2 is the wavefront phase variance and σ_χ^2 is the variance of the log-normal amplitude at the pupil plane (Marechal et al., 1994). It is valid when the Sr $> 10\%$ or $\sigma_\phi^2 < 2.3$. A consequence of the Maréchal approximation is that the total Sr of an instrument is the product of the Sr of its n individual optical elements as long as the phase errors of each component are uncorrelated (ie: $\phi = \phi_1\phi_2...\phi_n$).

However, one has to be careful with Sr ratios, as its different techniques of computation, based on either equation (2.12) or (2.13) can yield significantly different results (Roberts et al., 2004).

Excluding atmospheric conditions, the overall performance of an AO system depends on the characteristics of each of its components: the number of lenslets in the WFS lenslet array, the number of actuators behind the DM, and the rate at which WF reconstruction (measuring, processing and correcting the phase errors) and DM shaping are performed.

For the detection of exoplanets, the quality of the corrections is primordial as uncorrected aberrations lead to a bright quasi-static pattern around the observed source (see next section). In turn, these bright spots, called *speckles*, curb the resolution of the image, as regions close to the source object are lost in this luminous pattern. For Jupiter-type planets around solar-type stars, specifications of the *Planet Finder*[5] for second generation VLT/SPHERE instrument ($\sim$ 1000 actuators) are to reach Sr=95% (Mouillet et al., 2004). By contrast, current on-sky performances of VLT/NAOS (14x14 WFS sub-apertures, 185 actuators) reach about $\sim$40% in H-band, $\sim$60% in Ks-band and $\sim$80% in L'-band with average seeing ($\leq$0.6") and coherence time

However, as Girard (2012, in release) pointed out, it is difficult to talk about nominal on-sky AO performances, since they depend on a large number of parameters such as the atmospheric conditions, airmass, sky transparency, brightness of the guide star, angular distance between the reference source and the science object. The Sr is the appropriate metric for diffraction limited imaging, but in the case of very high contrasts, the best metric becomes the intrinsic contrast at a given separation of the residual wavefront error measured by the WFS in nm.

As for AO systems coupled with observations in the IR, one has to deal with modest detector cosmetics and both high and variable backgrounds, even more than for non-AO IR observations. Indeed, the IR background is higher for an IR instrument with an AO system because of the additional optics in an AO system. Frequent backgrounds have to be acquired (at least once a minute), requiring offsets, and poor results are obtained if one does not offset frequently or if the time scale for fluctuations in the L-band background is short (Girard, 2011).

2.1.7 Speckles

Speckles (figure 2.6) are the manifestation of wavefront aberrations, in the image plane. They take the form of bright spots of typical size $\sim \lambda/D$ and whose brightness depends on the brightness of the star, the fraction (1-S) of residual light in the halo and the angular distance to the star. They are due to atmospheric and instrumental causes.

Adaptive optics can reduce significantly, but not totally aberrations due to atmospheric turbulences. As coherence time of atmospheric turbulence occurs at a timescale of order 10ms, *atmospheric speckles* are said to be *short-lived*. Therefore, the stray light pattern averages itself out into a smooth halo over the course of the observation. However, it is rather simple to deal with those speckles, as a first order solution consisting in applying a high-pass spatial frequency filter subtract relatively well these halos.

On the other hand, the so-called *quasi-static speckles* are typically due to the secondary mirror's

[5] *Planet Finder* project consists of two preliminary studies about the achievements needed in order to image planets, and whose results eventually led to the implementation of instrument SPHERE.

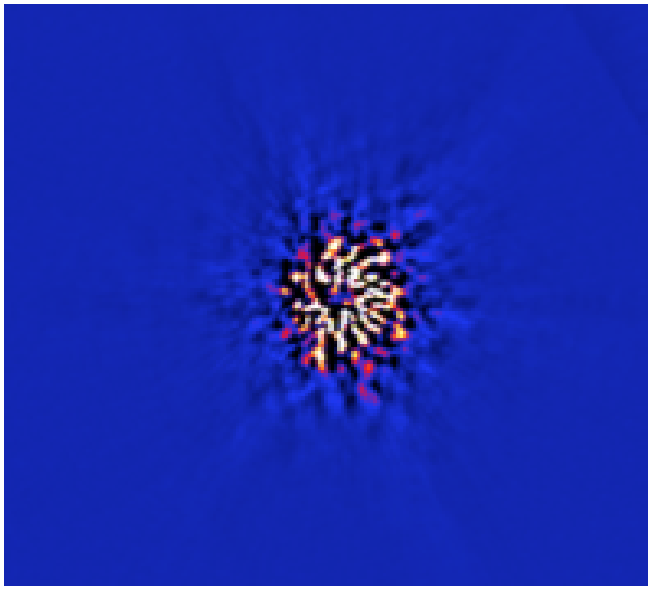

Figure 2.6: Example of speckle pattern, curbing the detection of exoplanets at close angular separation from the star (credit: D. Mawet).

mechanical support (the *spiders*), imperfections of the telescope mirrors (optical testing is never perfect) and NCPAs. They are more problematic to deal with as they do slightly vary with time, on timescales that range from minutes to hours (e.g Fitzgerald & Graham, 2006; Hinkley et al., 2007), because of temperature or pressure fluctuations, mechanical flexures, moving optics (e.g. the Nasmyth mirror), guiding errors, or other phenomena (see Marois et al., 2005, 2006), hence the *quasi-static* denomination. In the case of high-contrast imaging, quasi-static speckles add themselves coherently and become dominant over signals that add incoherently, such as photon noise of the diffraction wings, sky, readout noise and atmospheric speckles (Macintosh et al., 2005), thereby forming a central bright quasi-static pattern. This fact prevents a gain with increasing integration time (Marois et al., 2005) and has the unwanted effect that true companions cannot be distinguished from those artifacts. It depends on the dwell time of the speckle pattern, the brightness of the star, and the fraction (1-S) of residual light in the halo (S being the Strehl ratio of the image).

The bright swarm of quasi-static speckles can be dampen either thanks to better NCPA calibrations applied to the instrument, or by appropriate observing strategy and data reduction, which are described in the two next sections.

It is noteworthy that as the general trend consists in suppressing the speckles, in particular to find exoplanets, Labeyrie (1995) has on the opposite proposed to take advantage of it, through a technique called *dark speckles*. The bright halo of scattered light is constituted of speckles whose luminosity varies statistically over time, at short timescale for atmospheric turbulence and longer timescale for optical defects. At each point of the sky around the target star, the level of scattered ligth can reach either very low or very high values, depending on phase fluctuations. However, at the location of a planetary companion, the brightness level van never falls under the object's intensity. Therefore, the

detection of a planet is in theory possible by finding the pixel(s) that never reach the obscuration level of the other pixels. A recent publication also studied the usefulness of statistical properties of speckles in AO images and their usefulness to discriminate between speckles and exoplanets (Gladysz et al., 2010).

2.2 Stellar coronagraphy

Pupil edges are responsible of diffraction effects as they correspond to an abrupt transition in flux between pupil's interior and exterior. This transition results in strong oscillations in the impulsive response, or PSF, of the telescope, which create the diffraction wings. As mentioned in section 1.3.2, the brightness ratio between a putative planet (let's say a *Jupiter*) to its star diffraction wings is around 10^{-6} for an 8m telescope at a wavelength of 3.8 μm. To reduce the stellar photon noise against which the planet must be distinguished, it is thus necessary to separate out the planet and stellar signals by resolved imaging, for which AO contributes. In addition, as shown in the last chapter, some residual aberrations remain even after the AO correction. These *quasi-static speckles*, which in the case of high-contrast imaging add themselves coherently and become dominant over signals that add incoherently, pollute the region close to the star preventing thereby the detection of putative circumstellar disks or low-mass planets. *Stellar coronagraphy* is used to mitigate the conjugated effects of these two phenomena. Note that from an instrumental point of view, the dynamic range of the best detectors is physically limited by their full-well capacity and the number of bits of the analog-to-digital converter. Therefore, not only new coronagraphic masks aid in reaching higher contrast, but the development of better and better detectors enable to get a wider dynamic range.

Coronagraphy was invented by Lyot (1930) with the initial goal of studying the Solar corona. It has recently been adapted to distant stars in the particular context of direct imaging of exoplanets. The basic principle of stellar coronagraphs consists in the combination of mask(s), and diaphragm(s) in focal and pupil planes, typically just before it arrives on the detector (i.e. after the beamsplitter in figure 2.1). A great diversity of combinations exist, so that we do not intend to be comprehensive as it is not the main topic of this work. Instead, we briefly review the most outstanding examples in each category of masks: amplitude mask, phase mask, hybrid (amplitude and phase) or interferometric coronagraphs. We refer the interested reader to (Mawet, Pueyo, et al., 2012) for a review of small angle coronagraphs.

2.2.1 Amplitude mask coronagraphs

Amplitude masks are characterized firstly by an opaque mask at the intermediate focus of the telescope, on top of the central core of the diffraction pattern of the star, and secondly, by a diaphragm of appropriate dimension in the relayed pupil plane, called *Lyot stop*, in order to block diffraction residuals. This configuration is basically the one proposed by Lyot to observe the Solar corona, and is therefore refered as classical Lyot coronagraph. The intensity at different locations of the lightpath is shown in figure 2.8.

In (a), the pupil plane has the shape of a disk truncated from both the spiders and secondary mirror. It is in first order uniformly illuminated. A faint companion is observed near the star in the

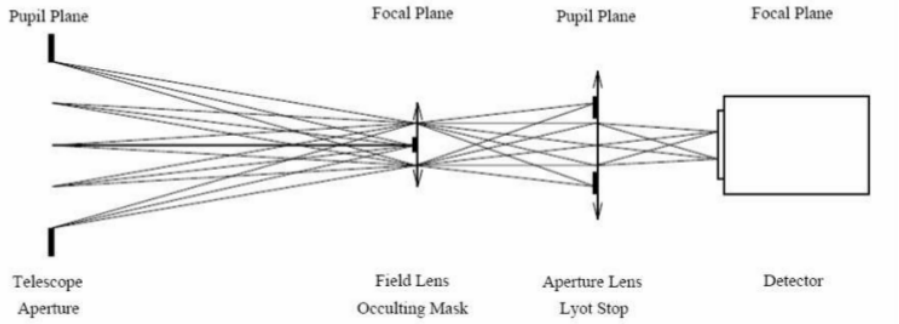

Figure 2.7: Principle of stellar coronagraphy. One or several masks and diaphragms are inserted either in the pupil or intermediate focal plane of the lightpath leading to the detector.

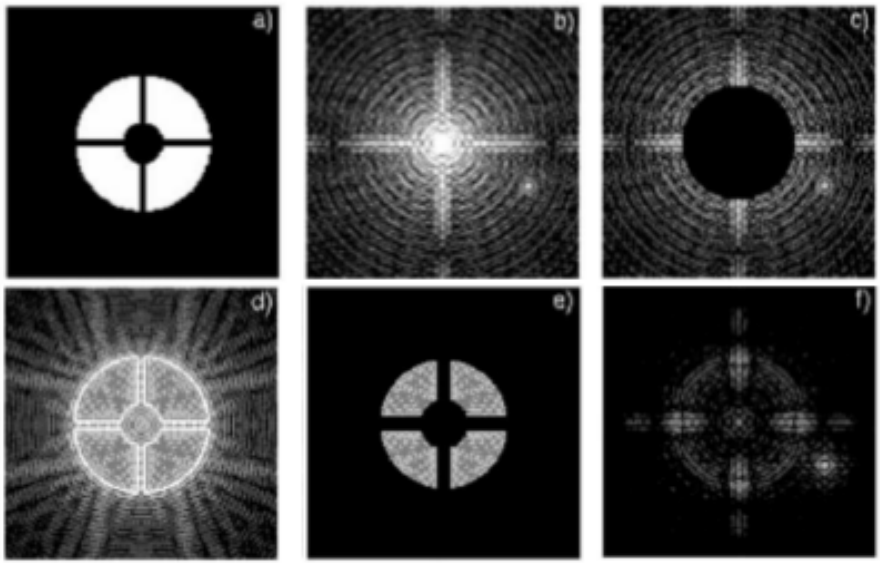

Figure 2.8: Intensity at different locations of the lightpath of a Lyot coronagraph. (a) Entrance pupil, (b) Focal plane before the mask, (c) Focal plane just after the mask, (d) Downstream pupil before Lyot stop, (e) after the Lyot stop and (f) in the final focal plane.

intermediate focal plane image (b), drown in the bright wings of the star, even if the star is occulted by the focal plane opaque mask (c). However, this mask has a double effect in the re-imaged pupil (d). First, the luminosity is decreased over the whole pupil and second brightness overloads are created on the edges of the pupil due to diffraction. This light corresponds in fact to starlight that has not been blocked and that was still present in the diffraction wings. The companion is not strongly affected by the presence of the focal mask. At this stage, the considerable step brought by Lyot was the addition of a diaphragm occulting the edges of the pupil (e). This required a thorough study of his instrument in order to apply an appropriate diaphragm enabling to conceal only the overload pattern. In the final focal plane (f) - i.e. on the detector, the stellar flux is globally reduced, whereas the flux of the companion will be more or less affected depending on the angular distance to the star.

The metric used to characterize the typical angular proximity (relative to the star) that can be reached by the coronagraph is the *inner working angle* (hereafter IWA). It is defined as the 50% off-axis throughput point of a coronagraphic system, whose value is usually expressed in terms of the resolution element (λ/D). In the case of amplitude mask coronagraphs, typical IWA ranges around 5-15 λ/D, it is thus inefficient very close to the star.

2.2.2 Phase mask coronagraphs

Recent researches on stellar coronagraphs focus largely on phase mask coronagraphs as they allow to reach much smaller working angles and to preserve the flux of the companion from amplitude loss (Mawet, Pueyo, et al., 2012). Instead of blocking the stellar image by an opaque mask, a phase plate is used to produce a phase shift. A large line of phase plates have been proposed, as the inspiration of each phase plate *designer* was taxed to correct the weaknesses of the previous generation. Depending on the model, some phase plates operate in the intermediate focal plane, whereas others lie in the pupil plane, either upstream and/or downstream.

The first one to be suggested was the plain circular phase plate (F. Roddier & Roddier, 1997), also known as the *nulling coronagraph* (Guyon et al., 1999). It produces in the intermediate focal plane a π radian phase shift to the core of the stellar image. Light diffracted outside the core is then almost perfectly eliminated by destructive interference in the downstream pupil plane, hence the name. This method would have allowed IWA very close to the diffraction limit.

However, another design has rapidly emerged as it allowed to solve partially the weaknesses of its predecessor, namely the chromatic effects of a π phase difference with a fixed radius phase plate[6]. The 4-quadrant phase mask (hereafter 4QPM), suggested by Rouan et al. (2000), introduces an azimuthal phase variation in four quadrants (respectively 0, π, 0 π rad), thereby solving the radial chromaticity issue. The simplicity of its design and the small IWA that it can reach (down to $\sim 1\lambda/D$) explains its relative success (installed at Palomar in H and Ks, in use on VLT/NaCo, planned for JWST/MIRI, VLT/VISIR, VLT/SPHERE).

Nevertheless, the discrete number of quadrants causes both some spatial information to be lost and the creation of artifacts. This concept was thus pushed further on to a smooth azimuthal modulation, the optical vortex coronagraph was born (Mawet et al., 2005). Its smoothness enables to correct the loss of spatial information of its predecessor. Current technology uses diamond work for its design.

[6]Indeed, a fixed radius phase plate does not yield same performances depending on wavelength, as the radius of the PSF evolves with λ/D.

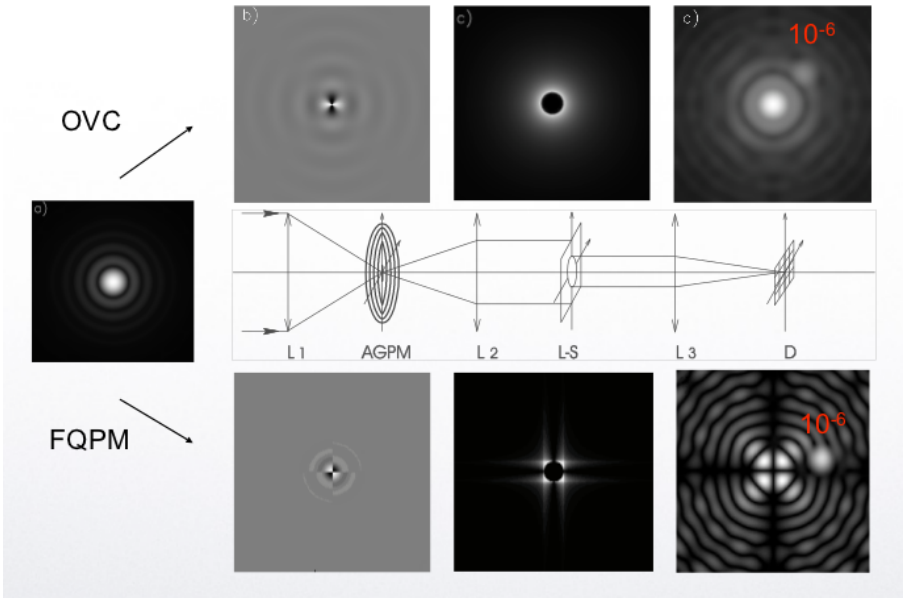

Figure 2.9: Intensity at different locations of the lightpath for the 4QPM and vortex coronagraphs: (a) at the focal plane before the mask, (b) the focal plane after the mask, (c) and (d) at the downstream pupil before Lyot stop (Rouan et al., 2000; Mawet et al., 2005).

Figure 2.9 shows the intensity at different locations of the lightpath for the 4QPM and optical vortex coronagraphs (hereafter OVC). The companion is hardly visible in the direct image (b), whereas it appears brighter in the coronagraphic image (d). With an angular separation of 330 mas (or 1.1 λ/D in the conditions of the observation), the discovery of a close companion to ϵ Cephei thanks to an OVC behind the 1.5 m WCS at Palomar constitutes, to date, the smallest angle detection ever realized with a coronagraph, in terms of λ/D (Mawet et al., 2010, 2011). As one can easily imagine, the impact on a larger telescope would be huge. Figure 2.11 shows the latest concerning optical vortex coronagraphs: the first test of the commissionning of VLT/VISIR's vector vortex coronagraph (AGPM), conveying relatively good performance.

2.2.3 Apodizers

In order to conceal the overload pattern as much possible and to reach small working angles, a diaphragm, smoothed following simple functions such as gaussian or cosines, or to more sophisticated ones such as prolate functions (Aime et al., 2002; Soummer et al., 2003), can be placed in the upstream (relative to the intermediate focal plane) pupil plane. These diaphragms are called *apodizers*. Thomas et al. (2011) showed that *apodized Lyot* coronagraphs could typically reach IWA of order 3-4 λ/D (which is though mediocre compared to capabilities of phase mask coronagraphs). However, they are fairly achromatic and insensitive to central obscuration and tip-tilt.

However, classical apodizers have the caveat of also reducing the flux of a putative companion. Phase-induced amplitude apodization (PIAA) coronagraphs have been introduced to compensate for

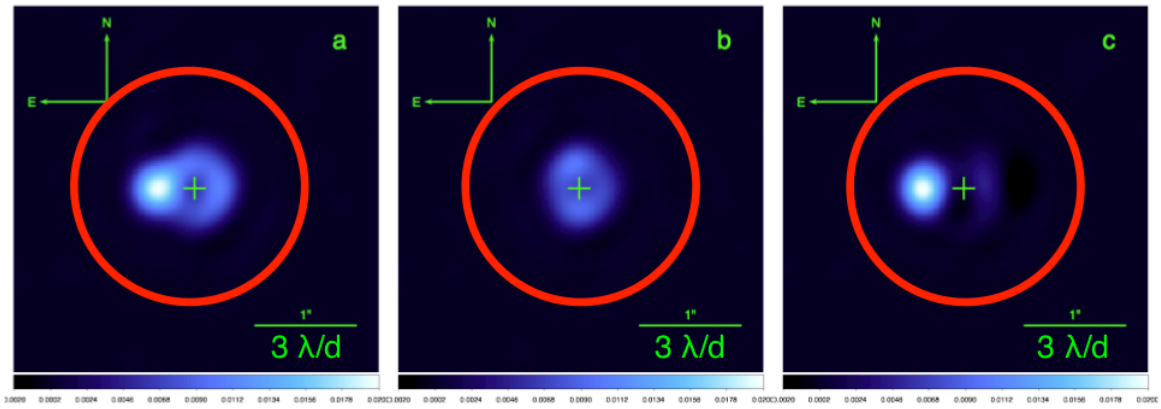

Figure 2.10: Image of ϵ Cephei and its close companion discovered using a vector vortex coronagraph behind the 1.5 m WCS at Palomar. a = target image, b = reference star, $c = ax \times b$. The candidate companion is 50 times fainter than ϵ Cephei, and lies at an angular separation of 330 mas, or 1.1 λ/D for the WCS. The red circle represents the $3\lambda/D$ IWA of typical new generation Lyot coronagraphs (e.g. the apodized Lyot coronagraph). This emphasizes the scientific importance of getting at smaller IWA than Lyot coronagraphs (Mawet et al., 2010, 2011).

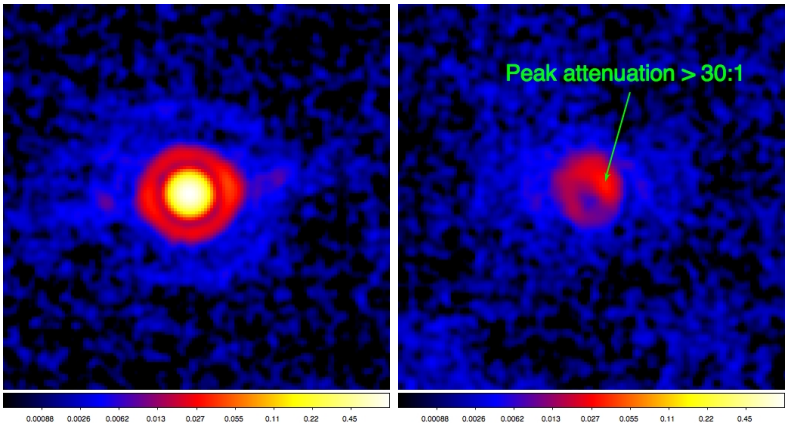

Figure 2.11: First commissionning test of VLT/VISIR's vector vortex coronagraph with the internal calibration source of VISIR. We notice that the artificial source is indeed *pumped out* by the vortex (D. Mawet, august 2012, private communication).

this weakness (Guyon, 2003; Guyon et al., 2005). Combined with classical Lyot coronagraphs, they present thus the double advantage of small IWA with no flux loss (Soummer, 2005). The apodizing phase plates (APP) of the MMT (Codona et al., 2006) and NaCo (Janson et al., 2010) are classified in this same category.

2.2.4 Hybrids

When both amplitude and phase masks are used within the same device, we talk about *hybrid coronagraph*. This kind of device combines advantages of both types of masks. They can reach small IWA, theoretically down to $1\lambda/D$ though a significant portion of the throughput would be lost, and they provide the best contrasts at larger angular distance (Trauger et al., 2011).

2.2.5 Interferometric coronagraphs

Finally, a last family of techniques consists in the splitting of the input beam, either by wavefront division or by amplitude division. The two paths are then interfered in a destructive fashion after one of them has undergone either field rotation or a passage through the focus. Devices using such mechanisms are refered as (achromatic) interferometric coronagraphs (Baudoz et al., 2000).

2.3 Observing strategies

In the highly-specialized field of direct imaging, all the different steps of an observation must be optimized to meet our goal, which is high contrast and high angular resolution. In particular, some observing strategies are more suitably designed than others. We present hereunder the main strategies in term of tracking and imaging methods, insisting on their suitable combinations.

2.3.1 Tracking

As Earth spins around its axis, the celestial sphere appears to rotate. During an astronomical observation, the telescope must therefore track the target across the sky. While for a long time telescopes were exclusively on an equatorial mounting, modern research facilities are now all equipped with an altazimuth mounting. For a same diameter, an equatorial mount would be indeed heavier, more expensive and require a larger dome structure. The advent of alt-az telescopes was enabled by the development of computers and hence more complex tracking and image-orienting algorithms.

Parallactic angle

The differences in orientation of a celestial object for the two telescope mounting types is illustrated in figure 2.12, at its dawn (left) and at its dusk (right), for an observer at a latitude of 50N. To point at a given star, an alt-az telescope is tilted vertically to match the target's *altitude* angle between the horizon and zenith, as well as rotated horizontally to match its *azimuth* angle measured along the horizon. Due to this construction, the telescope pupil always remains upright, oriented towards zenith. On the other hand, the observed piece of sky (or the field of view, hereafter FOV) is fixed to

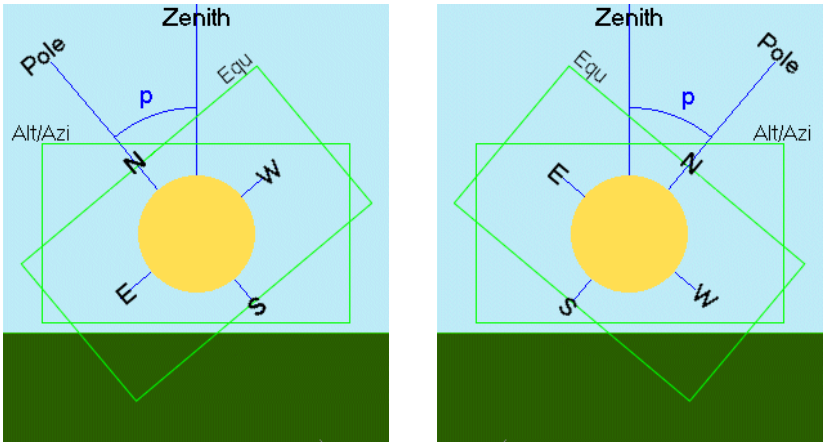

Figure 2.12: Illustration of the parallactic angle. Left: just after the rise of the object. Right: just before its set. We assume an observer located at a latitude of 50 N. The two rectangles show the FOV for an alt-az and equatorial telescope mounting.

celestial sphere, remaining oriented towards the celestial poles. For illustrative purposes, a rectangular FOV is chosen for the two mounting types.

With a telescope on an equatorial mounting, two points at the edges of the object (let's call them top and bottom) remain always on the curve (or *great circle*) that passes through the celestial pole during the object's motion. In other words, the cardinal points are always aligned with vertical and horizontal directions of the FOV. It is more delicate for an alt-az mounted telescope. In this case, the top and bottom points on the object's disk are on the curve that passes through the zenith. Now, the cardinal points of the disk slowly change between the object's rise and set. Only when the object is on the meridian are the cardinal points coincident with the top, bottom, left and right points of the object's disk. The angle p between these two different FOV is the same as the angle between the curve that passes through the middle of the object and the celestial pole, and the one passing through object center and zenith. This angle is known as the *parallactic angle* (p).

Mathematically, the parallactic angle p can be calculated from:

$$\sin(p) = \sin(A).\cos(\phi)/\cos(\delta) \tag{2.14}$$

where A is azimuth angle of the object, δ its declination and ϕ the latitude of the observer, or alternatively from:

$$\cos(p) = (\sin(\phi) - \sin(\delta).\sin(a))/(\cos(\delta).\cos(a)) \tag{2.15}$$

where a is the altitude of the object. The rotation rate $\dot{\psi}$ (degree/minute) of the FOV depends on p and therefore on the altitude of the target. It is obtained from the time derivative of equation (2.15):

$$\dot{\psi} = 0.2506\frac{\cos A \cos \phi}{\cos z} \tag{2.16}$$

usually expressed in terms of z, the distance to zenith (altitude a = 90-z) of the object. As an order of magnitude, the range of values for the parallactic angle of the Sun is between -42 and 42 at a latitude of 50. The whole variation between these extreme values is performed the day of the summer solstice.

	Observation strategies		
Orientation	Fixed instrument	Field-tracking	Pupil-tracking
Pupil	a	p	fixed
Field	$p + a$	fixed	$-p$

Table 2.1: Evolution of the orientation of the pupil and the FOV in the instrument plane as a function of the tracking strategy. The rotator can be either turned off (fixed instrument), a represents the altitude angle and p the parallactic angle.

Field tracking vs pupil tracking

Let's consider the specific case of an instrument mounted at the Nasmyth focus of the telescope, as it is the case of VLT/NaCo with which our data were acquired. If the instrument is decorrelated (or fixed compared) to the telescope, the recorded orientation of the telescope pupil will be evolving with the altitude a of the target. Similarly, the FOV is now seen by the instrument with a rotation not only due to the parallactic angle p (see previous paragraph) but also with the altitude a.

As most instruments mounted at the Nasmyth focus of modern research telescopes are equipped with a *rotator*[7], the observator has the choice between two possibilities of *tracking* for its target along the night. Either he opts for a fixed field or a fixed pupil. In the former case, we talk about *field-tracking* (hereafter FT), while the latter corresponds to *pupil-tracking* (hereafter PT) or, by reference to the imaging mode, angular differential imaging (hereafter ADI). In FT, the pupil rotation is given by the parallactic angle p (cf. its definition). On the contrary, if one decides to freeze the pupil, the relative rotation of the field is given by the opposite amount $(-p)$. Therefore, in view of equation (2.15), the rate at which the FOV rotates depends on the object coordinates. The field rotation is fastest when the target passes the highest point of its trajectory, i.e. when it transits the local meridian. The rate of field rotation around transit furthermore depends on the declination of the target. It is greatest for targets transiting close to zenith, i.e. whose declination is close to the geographic latitude of the telescope. Table 2.1 provides a summary of the respective evolution of the orientation of the pupil for a fixed instrument, field-tracking and pupil-tracking.

FT is the conventional way of tracking, as images taken during the night are stabilized and can be readily stacked to get better S/N ratios. However, PT has a strong advantage in the case of HC and HAR direct imaging curbed by bright quasi-static speckles, as speckles due to the telescope (spiders, telescope mirrors) and to the instrument are locked to each other. The resulting speckle halo around the target star remains as stable as possible. This is not the case for conventional FT, as speckles due to aberrations of the telescope and of the instrument rotate independently in the images. Therefore, recent data reduction algorithms in the scope of direct imaging of exoplanets (section 2.4), including LOCI, are essentially used with PT mode.

The use of PT with coronagraphy is particularly appropriate as they both reduce the stray light. However, at this stage, we should point out that the PT mode of VLT/NaCo has been plagued by a drift for about two years after the implementation of the PT mode, as this drift has directly affected

[7]However, the instrument is not necessarily mounted on the telescope though. If high stability of the instrument is endeavored, and in particular if the instrument is massive and would hence induce substantial mechanical flexures if rotated along with the telescope, it would also be *fixed* on a table. This is the case of upcoming instrument VLT/SPHERE.

our results. The guide star PSF, the supposed center of rotation, was describing a circle at the speed of the parallactic angle variation. The problem was eventually solved by october 2011, as it was noticed that the field selector, constituted of two parallel mirrors moving along to keep the star in the WFS, was incorrectly driven in the case of PT. In normal field tracking (FT), it has to update its position with respect to the azimuth angle, while this action should have been turned off for PT. This circular drift issue prevented an optimal use of any focal plane masks (i.e 4QPM and opaque Lyot coronagraphs). Unfortunately, the data reduced in this work were taken on March and November 2010, while this issue had not been fixed yet.

2.3.2 Differential imaging

As one needs to subtract the bright swarm of quasi-static speckles as best possible in order to achieve better detection limits, the idea of subtracting reference frames emerged very soon. A reference PSF image is any image whose subtraction from the target image would reduce the signal from the speckles while preserving that of the object sought after. A wide diversity of fashions have been proposed to subtract reference frames to the target image. The general point about them is that they have to be the most correlated to the target image and at the same time, present some diversity in order to preserve, or at least minimize the signal-loss of a putative companion, i.e. to decouple exoplanets from optical artifacts.

In this section, we briefly review a non-exhaustive list of the main techniques of differential imaging, namely reference star differential imaging (hereafter RDI), roll subtraction, spectral differential imaging (hereafter SDI), polarimetric differential imaging (hereafter PDI) and angular differential imaging (ADI). We devote a larger part to ADI, as it was the observing strategy chosen to obtain our data. The reduction algorithms associated to ADI are furthermore developed in the next section.

RDI

The basic method consists in subtracting a reference PSF obtained from the target star itself or from another star. Marois et al. (2005) showed that the subtraction with a reference PSF with a star close to the target achieves a factor ~ 4 of PSF noise attenuation, leaving nevertheless residuals that are also quasi-static and thus severely limiting detection of fainter companions. The efficiency of the subtraction depends on the level of correlation between reference PSF and target, which in turn depends largely on the time delay between both acquisitions, as quasi-static speckles although long lived, do still vary with time as explained in section 2.1.7. If the reference is another star, magnitude and color matching are also important so that the AO correction will be relatively similar for both the reference and the target, and the S/N ratio of the speckle pattern will also be approximately the same. Finally, parallactic angle matching should not neglected neither in order to mitigate differences spawned from mechanical flexures induced speckles. The main caveat of RDI is thus the small number of stars usually meeting all these conditions, so that the subtraction is often of average quality. However, in the case of coronagraphy at very small IWA, it is the most indicated method, as ADI and SDI-IFS are not applicable (Mawet, Pueyo, et al., 2012).

Roll subtraction

Both ground- and space-based imaging are plagued with the stellar PSF calibration problem caused by imperfect optics and slowly evolving optical alignments. However for space telescopes, the PSF stability is better. The subtraction of two stellar images acquired during the same orbit of the HST enabled to achieve a factor of order 50 (G. Schneider & Silverstone, 2003), this limit being ultimately dependent on the PSF evolution. This technique is known as *roll deconvolution* or *roll subtraction*. A recent example of successful use of this technique with the HST enabled to re-image the outstanding HR8799 system (Soummer et al., 2011).

DBI

The principle of spectral differential imaging by dual-beam imaging (SDI-DBI) relies on the simultaneous acquisition of 2 images, typically thanks to a beam splitter, in two different filters. One of them is supposedly centered on an absorption line, typically of CH_4 at 1.6 μm, and the other not. The two signals are then subtracted. The presence of a planetary companion would then provide non-null difference as any faint companion with the absorption feature is brighter in one filter than the other. Practical implementation of SDI-DBI is very simple and requires only a beam splitter, 2 filters and 2 detectors, so that most 8-m class telescopes acquired one (VLT/NaCo, Subaru/HiCIAO, Gemini/NICI).

A very similar concept was proposed by Kuhn et al. (2001) but with polarizers instead of filters. It assumes that light from the parent star is unpolarized and would become polarized through the atmosphere of the exoplanet. In this case, we talk about polarimetric differential imaging (PDI). This method relies on the simple fact that uncoherent and unpolarized light emitted from stars comes out polarized from the atmosphere of a planet, as it interacts with the molecules composing it. As asserted by Schmid et al. (2006), polarimetry being not limited by the stability of Earth's atmosphere, it would in principle be able to reach the high sensitivity needed for these detections (about one part in a million).

These techniques are supposed to work at very small IWA, so that they could be used in combination with phase mask coronagraphs. Nevertheless, although observed in substellar objects cooler than 1400 K (T dwarfs and smaller), the assumption that the off-axis signal presents molecular lines or degree of polarization significant enough to detected still needs to be verified. In addition, even As reference and target images are taken simultaneously at other wavelengths or polarizations, high correlations are achieved between both images. However, differential aberrations within the camera (that could also be called *NCPAs*) decorrelate the PSFs as a result of the beam splitting (Marois et al., 2005; Lenzen et al., 2004).

SDI-IFS

Integral field spectographs (hereafter IFS) obtain spectra in a two-dimensional field, so that they can be considered as the evolution of the long-slit spectrograph. By acquiring directly a spectrum in two dimensions instead of requiring several uses of a long-slit spectrograph, the exposure of the signal and background are made at the same time, which is essential when the noise that we are trying to subtract is varying. An IFS divides the image plane in spectral elements (*spaxels*), behind which lies a

prism (or any device enabling to disperse light) so that each *spaxel* is associated to a discrete spectrum of n different wavelengths. It is then possible to recover a datacube of n images, each of them at a different wavelength.

As the characteristic size of speckles is wavelength-dependent ($\sim \lambda/D$), this datacube of images displays a radial modulation of their size. On the contrary, a putative exoplanet would not vary in size with wavelength. The typical data reduction associated consists in re-scaling these different images, taking their median and subtracting it from each re-scaled image (in a very similar fashion to c-ADI, described in next section), and finally median-restack them in order to bring the exoplanet to light. An advantage of SDI-IFS is that, once a companion is detected, its spectral information is an immediate by-product. Examples of application of IFS to characterize companions with favorable contrast ratio include (McElwain et al., 2007; Patience et al., 2010).

ADI

ADI is the archetypal method exploiting PT. It was originally proposed by (Marois et al., 2006). As described in section 2.3.1, the principle is to use the differential rotation between FOV and pupil when the rotator is set to PT mode, to both retain speckles due tot he pupil and the instrument fixed, and obtain frames differentiated by angular diversity (by contrast e.g. with the radial diversity obtained with SDI-IFS). The evolution of this rotation is dictated by the parallactic angle p. ADI is an observing strategy and should not be confused with c-ADI, r-ADI or even p-ADI which are associated data reduction algorithms (described in section 2.4.

ADI has proved its efficiency with the imaging of exoplanets (e.g. Marois, Macintosh, et al., 2008; Marois et al., 2010; Lafrenière et al., 2010) and debris disks (e.g. Buenzli et al., 2010; Boccaletti et al., 2012; Currie et al., 2012). However, it is noteworthy that when extended objects such as disks are imaged, ADI do present some difficulties to build reference frames with a speckle pattern highly correlated to the target image but at the same time without encroachment with the flux of the disk. In this case, one faces the problem of *self-subtraction* (a concept that will as well be tackled in this version of LOCI, section 3.2). Not only does it lead to a lower signal-to-noise ratio (S/N) for the disk but it also biases the observable parameters of the disk (another concept that will be equally tackled for exoplanets later in this work). A qualitative and quantitative study of this problematic, leading to the conclusions that ADI can very easily create artificial features without involving astrophysical processes, as it induces fluw losses, can be found in (Milli et al., 2012).

Table 2.2 provides a summary of the main features of each differential imaging strategy.

2.4 Data reduction

Before announcing any discovery from the frames obtained at the end of the observation run, one needs to process images in order to suppress at best all the *systematics*. For a long time, this data reduction settled for what is usually refered as *basic treatment*, tackling systematics presented in section 2.4.1. More advanced processing methods arrived along with development of AO systems. However, it did not caused unanimous backing as for many domains in astronomy, interpretation from the basically reduced data was sufficient. In the field of HC and HAR imaging though, quasi-static speckles being

Strategy	Modulation	Noise
RDI	ON-OFF	$\propto T$, decorrelation due great time difference T
ADI	θ	$\propto t$, decorrelation also due to time delay, but t << T
SDI-IFS	r	$\propto \lambda$
SDI-DBI	λ_{CH_4}	$\propto \lambda$ and NCPAs (because of the beamsplitter)
PDI	P_{pl}	P_* (stars are never completely unpolarized), P_{instru} and NCPAs

Table 2.2: Characteristics of main differential imaging strategies. The second column provides the parameter that is modulated by the method ans the third column corresponds to the source of noise on which depends the decorrelation.

the main limitation of the direct detection of exoplanets, more and more sophisticated algorithms are constantly developed to deal with them. Without these appropriate processing algorithms, no detection can be made. These algorithms are generally very specific to each observing strategy in order to exploit as much as possible all the information provided by the specific signal modulation. In this section, we first present the basic treatment steps before focusing on ADI-type reduction methods, and in particular on LOCI and its damped version. Most of the methods described in this section were already implemented in IDL language by Dimitri at Palomar observatory and adapted to NaCo data, so that these algorithms constitute the starting point of the further personal implementation presented in the next chapter.

2.4.1 Basic treatment

The main steps of basic treatment are background (*dark* in VIS and *sky* in IR) subtraction, flat-field division, bad pixel map correction and cosmic rays rejection, in this order. Hereunder, we divide them following the type of bias they correct, namely additive, multiplicative and discrete biases.

Additive biases

In visible wavelengths, typical sources of noise patterns in the whole image is due to *bias level* and *dark current*. The bias level is the image obtained with no exposure time, thus only containing noise due to the electronics that elaborate the data obtained by the sensor. On the contrary, the dark current is the relatively small current due to charge accumulation within the detector itself, even when no photons are entering it. For each of these effects, there is a fixed number of counts erroneously added to pixels, independent of the exposure time for the bias level but exposure time-dependent for the dark current, independent of the number of counts in the sky or sources. These effects have to be corrected by the acquisition of *dark* frames, which as their name indicates, are images captured in a dark region of the sky. The average of these dark frames can then be subtracted from subsequent images to correct for the noise pattern caused by bias level and dark current.

In IR and NIR wavelengths, these effects are even worse because of the IR sensor. In addition, the atmosphere thermal emission has to be corrected. The acquisition of frames on the *sky* is thus performed, so that both bias level, dark current and atmosphere thermal emission are taken into account. For the longer-wavelength K, Ks and L images, we subtract a blank-sky image to remove thermal backgrounds.

Since dark current and thermal background evolve during the night, the rate of dark/sky acquisition is very high. Typically 2 darks/skies are taken after each set of 8 frames at VLT/NaCo, in order to provide the most appropriate dark/sky subtraction to all the images. Each dark/sky acquisition requires offset of the telescope.

Multiplicative biases

The different pixels of a given CCD show quantum efficiency (i.e. sensitivity) differences at different scales. Pixel-to-pixel variations are usually small (less than a few percent), but the large-scale variations can be larger. Moreover, any bits and pieces of stuff near the focal plane do also create regions of low quantum efficiency on the CCD. The point of flat-fielding is to correct these variations. A flat-field consists of the image of a uniform background of light that both matches the color of the dark background sky and illuminates the CCD in the same way as the background sky.

Flat fielding usually refers to the process of compensating both for the additive biases (dark current, bias level, thermal background) and multiplicative biases (the different gains due to QE discrepancies) of a detector. This operation can be written:

$$I_{red,1} = \frac{I_{raw} - dark/sky}{FF} \tag{2.17}$$

where I_{raw} is the raw image, and FF stands for flat-field. Once a detector has been appropriately flat-fielded, a uniform signal will create a uniform image (hence *flat-field*). Any further signal detected will not be caused to a systematic error.

Discrete biases

Detectors are never perfect. They present *dead* pixels, never showing light, *stuck* pixels, always showing light, and *hot pixels*, which have higher than normal dark current and resulting in brighter pixels especially on long-exposure acquisitions. A bad pixel map has thus to be applied on the image. It can be written:

$$I_{red,2} = bpixfix(I_{red,1}, bpixmap) \tag{2.18}$$

with $bpixfix$ the function using the bad pixels given in $bpixmap$ to correct the image $I_{red,1}$.

Finally, cosmic rays do also affect the detector. As cosmic rays reaching a sensor manifest themselves by one to four very bright pixels each, they can be dealt with specific filtering. Typically, one chooses a box size of 4 pixels, if their intensity is superior to 5 σ (σ being the noise level) they are removed:

$$I_{red,3} = sigma\_filter(I_{red,2}, box\_size = 4, threshold = 5) \tag{2.19}$$

where the threshold is expressed in terms of σ unit.

2.4.2 Pre-ADI procedures

When frames are taken in PT mode, several operations are achieved. As mentioned in section 2.3.1, the PT mode of NaCo was plagued by drifts of the center of rotation until November 2011, so that all images are not centered in the same way. A recentering of the images can be necessary. In this case,

it can be readily done by a search for a maximum (the centroid) within a box centred on the image and appropriate shift of the whole image. In our whole-in-one code, this option is possible with the keyword *centering*.

Depending on which object we are looking for, exoplanet or circumstellar disk, a spatial filter should be used or not. As mentioned in section 2.1.7, atmospheric turbulence is not completely corrected by the AO system, so that some atmospheric speckles taking the shape of smooth halos remain. The solution to erase these smooth and extended variations is the use of high-pass spatial frequency filter. Typically, we used a cutoff frequency of 4 FWHM (our observations being taken in L'-band, the FWHM was $\sim \lambda/D = 3.8\ 10^{-6}/8 \simeq 0.1''$). However, this high-pass filter should not be used if one wants to detect circumstellar disks, as they would, similarly to the atmospheric speckles, be substantially extincted. In our code, this distinction was taken into account and different keywords are used if one wants to run ADI or LOCI with or without applying this high pass filter: ADI_s and LOCI_s for simple ADI or LOCI, and ADI_f and LOCI_f for ADI and LOCI with images that have been high-pass filtered.

At the same time of these pre-processing procedures, the evolution of the parallactic angle of each frame is also recorded, as it will be used by the ADI algorithm.

2.4.3 ADI based data reduction algorithms

Before describing the possible ways of ADI-data reduction, we stress on the fact that ADI is an observing strategy, not a post-processing method. Data obtained in PT mode can indeed be reduced by different algorithms including classical ADI (c-ADI), s-ADI ((Lagrange et al., 2012)) and radial ADI (r-ADI). As for pseudo-ADI (p-ADI), it is to be used with frames obtained in conventional FT. As the field has not rotated in that case (some configurations are not compatible with PT, e.g. P1640), this post-processing technique make it artificially, by applying a global rotation to the images. As we focus on PT, we will not detail further this last option. Developments concerning c-ADI and r-ADI can be largely found in (Marois et al., 2006). Details about LOCI and damped-LOCI are to be found in (Lafrenière, Marois, et al., 2007) and (Pueyo et al., 2012) respectively.

c-ADI

Classical ADI is the easiest version of the ADI-data reduction process proposed by Marois et al. (2006). The principle of this method is shown in figure 2.13. The red dot symbolizes a planetary companion. As the images are taken in PT mode, it is rotating in the field by an amount given by the parallactic angle p. In first place, the median of the datacube of images (A_i) is computed (B). By definition, the median does not retain the companion, but contain all structures that are consistent throughout the observation. This median is our reference frame and is thus subsequently subtracted from each individual image reducing considerably the quasi-static speckle noise. Each frame of this new datacube $C_i = A_i - B$ contain the planet and the non-static part of the quasi-static speckle pattern. Finally, after putting the frames in a larger blank image, they can be derotated, knowing the parallactic angle of each frame, to form a new datacube $D_i = derot(C_i)$. Median-combining these images provides the final circular image, in which both the companion has added up and the remaining spurious background structures are further averaged down, so that the PSF noise is reduced in two steps.

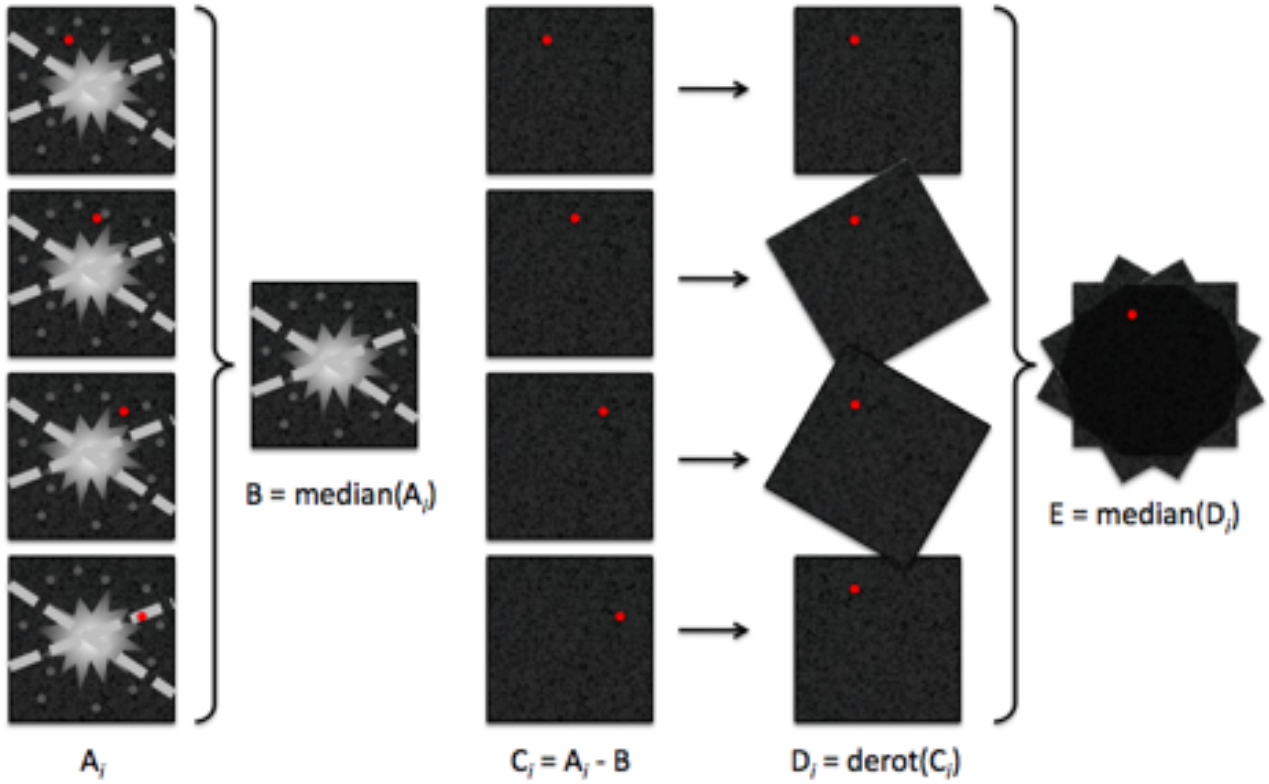

Figure 2.13: Principle of the c-ADI algorithm. (credit: Thalmann)

In practice, the method cannot remove totally the star's speckle halo because it is *quasi-static*, i.e. not entirely static. The key factor to subtract at best these speckles is the degree of correlation between the different frames, which depends notably on the stability of the atmosphere. Therefore a good and stable seeing is not only important for the AO system to correct the turbulence, but also on the quality of the quasi-static speckles subtraction and hence the detection limit for a given integration time. On the contrary, as a large number of images is taken, the pixel-to-pixel noise (i.e. PSF, flat field, dark and sky Poisson noises and detector readout noise) of the reference image is much less than that of any individual image. Therefore, c-ADI minimizes the noise in regions where the residuals are limited by pixel-to-pixel noise, but would not be the most suited solution in speckles dominated regions.

Another important point is the amount of field rotation. Indeed, if not enough field rotation occurs during the sequence of frames, then a putative companion will not be rejected by the median but retained in it. Therefore, the subtraction of such a reference frame would largely destruct the signal of the exoplanet, if any.

r-ADI

It appears from the process that we have just described that the key factors to reach the best detection limits in regions dominated by speckles are the correlation between the targets used for the reference frame and the necessity to have enough field rotation in order to not suppress the signal of a putative companion with the median. Therefore, instead of taking the median of all of the available frames as the reference for each frame, one can follow a criterion based on the parallactic angle variation, the time delay or more generally on the degree of correlation in order to select the images that will be used to build the reference frame. Depending on the criterion, a diversity of variants can be found, including radial-ADI (also presented in Marois et al., 2006) on which we focus here after brief explanation of the intermediate s-ADI. In figure 2.13, all the steps other than the computation of B remain identical for s-ADI and r-ADI.

In the case of *s-ADI* (Lagrange et al., 2010), for each of the n working frames, the reference frame associated is calculated from the mean of n_r images (typically 5-30) selected upon a specific criterion: these n_r frames are those that are the closest in time (measured by their hour angle), but for which the field has rotated of at least a separation x_p at a given radial distance r. The value of x_p is usually chosen so that it represents $\sim$ 2 to 5 FWHM at this radial distance, as in this case a putative companion would indeed be rejected by the median. In this context, the total amount of parallactic angle is fundamental as it governs the minimum *radial* separation r_{min} at which a separation x_p can be found for n_r images.

Alternatively, this fixed minimum separation x_p implies that it is more appropriate to build the reference PSF in annuli. Indeed, the n_r frames that are the closest in time and enabling a separation x_p are not the same at different radial distances. In *r-ADI*, the construction of each annulus of each reference PSF is thus given by the annulus of the median of the n_r frames that meet the criterion.

The total amount of field rotation available typically ranges between 20 to 80 for observations of one to several hours, depending on the altitude of the object. Parameter n_r must be chosen wisely in regard with the total number of frames, and must take into account the facts that a greater n_r induces better pixel-to-pixel noise subtraction, but less correlation between the chosen frames. Finally, time exposure t_exp is also decisive as it both directly governs the degree of correlation between n_r images

and sets the degree of speckle noise domination (compared e.g. to pixel-to-pixel noise) in the image.

A consequence of r-ADI is that targets closest to the zenith are more favourable than others in order to subtract at best the quasi-static speckles. Indeed, as seen in section 2.3.1, the rotation rate $\dot{\psi}$ (degree/minute) of the FOV depends on p and therefore on the altitude of the target. For a target *high* in the sky, the minimum delay τ_{min} to obtain a given parallactic variation equivalent to a separation x_p is thus smaller. Therefore the quasi-static speckles have also less time to decorrelate, and the subtraction of the reference PSF, constructed with the closest frames in time for each annulus, will achieve better results.

The noise attenuation g_{sub} that can be achieved in each image by the subtraction of the respective reference frames depends on the radial separation r, the time interval τ between the image and its reference, and the exposure time t_{exp} of each individual frame. As for the noise attenuation g_{derot} achieved in the second step (the median-combining of the de-rotated images), it depends on the decorrelation between the n differential images, so that their median-combination will only add up the signal of a companion, not of the residual noise. The global attenuation g is thus given by :

$$g(r, \tau, t_{exp}, n) = g_{sub}(r, \tau, t_{exp})\ g_{derot}(n) \tag{2.20}$$

The exact values of $g_{sub}(r, \tau, t_{exp})$ and $g_{derot}(n)$ depend of course on the coherence time of the quasi-static speckles. In any cases, the S/N ratio in r-ADI theoretically increases with observing time, being only eventually limited by field rotation. This technique shows thus a strong advantage in comparison to classical observations, for which the gain is quickly limited by the bright quasi-static pattern.

Figure 2.14 shows that noise attenuations of 20 to up to 100 can be reached at the end of the process of r-ADI, depending on the brightness of the star and as a function of angular separation.

As the application of c- or r-ADI has proved to alter significantly disks, a variant using masks to limit the contamination of the reference frame by the disk, called *mcADI*, has recently been proposed (Milli et al., 2012).

2.4.4 LOCI

Classical LOCI

The Locally Optimized Combination of Images was introduced by (Lafrenière, Marois, et al., 2007). LOCI resembles somewhat r-ADI in the sense that both are building reference images from the other frames than the one it will be subtracted from. However as we will see, LOCI pushes the optimization of the reference frames one step further. Moreover, it can be adapted to data taken with other observing strategies relying on PSF subtraction such as roll subtraction, SDI (it was shown by Crepp et al., 2011 and further exploited by Pueyo et al., 2012), and RDI observations. However, for convenience, we restrict ourself to the description of LOCI applied to ADI data.

Several new contributions distinguish LOCI from r-ADI. First, while r-ADI builds its reference PSF annulus by annulus, LOCI calculates its composite reference in different segments of optimization $\mathcal{O}$ that are defined in each different annulus, with the number of segments depending on the radial distance of the annulus. Second, whereas r-ADI computes its reference PSF with the median of a certain number of frames meeting the criterion described in the previous paragraph, LOCI finds the optimal set of coefficients c_i to be applied to n_L other frames in a linear combination, so that it

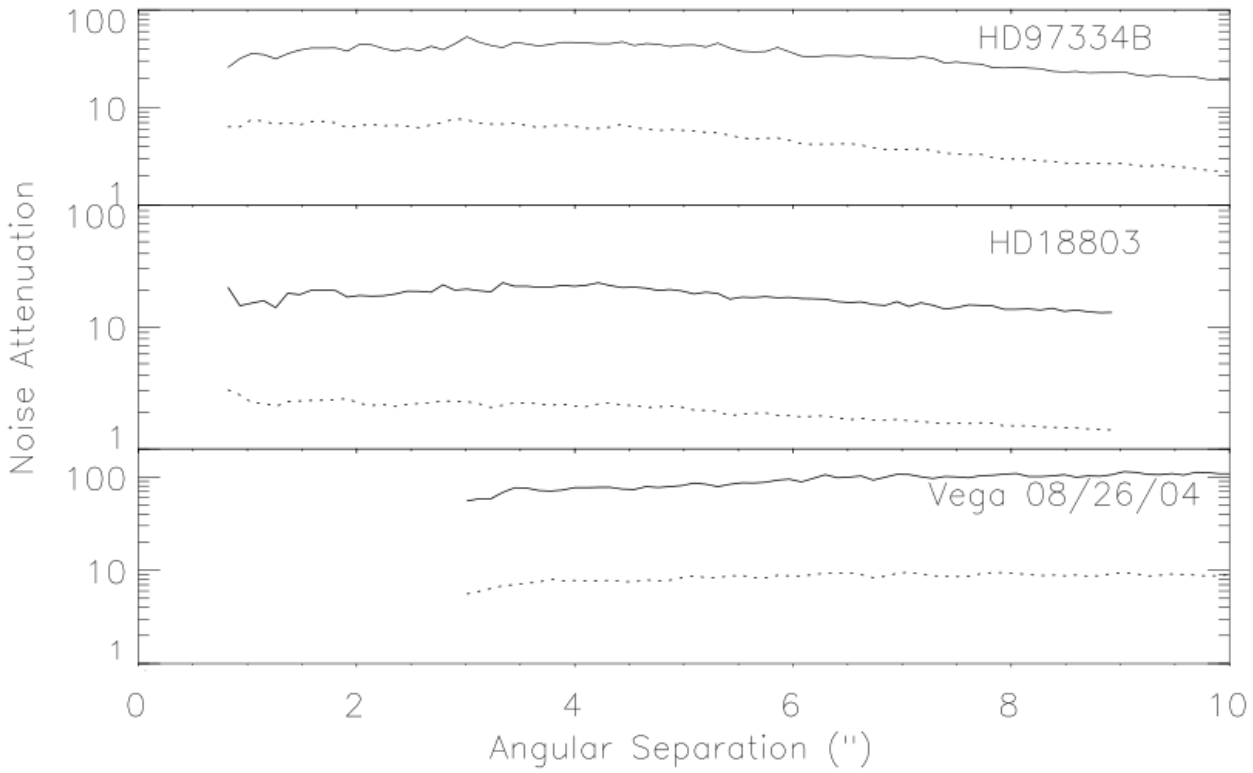

Figure 2.14: Contrast curves obtained for different stars. The dotted-lines correspond to the gains obtained from the single subtraction of the radially-computed reference frame, whereas solid lines show the result after the application of the whole process (Marois et al., 2006).

minimizes the least-squares residual between the target frame and the composite reference in the segment $\mathcal{O}$ (i.e. locally). Why locally? Because the correlation between target and reference PSF images generally varies with position within the target image. However, the subtraction is not performed in the segments $\mathcal{O}$ where the optimization is performed, but in the subtraction zones $\mathcal{S}$, which are much smaller subsections of segments $\mathcal{O}$ (figure 2.15).

It is important to note that similarly to r-ADI, a minimum separation (δ_{min}) criterion has to be applied if the reference images are target images acquired with ADI. The optimized PSF to be subtracted from a given subsection $\mathcal{S}$ of the target frame has indeed to be constructed in such a way that a putative companion that would lie in $\mathcal{S}$ would be delocated by at least a distance δ with respect to its putative initial position in the target frame. In this way, the source/planet signal is not there to be excluded. The value of our δ_{min} criterion is usually modulated by parameter N_δ entered by the user, with (Lafrenière, Marois, et al., 2007):

$$\delta_{min} = N_\delta \text{ FWHM } + \ r\mathrm{d}\phi_n \tag{2.21}$$

N_δ corresponds to the minimum displacement allowed, in terms of FWHM, if the reference frames were all static relative to each other. However, it is not the case in ADI. $\mathrm{d}\theta_n$ is the differential angle covered during exposure $\#n$ (it is given by $\dot{\psi}.t_{exp,n}$), and $r\mathrm{d}\theta_n$ is thus the azimuthal sprawl of a point source with separation r from the centre during this same exposure. Empirically, $N_\delta = 1$ is usually sufficient. However, in some cases, this criterion is too strong (in particular if the parallactic angle variation is very slow). Therefore, a loop of type: *while criterion=-1, do* $\delta_{min} = \delta_{min}/2$ is better in order to be sure to keep a number of reference frames $n_L(r) > 0$ in the pool, at the expense of augmenting the probability of erasing the signal of the companion though.

Why $\mathcal{O}$ and $\mathcal{S}$ zones and how are they chosen? Let's first consider the case of an $\mathcal{O}$ zone of the typical size of the FWHM of the PSF ($\sim \lambda/D$). If a point-like source such as a planet was to be there, the algorithm would not see the difference with a speckle and would therefore easily manage to subtract it from a combination of the other frames, as it is its role to minimize the residual between the subsections of the target frame and the composite reference. Therefore, a much larger optimization zone, not corresponding to the subtraction zone, has to be considered in order to *dilute* the influence of the planet in the speckles. However, as mentioned above, the correction still has to occur *locally* as the correlation varies spatially in the images, so that in the end this size has to be balanced. It is usually expressed in terms of number N_A of FWHM, as it is the relevant unit. The area A is given by:

$$A = N_A \pi \left(\frac{\text{FWHM}}{2} \right)^2 \tag{2.22}$$

The area of each optimization zone $\mathcal{O}$ is thus given by the surface covered by N_A PSF cores. N_A is a free parameter to be determined by the user, though typical values of range between 50 to 500. It is one of the parameters whose optimization was attempted in the implementation part of this work, as explained in section 3.3.

On the opposite, the size of the subtraction zones $\mathcal{S}$ should ideally be as small as possible in order to subtract the most appropriate quantities. Nonetheless, 1 pixel size $\mathcal{S}$ zones are not conceivable as they would require outrageous amount of time for processing. Accordingly, the size of the subtraction

zones has also to be balanced. Typical sizes are of order 10-100 pixels, this value being adapted from a machine to another.

These zones are further described by another parameter that can be chosen by the user: their aspect ratio g. From now on, we will assume polar symmetry as illustrated on figure 2.15, hence subsections $\mathcal{O}$ and $\mathcal{S}$ are (truncated) *camembert*-shaped. Therefore, while the value of A is set by N_A (equation (2.22)), the area of an optimization zone located at a radial separation r, with a radial width Δr and spanning an azimuthal angle $\Delta\phi$, is also given by:

$$A = \Delta r \left(r + \frac{\Delta r}{2} \right) \Delta\phi \tag{2.23}$$

The aspect ratio g is then defined as the ratio between the radial and azimuthal widths of $\mathcal{O}$:

$$g = \frac{r}{\left(r + \frac{\Delta r}{2} \right) \Delta\phi} \tag{2.24}$$

If g is set to 1, all the $\mathcal{O}$ zones have the shape of *pseudo-squares*, i.e. they have the same radial and azimuthal widths. If it set to a value inferior to 1, $\mathcal{O}$ zones are elongated along the azimuth (squashed radially). If $g > 1$, they are elongated radially, e.g. twice longer than wide if $g = 2$.

Although any geometry could be used in principle, we have chosen polar symmetry as it seemed the most natural. As a matter of fact, now that we have defined g, we can argue that it is indeed the most appropriate way to use LOCI for the detection of circumstellar disks. Indeed, setting g to 2 or more, and thus using radially elongated $\mathcal{O}$ zones enables to dilute at best the parts of the disks intersecting them.

Mathematical formalism If you have not understood the principle of LOCI yet, don't panic. Here comes the mathematical formalism, and it should help you to get it (!).

Calling $\mathcal{R}_i$ our datacube of reference images, we assume hereafter that $\mathcal{R}_i$ is only composed of target frames. The first step consists in finding the best combination $c_i\mathcal{R}_i$ to minimize the square of its subtraction from the target frame $\mathcal{T}$, in the optimization zone $\mathcal{O}$. A priori, we are thus looking for:

$$\min_{c_i} \sigma^2 = \min_{c_i} \left\{ \left[\mathcal{T} - \sum_i^{n_L} c_i \mathcal{R}_i \right]_{\mathcal{O}}^2 \right\} \tag{2.25}$$

One can re-write equation (2.25) with a more accurate formalism showing explicitly the 2 dimensions of the image and using a weighting function $w(x, y)$ we have, (Pueyo et al., 2012):

$$\min_{c_i} \left\{ \int_{\mathcal{O}} \mathrm{d}x\mathrm{d}y \; w(x,y) \left[T(x,y) - \sum_i^{n_L} c_i R_i(x,y) \right]^2 \right\} \tag{2.26}$$

The weighting function $w(x, y)$ can be used to mask certain pixels, either for bad pixel/cosmic rays correction if it has not been performed during the basic treatment, or more likely, it can be used in the search for circumstellar disk to mask annular regions around the star where the disk is supposed to lie, in order to limit the contamination of the reference frame by the disk (see e.g. mLOCI in Lagrange et al., 2012; Milli et al., 2012).

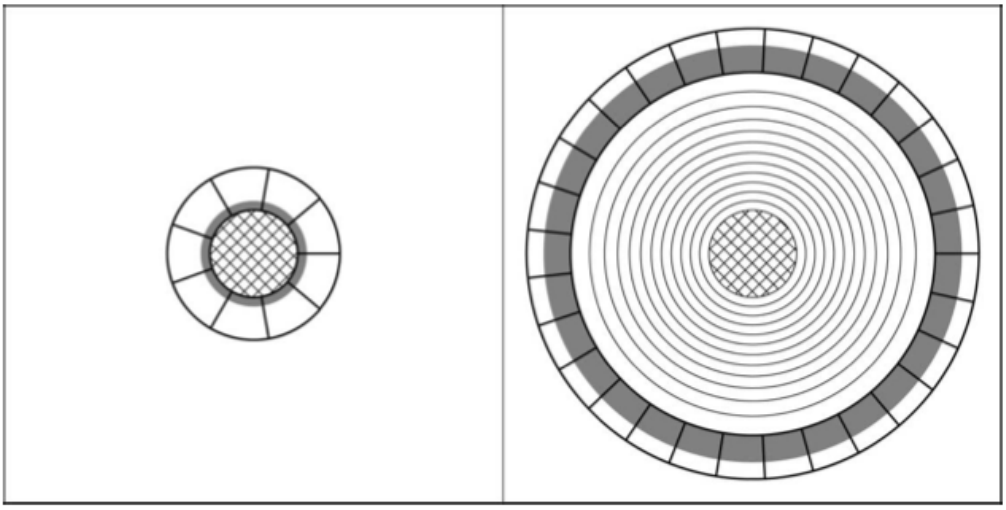

Figure 2.15: Optimization (delimited by thick lines) and subtraction (shaded in gray) zones defined by LOCI. The central circle (cross-hatched region) represents the saturated region. In principle, the shape of these zones can be chosen as wish, however the polar symmetry of the PSF suggests a similar division of the image. The left panel represents both the first subtraction and optimization regions within respectively the first subtraction and optimization annuli. Each subtraction region has a width dr, increasing radially outward in this example and associated to a larger optimization zone. The right panel shows the first 13 subtraction rings (the 13th being shaded) along with the 13th optimization annulus. (Lafrenière, Marois, et al., 2007).

As our bad pixels and cosmic rays are corrected in our basic treatment and furthermore our code will only be applied to search for exoplanets, we go back to equation (2.25) for simplicity. The minimum is obtained when all its partial derivatives with respect to the coefficients c_i are equal to zero. We have thus:

$$\frac{\partial \sigma^2}{\partial c_j} = -2\mathcal{R}_j \left(\mathcal{T} - \sum_i^{n_L} c_i \mathcal{R}_i \right) = 0 \quad \forall j = \{1, ..., n_L\} \tag{2.27}$$

Rearranging the different terms, it follows:

$$\sum_i^{n_L} c_i \mathcal{R}_j \mathcal{R}_i = \mathcal{R}_j \mathcal{T} \qquad \forall j = \{1, ..., n_L\} \tag{2.28}$$

We notice that equation (2.28) is actually a system of linear equation and can thus be written as $\mathbf{Ax} = \mathbf{b}$, with:

$$\mathbf{A_{ij}} = \mathcal{R}_i \mathcal{R}_j \;\; ; \;\; \mathbf{x_i} = c_i \;\; ; \;\; \mathbf{b_j} = \mathcal{R}_j \mathcal{T} \tag{2.29}$$

where $\mathbf{A_{ij}}$ is actually the autocorrelation matrix of the reference frames, $\mathbf{b_j}$ is the correlation vector between the target and the reference frames and $\mathbf{x_i}$ are the coefficients sought.

The determination of the coefficients is thus an inverse problem. Assuming $\mathbf{A_{ij}}$ is invertible, they are readily found with:

$$\mathbf{x} = \mathbf{A}^{-1}\mathbf{b} \tag{2.30}$$

Once the coefficients are found, the composite frame $\mathcal{R}_{comp}$ that should be subtracted to the working frame in the subtraction zone $\mathcal{S}$ of optimization zone $\mathcal{O}$ is given by:

$$\mathcal{R}_{comp} = \sum_i^{n_L} c_i \mathcal{R}_i \tag{2.31}$$

All the following steps are then exactly the same as for c-ADI. In the end, this procedure allows a better exploitation of the closely correlated speckle patterns in images taken shortly one after the other, and yields a greater contrast improvement than classic ADI. Lafrenière, Marois, et al. (2007) showed that a gain of about ~ 3 was achieved at small separations compared to r-ADI. This method has rapidly asserted itself in view of its good noise attenuation. Successful examples of application of LOCI include the 4 exoplanets discovered around HR8799 (Marois, Macintosh, et al., 2008; Marois et al., 2010) and the two faint and cold objects found around GJ 758 detected both at less than 2" of separation (Thalmann et al., 2009).

Damped LOCI

The advantage of LOCI is that it does not require any assumption to work, it will do its job for any set of images provided. This is for example not the case of methods based on a priori models of the PSF or the telescope (Mugnier et al., 2009; Burke & Devaney, 2010). On the other hand, in its classical version, LOCI presents the main caveat to not allow reliable spectro-photometry, hence science, to be made on any companion detected. Indeed, LOCI optimizes subtraction in the different subsections no matter what, so that both a certain amount of flux is lost and artificial features in the low resolution

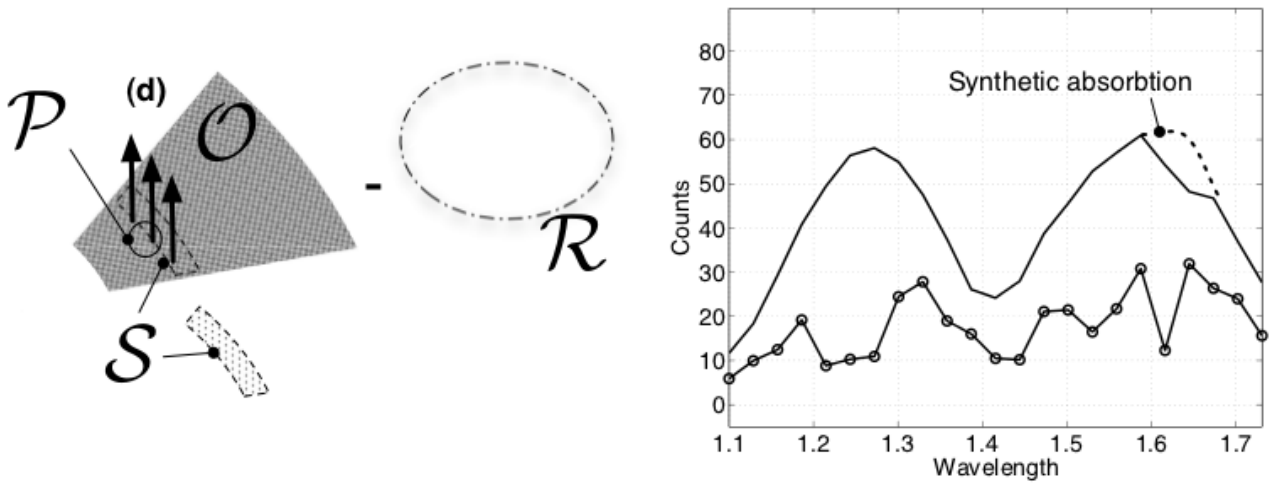

Figure 2.16: Principle of damped LOCI: minimization of the least square fit of the target frame in an optimization zone $\mathcal{O}$ (like classical LOCI), but at the same time maximization (upward arrows) of the spectrum after damped LOCI residual in the subtraction zone $\mathcal{S}$. The circle $\mathcal{P}$ corresponds to the pixels of the planet, however it is not considered in the cost function of this method. On the right: the spectrum of the star is in dotted line, it is similar to the one of the companion (overplotted, in solid line) except for a synthetic absorption at 1.65 μm. The extracted spectrum after LOCI is given in solid line with circles (measurements): the absorption feature is detected (Pueyo et al., 2012).

of the detected object can possibly be introduced. The recent use of LOCI on SDI-IFS data showed a loss of 60% of the companion flux that is constant over the spectral window (Bowler et al., 2010). However, a gray depletion is not necessarily the rule as simulations with injection of fake companions have indeed yielded non-gray response (Zimmerman et al., 2010). In this context, Pueyo et al. (2012) suggested two main upgrades to be applied to classical LOCI, the new version being known as *damped LOCI* (hereafter d-LOCI). As most of the formalism is identical to the one presented in the above paragraph, we keep the same notations.

Pueyo et al. (2012) first studied the spectro-photometric results obtained after application of LOCI, for several possibilities of relative dispositions of $\mathcal{S}$ and $\mathcal{O}$ zones, on a synthetic companion of a given spectrum. They found that only one possibility led to preservation of the spectral information of the companion (figure 2.16). This solution corresponds to the choice of minimizing the least square fit of the target frame in an optimization zone, but at the same time maximizing the spectrum after d-LOCI residual in the subtraction zone.

Therefore, in addition to equation (2.25), a further condition on the coefficients is added to the previous cost function. The new cost function can be expressed in simple mathematical formalism by:

$$\begin{cases} \min\limits_{c_i} \left[\mathcal{T} - \sum\limits_{i}^{n_L} c_i \mathcal{R}_i \right]_{\mathcal{O}}^2 \\ \\ \max\limits_{c_i} \left[\mathcal{T} - \sum\limits_{i}^{n_L} c_i \mathcal{R}_i \right]_{\mathcal{S}}^2 \end{cases} \tag{2.32}$$

In the previous paragraph, we did not insist on the inversion problem as we assumed $\mathbf{A}$ to be easily invertible. In practice, a deeper look is needed. Back to equation (2.30) in the case of data taken in ADI, the autocorrelation is the greatest between the same frames (i.e. the main diagonal is maximal). Out of the main diagonal, the correlation decreases at a rate depending on the level of correlation between successive frames. In the end, the $\mathbf{A}$ is in practice very close to the *identity* matrix, which leads to poor conditioning for its inversion. The use of specific algorithms for inverse problems such as *singular value decomposition* (hereafter SVD), *bound value least square* (hereafter BVLS) or *non-negative least square* (hereafter NNLS) is thus required. A description of these different specific algorithms is out of the topic of this work. However, we provide a short summary of their main features. SVD is the standard method, it provides the best noise attenuation, however it is less stable. NNLS forces the coefficients to be all positive, it preserves the flux but both the noise is less attenuated and the algorithm is slower. Finally, BVLS forces the coefficients to be between two values set by the user in order to avoid divergence. It is thus stabler than NNLS, and provides intermediate performances in terms of noise attenuation.

As NNLS is the only method that preserves the flux, it is the one that was chosen by Pueyo et al. (2012) in combination with its new cost function. In final, we can thus summarize d-LOCI as a differential imaging data reduction method whose composite references are the result of a trade-off between minimizing the fit residual in the zone $\mathcal{O}$ and maximizing it in the zone $\mathcal{S}$, under the constraint that all the composite coefficients are positive.

2.4.5 Alternatives to LOCI

While damped-LOCI seems the most appropriate and efficient way to reduce HC and HAR acquired images with SDI and ADI, it should be kept in mind that, as for any perfectible technique, new algorithms are being developed, in particular in the dynamic field which is direct imaging of low-mass companions. Very recently, a new promising technique, perhaps able to supplant LOCI and d-LOCI, has been proposed independently by two different teams, (Soummer, Pueyo, & Larkin, 2012) and (Amara & Quanz, 2012). Both suggest the use of *principal component analysis*. This technique is based on the projection of the science target on a basis of eigenimages spawned through a Karhunen-Loève transform applied to a set of reference PSFs. According to them, this approach provides comparable PSF-suppression to LOCI algorithm, though with increased robustness to the algorithm parameters and speed enhancement. Furthermore, this method does not bias astrometry and photometry of discovered faint sources.

Chapter 3

Personal implementation

First and foremost, though looking paradoxally, a summary of the whole final reduction pipeline that was implemented is given. The purpose is to give a global view of its different components, insisting on which parts of it were the fruits of the efforts undertaken during this work (i.e. what Dimitri had not implemented yet). The two main contributions which are the introduction of fake companions and the attempt of parameters optimization is subsequently the subject of more detailed developments in sections 3.2 and 3.3.

3.1 Global picture of the code

The call of the main procedure `pro reduce_naco_nirc2_v11` indicates some important features in the code (we recommend the reader to glance at the outline of the main program attached in appendix A, p.131). This code claims to be the most versatile possible as it can effectively perform basic treatment, c-ADI and a personalized version of LOCI (to be used with ADI data though). The name of the beast itself indicates that the code was not only built for data obtained with VLT/NaCo, but also for Keck/Nirc2[1]. It is to be noted that the personalized version of LOCI (hereafter p-LOCI) present in our all-in-one code encompasses in turn the classical algorithm c-LOCI described in section 2.4.4. As a matter of fact, the main feature of our p-LOCI is that it performs two iterations of c-LOCI, the second one being run with fake companions.

To further develop some aspects of the existing code, we took a leaf out of the works of Lafrenière, Marois, et al. (2007) and Pueyo et al. (2012), namely we injected some fake companions in order to measure the extinction due to LOCI (section 3.2), plotted contrast curves and endeavored an optimization of the LOCI parameters that have to be set by the user, first empirically and then algorithmically (section 3.3). Before presenting our contributions, we detail the input parameters that feed our code and remind the concept of contrast curve.

3.1.1 Input parameters

The input parameters required are the center of the star (c_x, c_y), starting and ending frames (`st_ob`, `nd_ob`) and desired level of the fake companions injection in terms of sigma (see section 3.2). All

[1] As a matter of fact, the kernel of the code was adapted from the Nirc2 version, to NaCo.

the others are keyword parameters. Depending on whether the data were obtained with NaCo or Nirc2, the user indicates the corresponding keyword. If the basic treatment and pre-ADI procedures, both described in sections 2.4.1 and 2.4.2, have not been performed yet, keyword `/basic` should be mentioned. Subsequently, the following keywords are the most important as they indicate which kind of data reduction method is wished to be used: `ADI_s` and `ADI_f` correspond respectively to simple and high-pass spatial filtered c-ADI algorithm, whereas `LOCI_s` and `LOCI_f` correspond to simple and high-pass filtered p-LOCI. In association, the keyword `contrast_curve` plots, as it indicates, contrast curves obtained after c-ADI or p-LOCI. It provides thus detection limits, as a function of radial separation to the star.

Keywords `mag_L`, `centering` and `concat` are specific to the case of NaCo. The L'-band magnitude `mag_L` is required for the photometric normalisation[2]. Centering keyword is optional, but recommended for data acquired with NaCo in PT before the PT drift issue was solved [3]. Concatenation `concat` is optional also, if used, it should be equal to a vector composed of the *good* frames of the datacube. In the case the user wishes to utilize the `concat` option (e.g. the user guesses from its log that some of his frames are not good and wishes to discard them), the code has to be run twice:

1. It is first run with the compulsory parameters (c_x, c_y, st$_o b$, nd$_o b$, sigma), keywords /Naco and mag_L (and optionally /centering) or /Nirc2, and keyword /basic. By a glance at the basic-treated datacube created, a vector containing the number of the *good* frames is then recorded (e.g. vec_concat).

2. The second run is subsequently performed with the compulsory parameters, keywords /Naco and mag_L or /Nirc2, keywords ADI_s or ADI_f and/or LOCI_s or LOCI_f, keyword /contrast_curve, and keyword concat=vec_concat.

3.1.2 Contrast curves

If the central star is seen, either in the middle of the image (i.e. not occulted by a Lyot mask for example) or on a reference dedicated frame, the determination of the central flux (in ADU) is immediate. The value of all the pixels in the image can subsequently be divided by this central flux to *normalize* the image. Normalizing enables both to plot contrast curves and to determine the relative luminosity of a companion readily. As regions close to the star are usually dominated by quasi-static speckles adding coherently with exposure time, contrast curves are the appropriate metric to measure their degree of attenuation by either c-ADI or p-LOCI.

In practice, to plot the contrast curve, one has to estimate the radial profile of the level $N(r)$ of the final image (typically the median of the LOCI frames). This can be done by defining a matrix $\mathbf{M}$ of n_ϕ (e.g. 360) x n_r (e.g. dim/2 = 200) components representing a polar-symmetric array of 360 points distributed azimuthally at each of the 200 values of radius across the median image. The

[2]It was usually estimated from the L-band magnitude given in the WISE catalog and the temperature of the star (if the latter has never been determined independently, it was assessed from the spectral type). Indeed, knowing both the magnitude in a close wavelength and its effective temperature set two points in the black body curve, the second point being the peak of the bell-shaped curve (through Wien's law). On-line algorithms, such as *NICMOS Units Conversion Form* which was extensively used, are based on this principle to enable a direct computation.

[3]As a matter of fact, we forgot to use it when applying our code to the targets presented in the next chapter, so that some effects could be the result of the PT drift.

discrete radial profile $N(r_j)$ is subsequently calculated with the standard deviation of the 360 values at each radius:

$$\sigma(N_j) = \text{stddev}(\mathbf{M_{ij}} \quad \forall i \in \{1, ...360\}) \tag{3.1}$$

The plot of the radial profile found constitutes the contrast curve. Nevertheless, the contrast curve is usually multiplied by a factor n (e.g. 5) in order to represent the detection limit. Indeed, assuming the residual noise is Gaussian, which has been shown to be the case after use of LOCI (Marois, Lafrenière, et al., 2008), the confidence level is given by

$$n{-}\sigma = \text{erf}\left(\frac{n}{\sqrt{2}}\right)$$

For n = 5, this confidence level is about $1 - 10^{-7}$. For n=3, it is ∼0.9973 and for n=1, only ∼0.68289 (Marois, Lafrenière, et al., 2008).

3.2 Fake companions

To obtain the best estimate of the photometry of a detected companion is very important for scientific purposes. It can indeed lead to an estimate of its mass, provided the age of the star and formation models. In turn, these formation models are constrained by statistically significant data gathered by the discovery of exoplanets.

As pointed out by Lafrenière, Marois, et al. (2007) and Pueyo et al. (2012), the flux of a putative companion is reduced by LOCI. In order to perform correct photometry on an exoplanet found, it is thus necessary to know with which factor α it has been lowered. For this purpose, fake companions are injected at different positions, both with a radial and azimuthal diversity, in the image. These fake companions are actually PSFs of star acquired at high Sr ratio, either with VLT/NaCo or Keck/Nirc2. Depending on the instrument (NaCo or Nirc2) and on the filter in which the images were taken, the fake companions to be injected are correspondingly chosen among a library of PSFs.

3.2.1 Pattern

Figure 3.1 shows the pattern chosen for the injection: $n_{rad} = 4$ companions are stretched radially on each of the $n_{br} = 6$ different branches. Variants including spiral patterns could also have been used.

The determination of their exact position is a bit more tricky than it looks, and should be done very generally for n_{rad} and n_{br}. A point that should be kept in mind is that fake companions should span at best the whole extent, both radial and azimuthal, of the LOCI image, in order to have the best estimate of the evolution of the attenuation factor in the image.

Firstly, we focus on the radial separations from the centre at which they should be placed. The first companion injected (counting radially outward) has thus to be placed at the shortest angular distance $r_{c,1}$ (expressed in pixels) from the centre, with at the same time $r_{c,1}$ great enough so that the injected PSF does not leak in the inner edge radius $r_{LOCI,in}$ (expressed in number of resolution elements FWHM) at which LOCI starts its computation[4]. To meet this condition, we take thus

[4]Indeed, LOCI does not start from the centre of the image, as it is of no use to apply it on a saturated zone. Similarly, if a Lyot mask is placed in the optical path (it is the case of the data reduced in chapter 4, it is of no use neither to apply

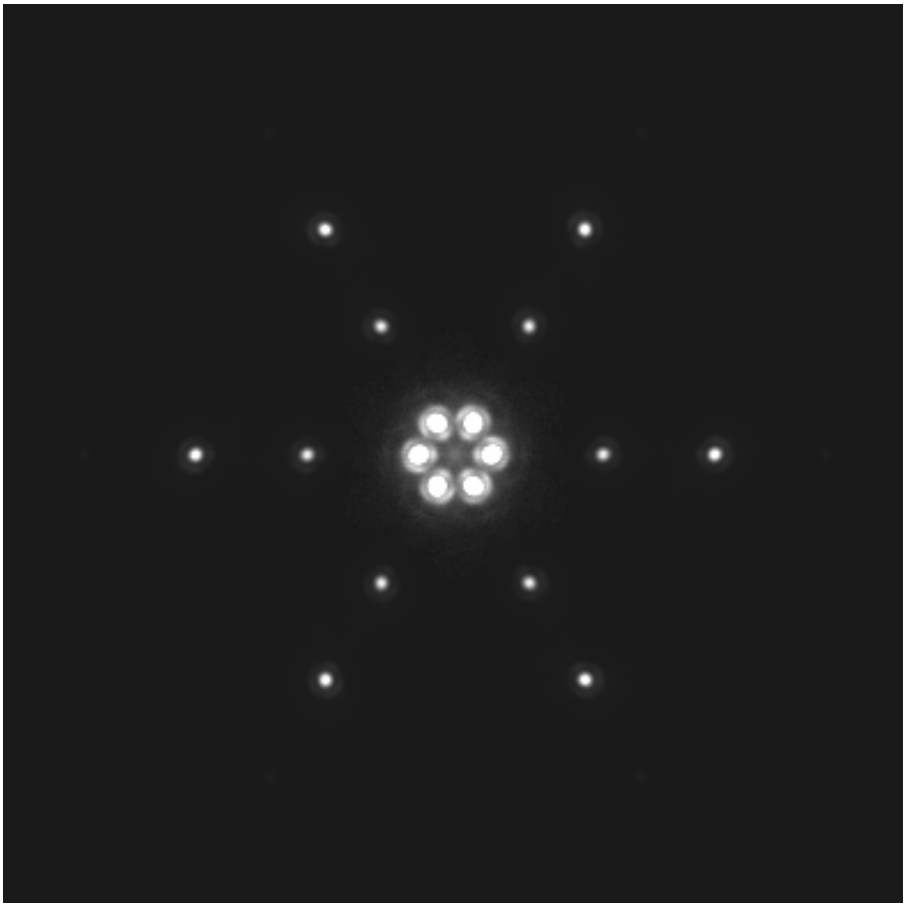

Figure 3.1: Pattern of fake companions injected. 4 fake companions equally spaced radially are introduced at each of the 6 different azimuths. Their respective level is governed by the local noise. In this case, they were injected around HIP73633. Brightness scale is linear. We notice that the last row of fake companions is hardly detectable, as the noise there is much weaker than closer to the star.

typically:

$$r_{c,1} = (r_{LOCI,in} + 1) * \text{FWHM} * \text{plsc} \tag{3.2}$$

where plsc is the plate scale at which the image was taken (e.g. 0.027 mas/px for L27 plate).

Second, the last companion to be injected must not leak outside the LOCI image neither. Combining equations (2.23) and (2.24) provides the radial extent Δr (in terms of FWHM) of LOCI's optimization zones $\mathcal{O}$ in function of its specific parameters chosen by the user (N_A and g):

$$\Delta r = \sqrt{\frac{\pi g N_A (\text{FWHM})^2}{4}} \tag{3.3}$$

For safety (fake companions images are square, and the edge of LOCI image is round), we choose to inject the last companion at:

$$r_{c,n_{rad}} = (\text{dim}/2) * \text{plsc} - 1.1 * \Delta r * \text{plsc} \tag{3.4}$$

where dim is the dimension of the LOCI image (typically set to 400 px).

The $n_{rad} - 2$ fake companions left should be placed at equal intermediate distances, so that we have the general rule:

$$r_{c,i} = r_{c,1} + \sum_{i=1}^{n_{rad}} (i-1) * \frac{r_{c,n_{rad}} - r_{c,1}}{n_{rad} - 1} \tag{3.5}$$

Now that we have determined one branch of the snowflake pattern, all what is left to do is to rotate n_{br} times, each time by an angle $\Delta\phi = 360/n_{br}$, with respect to the centre of the star. In other words, we have determined the polar coordinates of the different locations where the fake companions have to be injected. In the end, the change of coordinates can be readily done in IDL language and we find the set of positions $x_{i,j}, y_{i,j}$ $(i = 1, ..., n_{rad}; j = 1, ..., n_{br})$ of the fake companions in terms of pixels in the image.

3.2.2 Injection

At this stage, we need to know at which level the fake companions should be entered. This level is modulated by parameter `sigma` in the call of the main program. All our LOCI-reductions were performed with a standard value of `sigma` = 5, which means that the fake companions are inserted at a level of 5 times the noise level $\sigma(r)$. But from which frame should this noise level be taken? It appears that the relevant noise level to choose is the one of the median of the LOCI frames obtained after the first pass, as the noise attenuation will also eventually be computed from the median of the LOCI frames, but of the second pass.

To estimate the radial profile $\sigma(r)$ from the median of the LOCI frames, the process described in section 3.1.2 is followed. The discrete radial profile $\sigma(r_j)$ is also given by the standard deviation of azimuthal values of the polar-symmetric array at a given radius r ((3.1)).

Once this radial profile determined, the injection of the fake companions at a 5-$\sigma(r)$ level in all images of the datacube can eventually be performed. At this step, it should not be forgotten that ADI

it in the mask. In our case, we fixed a value of 3 FWHM for $r_{LOCI,in}$, which means it is placed on the third resolution element starting from the centre.

data are acquired with a rotation of the field. In order to be consistent, the pattern of fake companions has to be rotated of an amount given by the parallactic angle p, before being effectively injected in each frame. At this stage, we can run LOCI on our datacube of images where the companions have been injected for a second pass (cf. *LOCI second pass* in the outline of the whole code, page 133).

3.2.3 Attenuation factor

The attenuation factor $\alpha(r_i, \theta_j)$ is first calculated for each fake companion. It is the ratio between the residual intensity of the fake companion $I_{aft.\ LOCI}$ integrated over its FWHM , after LOCI, and its initial intensity ($I_{bef.\ LOCI} = 5\ \sigma$) integrated over its FWHM:

$$\alpha(r_i, \theta_j) = \frac{\int_{\text{FWHM}} I_{aft.\ LOCI}(r_i, \theta_j)}{\int_{\text{FWHM}} I_{bef.\ LOCI}(r_i, \theta_j)} \quad \forall i \in \{1, ..., n_r\}; \forall j \in \{1, ..., n_{br}\} \tag{3.6}$$

Once this factor is known for each fake companion, it is averaged azimuthally:

$$\alpha(r_i) = \frac{1}{n_{br}} \sum_{j=1}^{n_{br}} \alpha(r_i, \theta_j) \quad \forall i \in \{1, ..., n_r\} \tag{3.7}$$

As we know the azimuthal average of α for each of the n_{rad} different radii, it is possible to interpolate (if $n_{rad} \geq 4$) a function $\alpha(r)$ thanks to the IDL function `interpol` and its optional parameter `/spline`, so that we have a quasi-continuous estimate of the attenuation over the whole radial extent. Generally, $\alpha(r)$ would be much greater in the central part of the image. Note that once this attenuation profile is known, a map representing this attenuation in 2D can be reconstructed (figure 3.2).

3.2.4 True contrast curves

At the end of the first pass of LOCI, a contrast curve is computed following the process described in section 3.1.2. However, as mentioned numerous times, LOCI biases the throughput, so that the contrast curve plotted at the end of the first pass does not represent our true detection limit. Indeed, if a companion is present in the working images, let's say at a level 5-σ (with σ the level of the median of their LOCI images), it can for example be reduced to a final level 3-σ at the end of the process by c-LOCI. The determination of this attenuation factor constitutes the precise purpose of the introduction of our fake companions.

Now that we have determined the radial attenuation profile, the true detection limit is finally given by:

$$S(r) = \frac{5N(r)}{\alpha(r)} \tag{3.8}$$

Contrast curves presented in the next chapter show both curves, the non-attenuated one resulting from the first pass, and the second corrected from the attenuation.

It is interesting to note that the concept of fake companion has been recently extrapolated to create fake disks, enabling to study the bias introduced in them by several reduction algorithms such as c-ADI, r-ADI or c-LOCI (Milli et al., 2012).

Figure 3.2: Example of a reconstructed attenuation map, after p-LOCI applied to HD 59967. The brightness scale is linear. While inner parts of the disk show attenuation close to ~ 1, in outer parts it is of order ~ 0.01

3.3 Optimization of the parameters

In their article describing the concept of LOCI, Lafrenière, Marois, et al. (2007) searched empirically the values of N_A , g, dr and N_δ that were maximizing the sensitivity of their algorithm to faint point sources. As pointed out in their manuscript, the optimal parameter values may vary slightly for other sets of data depending on the telescope, instrument, seeing, FOV rotation rate, target brightness, etc. In consequence, we decided to test both empirically, with slightly different parameters, and algorithmically, i.e. with a dedicated algorithm, called AMOEBA, searching for the values of a set of parameters that minimizes or maximizes a certain *figure of merit*.

3.3.1 Relevant parameters

In order to set things clear, we first briefly remind the different relevant parameters of LOCI.

N_A sets the size of all our optimization zones $\mathcal{O}$. This parameter is the number of resolution elements (or *cores* of PSF) fitting in each $\mathcal{O}$-zone. Its optimal value must be the balance, as a small value favors better speckle attenuation (it is easier for the linear combination to create a highly-correlated signal) but greater value enables a greater dilution of the presence of a companion, which is hence less attenuated.

g sets the geometry of the optimization zones. This parameter is defined as the ratio between the radial and azimuthal widths (equation (2.24)). $g < 1$, $g = 1$ and $g > 1$ correspond respectively to radially squashed, pseudo-squared and radially elongated shapes. A priori, no assumption can be made about its optimal value, which probably varies from case to case (except for thin disk, where a $g > 1$ seems more appropriate to minimize its extinction).

N_δ (in terms of FWHM) modulates the minimum displacement δ_{min} of a putative point source in the actual $\mathcal{O}$ of the reference images compared to its position in the $\mathcal{O}$ region of the target image (as frames rotate for ADI data). This criterion governs the number of frames rejected from the computation. δ_{min} being dependent on the radial separation r (cf. equation (2.21)), N_δ has little impact at great angular separation. On the contrary, the value of N_δ is critical at small scale (because rotation implies slower linear motion in the middle), as a value too small triggers overlap of a putative point source and hence a significant attenuation, but at the same time better speckle suppression is achieved from close-in-time frames. This value has to be increased if the field rotation is slow. Typical values span 0.5-1.5. In the end, an optimal trade-off value has thus to be found in order to reach the best overall S/N.

dr sets the radial step for each annulus of subtraction zones $\mathcal{S}$. As mentioned in section 2.4.4, it has to be the thinnest possible to allow for the most appropriate subtraction. It has only to be trade-off with the computational heaviness of subtraction at the pixel by pixel level. Contrarily to Lafrenière, Marois, et al. (2007), we choose thus to not take this parameter into account in our optimization. Instead, we define an initial radial step of 0.5 (in terms of FWHM) and an increase power law of exponent 1.3, so that the computation does not become more and more cumbersome radially outward.

tr_{init} is an additional parameter, not tested in (Lafrenière, Marois, et al., 2007). As the whole matrix to be inverted for the determination of the coefficients of the linear combination is usually poorly conditioned, we notice that it was better to operate the inversion on submatrices of the whole matrix[5] tr_{init} sets the truncation of the reference image pool sorted by correlation, for this block division. Before optimization, we set its value to 8.

Similarly to Lafrenière, Marois, et al. (2007), we first tested these parameters empirically in order to have an order of magnitude of the separate impact of the variation of each parameter on the level of the final (calibrated) contrast curve, which is our relevant *figure of merite* to minimize in this optimization. These first manual tests are not presented as we noticed later that our results were biased by an error in the injection of our fake companions. After fixing of this error, we directly endeavored algorithmic computation of the parameters.

3.3.2 Algorithmic computation of the parameters

The algorithmic computation of the optimal set of parameters was performed thanks to IDL dedicated function AMOEBA. The latter performs multidimensional minimization of any function $f(x)$, where x is an n-dimensional vector, using the *downhill simplex* method described in (Nelder & Mead, 1965). As its name indicates it is based on the use of simplex, which are the generalisation of the notion of triangle to arbitrary dimension. In addition, it relies only on function evaluations, not to the function's derivatives which is a common feature of classical algorithms seeking for minima.

AMOEBA is fed by different parameters, which are $f(x)$, tol_f, N_{max}, $\mathbf{p_0}$, $\mathbf{sc}$, $temp$, $\mathbf{p_l}$ and $\mathbf{p_u}$. The values chosen for each of them is argued hereunder.

$f(x)$ is the function to be minimized. In our case, it is our p-LOCI algorithm, which has been slightly modified in order to return the contrast curve, which is our figure of merit (hereafter *fom*) to be minimized.

tol_f is the function tolerance, i.e. the fractional decrease in the value of our *fom* in the terminating step. In view of the typical values of contrast curves reached by p-LOCI on our data ($\sim 10^{-4}$-10^{-5}), we fix this value to 10^{-7}.

$\mathbf{p_0}$ is the vector containing the initial starting point of the set of parameters for AMOEBA's tests. Based both on (Lafrenière, Marois, et al., 2007) and our empirical knowledge, we set the characteristic values for N_A , g, N_δ and tr_{init} to 125, 1, 1 and 16 respectively.

$\mathbf{sc}$ is the vector containing the problem's characteristic length scale for each dimension. AMOEBA will roughly use the range thus provided to choose the value of parameters to be tested. We set it to one third of the characteristic values for each parameter of $\mathbf{p_0}$. As we noticed that AMOEBA did not hesitate to probe well outside the range of values thus defined, $\mathbf{p_l}$ and $\mathbf{p_u}$

[5] We talk about *blockwise inversion*. The formula is based on the Schur complement. For a matrix composed of 4 submatrices, we have:

$$\mathbf{M}^{-1} = \begin{bmatrix} \mathbf{A} & \mathbf{B} \\ \mathbf{C} & \mathbf{D} \end{bmatrix}^{-1} = \begin{bmatrix} \mathbf{A}^{-1} + \mathbf{A}^{-1}\mathbf{B}(\mathbf{D} - \mathbf{C}\mathbf{A}^{-1}\mathbf{B})^{-1}\mathbf{C}\mathbf{A}^{-1} & -\mathbf{A}^{-1}\mathbf{B}(\mathbf{D} - \mathbf{C}\mathbf{A}^{-1}\mathbf{B})^{-1} \\ -(\mathbf{D} - \mathbf{C}\mathbf{A}^{-1}\mathbf{B})^{-1}\mathbf{C}\mathbf{A}^{-1} & (\mathbf{D} - \mathbf{C}\mathbf{A}^{-1}\mathbf{B})^{-1} \end{bmatrix}$$

were used as well. The latter are respectively the strict minimum and maximum values that AMOEBA is not allowed to outpass. They were set for N_A , g, N_δ and tr_{init} to [20,250], [0.25,2], [0.25,2] and [4,64] respectively.

N_{max} is the maximum number of p-LOCI iterations allowed before terminating. We fix it to 64, as we are the combinations of 4 different parameters.

3.3.3 Results

AMOEBA[6] was run a whole night on the set of observations of HD59967, with the different parameters aforementioned. It found the following optimized parameters (fom = 7.69 10^{-5} for this best combination):

$$N_A = 37.50,\ g = 1.66,\ N_\delta = 0.25 \text{ and } tr_{init} = 23.88$$

Qualitatively, in view of the set of parameters minimizing our figure of merit, it seems the optimization tends to minimize the number of resolution elements inside the optimization zone in a certain limit (i.e. it seems to favor a better correlation of the noise to be subtracted than preservation of the signal of a putative companion), give a radially elongated geometry of the optimization regions (g¿1), give a value different than unity for the linear size of the exclusion cone, and finally maximize the number of terms we keep before the truncation. HOWEVER, all proportions considered, the *fom* itself does not vary that much. The maximum variation is around 10% around the value of 8.10^{-5} for all the combinations of parameters that AMOEBA considered.

In fact, the algorithm does not seem to converge since the minimal *fom* value found was for the 26^{th} step out of 64. In addtion, the computed *fom* seems to vary randomly around 8.10^{-5} during the last 20 steps. It appears that either 64 steps was not enough to make it converge, either there is just no convergence of our *fom* in the range of value assigned to our set of 4 parameters, which convey Therefore, the main conclusion for that target is that we are mainly limited by the background. Variation of our parameters does not seem to affect that much the value of our figure of merit. Consequently, for similar targets (such as all the targets of the next chapter), the use of our standard set of parameters ($N_A = 100$, $g = 1$, $\delta = 1$ and $tr_{init} = 16$) is not inappropriate.

Nevertheless, it can be retained from this first successful optimization that our algorithm works, and that it should indeed be useful when applied to brighter sources.

[6]More information about AMOEBA can be found at http://star.pst.qub.ac.uk/idl/AMOEBA.html

Chapter 4

Application to science targets

The implemented all-in-one code can now be used on science targets. The instrumental configuration for the observation, the motivated choice of our targets and the specific parameters of these targets required to feed our code are first provided. Next, the results of our 2 sets of reduced images are given, insisting on the further investigations that can be led.

4.1 Preliminaries

4.1.1 Observation techniques

The data were acquired at VLT/NaCo in L'-band using a Lyot coronagraph, and with a performing AO system (NAOS), enabling to reach up to Sr$\sim$ 80%. The observation strategy was pupil-tracking, so that the data are meant to be reduced by an ADI-type reduction procedure. Our all-in-one code is thus well-suited. Detectability is limited by quasi-static speckles noise close to the star. At the same time, the background level in L'-band is critical for larger distances, so that in the end the choice of a short exposure time, set to 0.2s for each frame, is motivated. In total, an average of 45 minutes of integration time is spent for the different targets. All these choices enable to make the most of the different techniques capabilities to reach the highest contrasts.

The general strategy when applying our code is to first run c-ADI, which is generally good enough to detect a putative companion at separations above $\sim 3-4$". Next, p-LOCI is only applied on a region centered on the star with a radius of about ~ 4.5", as it is computationally fastidious but provides better contrasts close to the star. If a point-source is found with c-ADI, parameters of LOCI can be modified in order to apply it on a relatively thin annulus at the angular distance where ADI found the point-source. This can possibly enables a better contrast.

4.1.2 Targets

The importance of imaging exoplanets in debris disk has been pointed out in the context of formation models (section 1.4). All the targets that are the subject of reduction in this work were chosen based on the fact that they possess debris disks. The latter were discovered by Spitzer space telescope during a survey focused on FGK stars within 25 pc from the sun (Koerner et al., 2010). These disks have characteristic fractional infrared luminosities of ~ 0.01 %, and radii of 25 AU that were not spatially

resolved by Spitzer. The characteristic stellar age for these targets ranges between 0.1-2 Gyr. Among the 600 stars probed, 49 nearby stars were showing strong infrared excess at either 24 or 70 μm, conveying the presence of a debris disk. Four young stars known to have debris disks from the work of (Plavchan et al., 2009) were also considered. Among these 53 nearby stars, 16 were observable from the VLT at the time of the first set of observations (March 19 and 20, 2010) and 14 for the second (November 20 and 21, 2010).

For several reasons, we only focus on the detection of planetary companions (i.e. not circumstellar disks), so that only `ADI_f` and `LOCI_f` are used. As it can be interesting to try to re-detect the disks and further characterize them in L-Band, the priority stake is rather to discover or place limits on substellar companions that could be stirring or sculpting these disks, enabling to further constrain formation models. In particular, the direct detection of planetary or brown dwarf companions at the inner edge of the cold dust in the system, the configurations already seen in the Fomalhaut and HR 8799 systems. As will be seen, characteristic detection levels are of order 10^4 or 10 mag down to 0.2-0.3". According to Fortney et al. (2008)'s *core accretion* start model, this corresponds to 10-15 M_{Jup} companions orbiting 5 AU around a 1 Gyr old H=9 star located at 25 pc. These values are more pessimistic, but more realistic, than for Burrows et al. (1993) and Baraffe et al. (1998, 2002, 2003) models.

The use of `ADI_s` and `LOCI_s` in an attempt to re-detect the disks is postponed to after the end of this thesis. Detection of their disks in scattered light would only be possible if they are oriented edge-on, or if the dust is confined to narrow rings. Indeed, if the disk is oriented pole on, it is entirely self-subtracted by c-ADI or LOCI.

4.2 Results

The characteristics of each target of the first and second set of observations that will be reduced by our whole-in-one code are given in tables 4.1 and 4.2 respectively.

The reduced data for the first set of images are given hereafter. For each figure, the upper left image is the final median obtained after c-ADI and upper right image is the final median obtained after p-LOCI. Both images are smoothed with a gaussian filter in order to facilitate the detection of a companion. The kernel of the gaussian filter is set to the size of the FWHM in pixel, i.e. (λ/D) plsc.

Lower left and lower right diagrams are the contrast curves, respectively after c-ADI and p-LOCI. On the contrast curve of p-LOCI, dotted line is the non-calibrated detection limit whereas the solid line represents the true detection limit, after division by the attenuation factor estimated thanks to the injection of fake companions.

For each target, a selection of n_g (the number of *good* frames) frames is made among all the frames available, thanks to parameter `concat`. This selection is based on the presence of drifts (star leaking out of the mask) in some frames, which are thus rejeccted. Each frame is constituted of 25 acquisitions of 0.2s. The total integration time $t_{int,tot}$ for a specific target is thus given by 25*0.2*n_g. The total parallactic variation Δp is also given.

Individual comments are to be found in the respective captions.

p.	Target	R.A.(J2000)	δ (J2000)	Mag.(L')	Spectral type
86	HIP 44295	09 01 17.47	+15 15 56.8	5.68	K4
87	HD 59967	07 30 42.51	-37 20 21.7	5.1	G2
88	HD 135599	15 15 59.17	+00 47 46.9	4.81	K0
89	HIP 36827	07 34 26.17	-06 53 48.0	5.86	K2
90	HD 73350	08 37 50.29	-06 48 24.8	5.1	G0
91	HIP 58451	11 59 10.01	-20 21 13.6	5.44	K2
92	HIP 74975	15 19 18.80	+01 45 55.5	3.91	F8III
93	HIP 72848	14 53 23.77	19 09 10.1	4.16	K2
94	HIP 77952	15 55 08 56	-63 25 50.6	2.1	F2III
95	HIP 85561	17 29 06.56	-23 50 10.0	6.14	K5
96	GJ 758	09 01 17.47	+15 15 56.8	4.34	K4
97	HIP 58576	12 00 44.45	-10 26 45.7	3.89	G9
98	HIP 73633	15 03 06.11	-41 59 33.2	5.88	K3

Table 4.1: Characteristics of the targets of the first set.

#	Target	R.A.(J2000)	δ (J2000)	Mag.(L')	Spectral type
99	HIP 105184	21 18 27.27	-43 20 04.7	5.26	G5
100	HIP 1499	00 18 41.86	-08 03 10.8	4.9	G0
101	HIP 17439	03 14 09.17	-38 16 54.38	4.94	K2
102	HIP 19893	04 16 02.0	-51 29 12.1	3.58	F1V
103	HIP 25775	05 30 14.00	-42 41 50.4	6.23	M0
104	HD 59967	07 30 42.51	-37 20 21.7	5.1	G3
105	HIP 43860	08 56 07.0	-64 39 38.3	7.96	F8V
106	HIP 108598	21 59 67.2	-54 39 18.0	7.5	K0V
107	TYC-635-90-1	02 28 57.0	+12 00 12.8	6.76	F5V
108	HIP 7699	01 39 08.1	-56 25 47.8	6.01	F5V
109	HIP 30503	06 24 43.88	-28 46 48.04	8.16	G1.5V
110	HIP 30729	06 27 21.4	-33 06 50.3	5.1	G3V

Table 4.2: Characteristics of the targets of the second set.

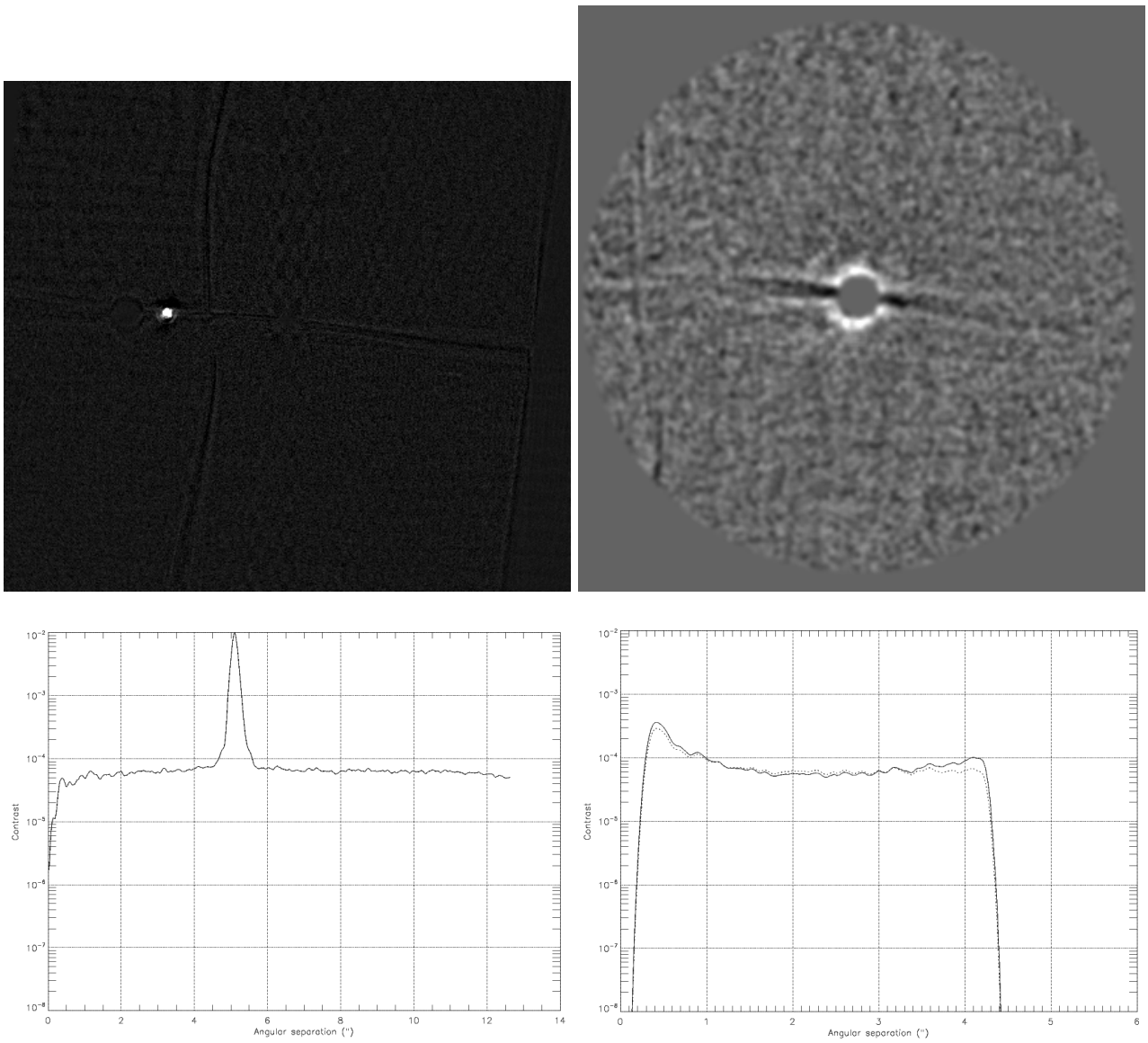

Figure 4.1: HIP 44295 A and B. The binary is clearly visible, both on ADI image and its contrast curve. No other companion is detected. Both contrast curves are very flat, at about 10^{-4}, conveying the fact that we are limited by the background, not by speckles. The log indicates that atmospheric conditions were not particularly good at the beginning of the observation (seeing of 0.9", cloudy) so that the floor of the contrast curve is not very deep.

$$n_g = 120 \qquad t_{int,tot} = 600 \text{ s} \qquad \Delta p = \text{-}11.8\ ^\circ$$

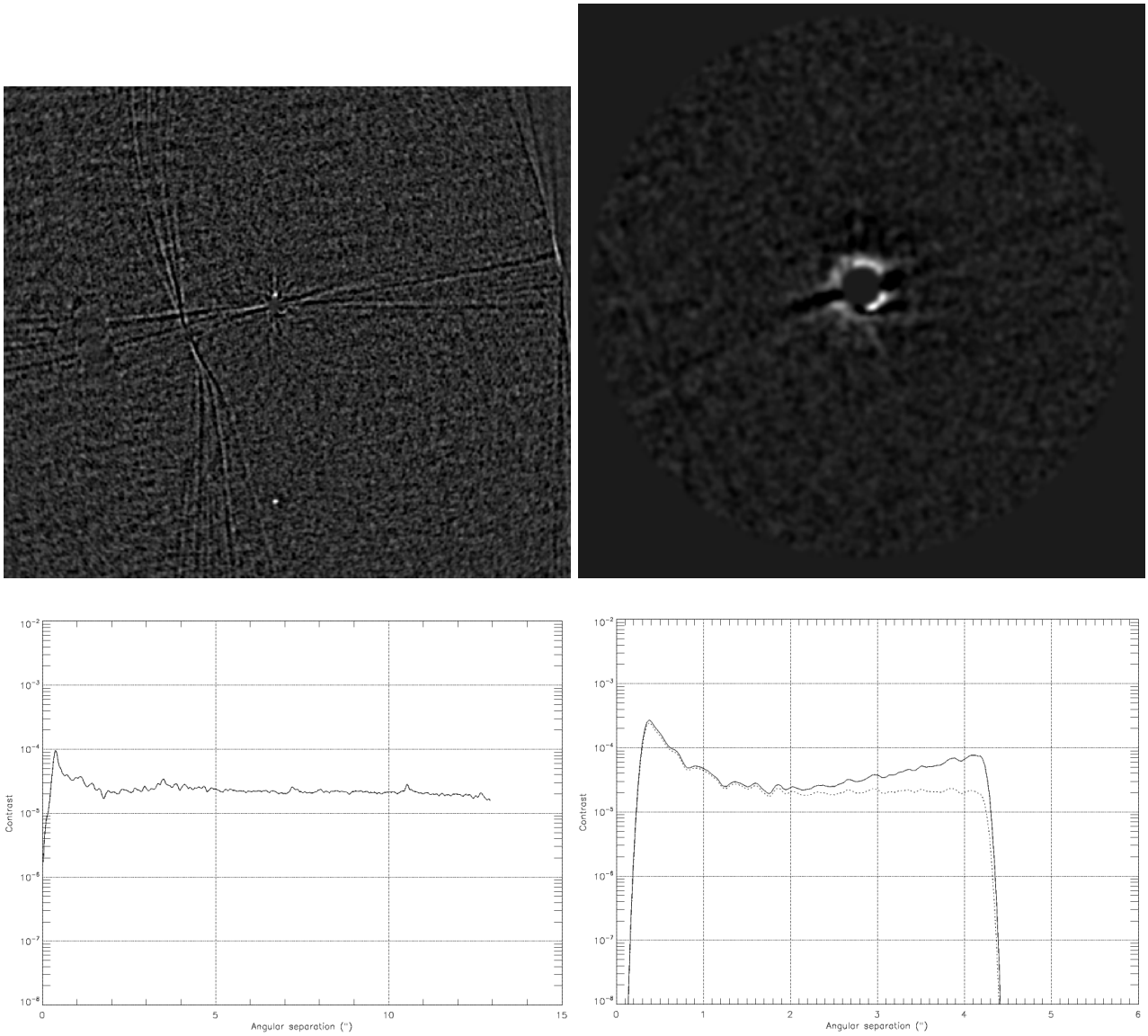

Figure 4.2: HD 59967. A companion can be found at great angular distance in the lower part of the ADI image. It can also be detected by a very faint peak at 10.5" in the ADI contrast curve. However, Dimitri had already followed up this object and it revealed to be a background star. Nothing is found by LOCI.

$$n_g = 144 \qquad t_{int,tot} = 720 \text{ s} \qquad \Delta p = 21.3\ ^\circ$$

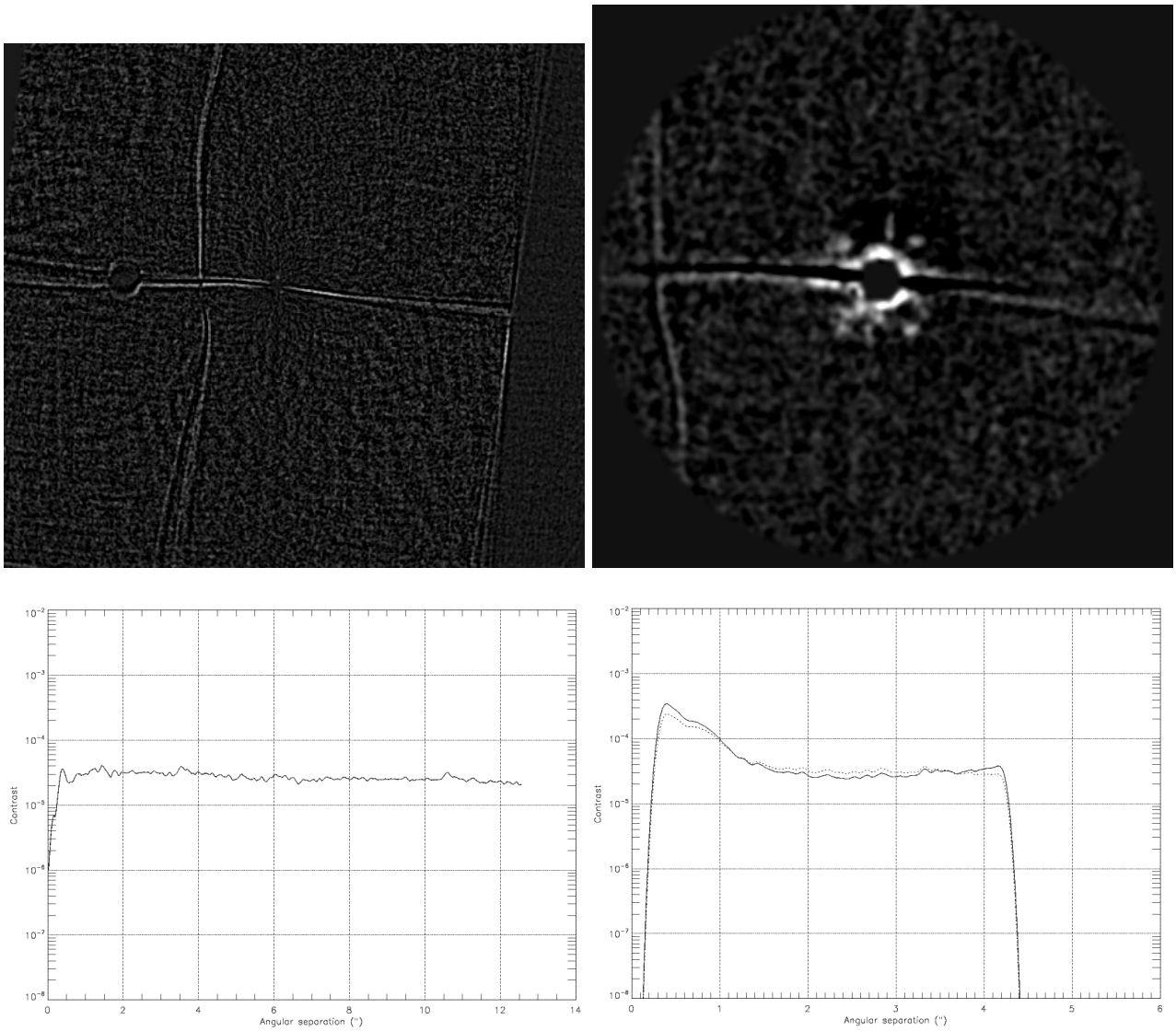

Figure 4.3: HD 135599. Nothing is found by ADI. The four symmetric points that are seen at the corners of the central star in the LOCI image is a common spurious pattern that should not be confused with companions.

$$n_g = 88 \qquad t_{int,tot} = 440 \text{ s} \qquad \Delta p = \text{-}7.0\ ^\circ$$

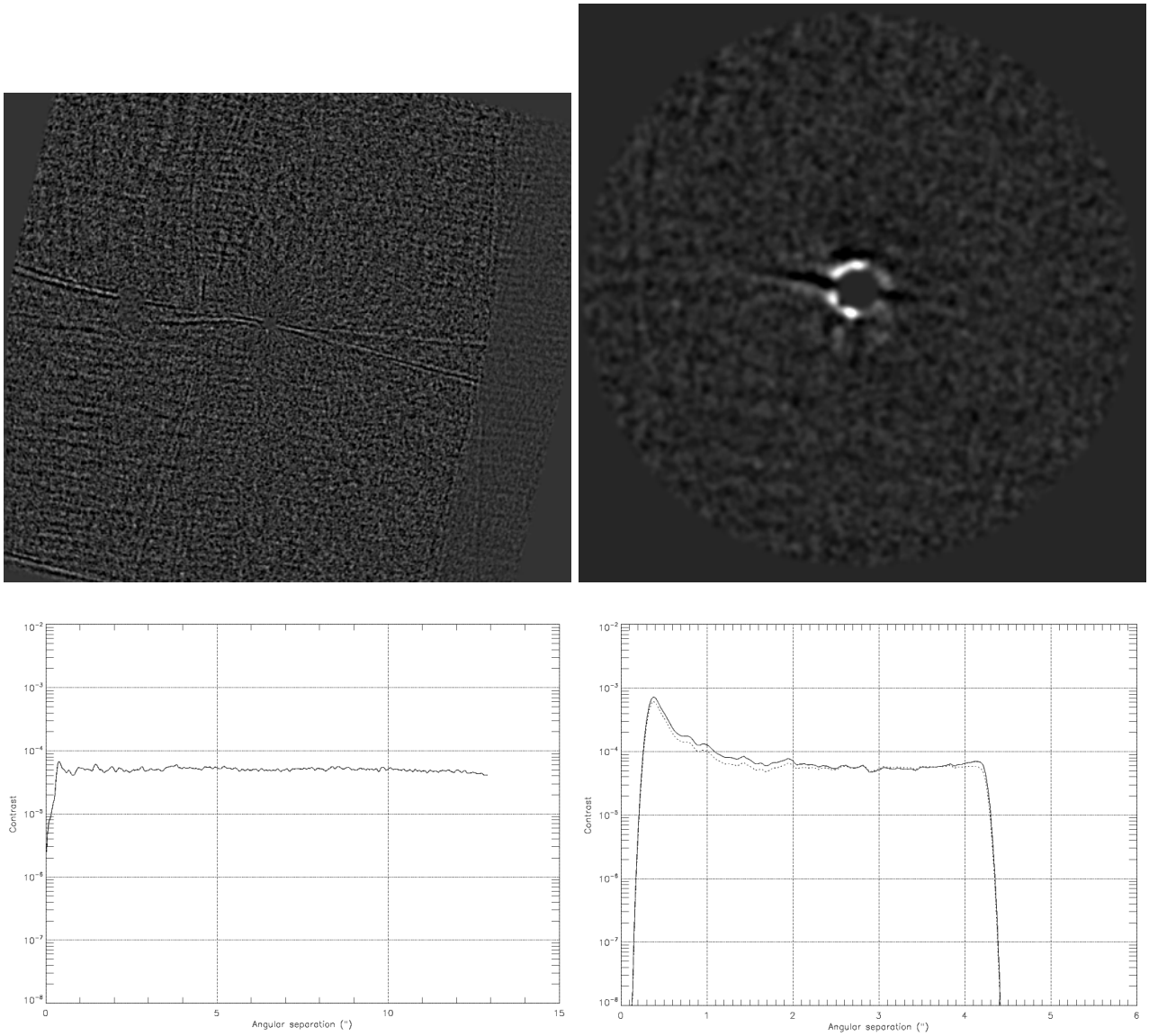

Figure 4.4: HIP 36827. Again, nothing is found neither by ADI nor by LOCI. The ADI contrast curve cannot be flatter. It is noteworthy that if ADI *seems* to reach better contrast at smaller distance, it is in reality not the case as no calibration is performed on ADI concerning the attenuation caused by self-subtraction.

$$n_g = 128 \qquad t_{int,tot} = 640 \text{ s} \qquad \Delta p = \text{-}14.0\ ^\circ$$

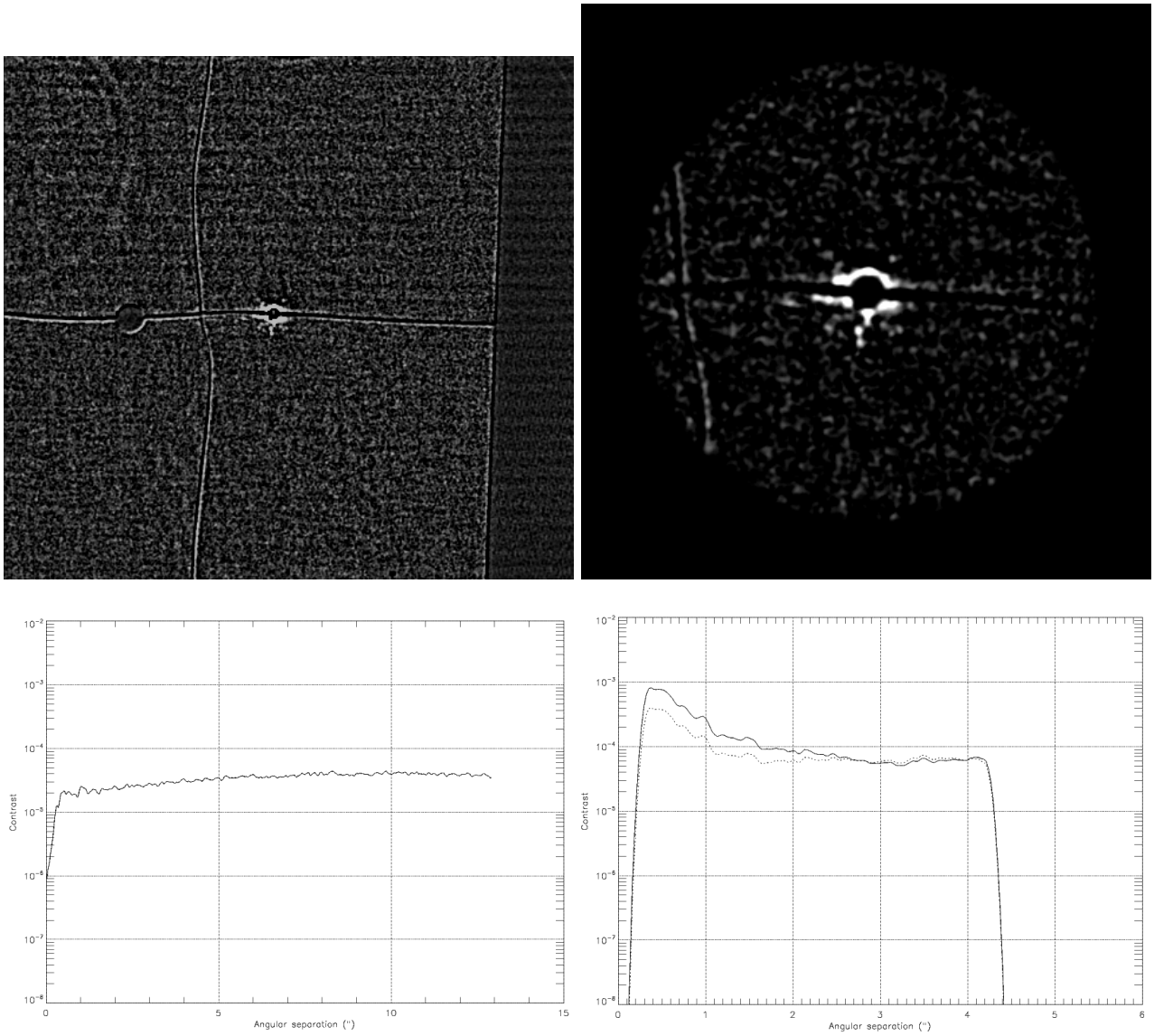

Figure 4.5: HD 73350. Nothing is found by ADI. For LOCI, the points seen under the star are more liekly speckles than real objects. Very limited number of frames and parallactic variation.

$$n_g = 28 \qquad t_{int,tot} = 140 \text{ s} \qquad \Delta p = \text{-}1.79\ ^\circ$$

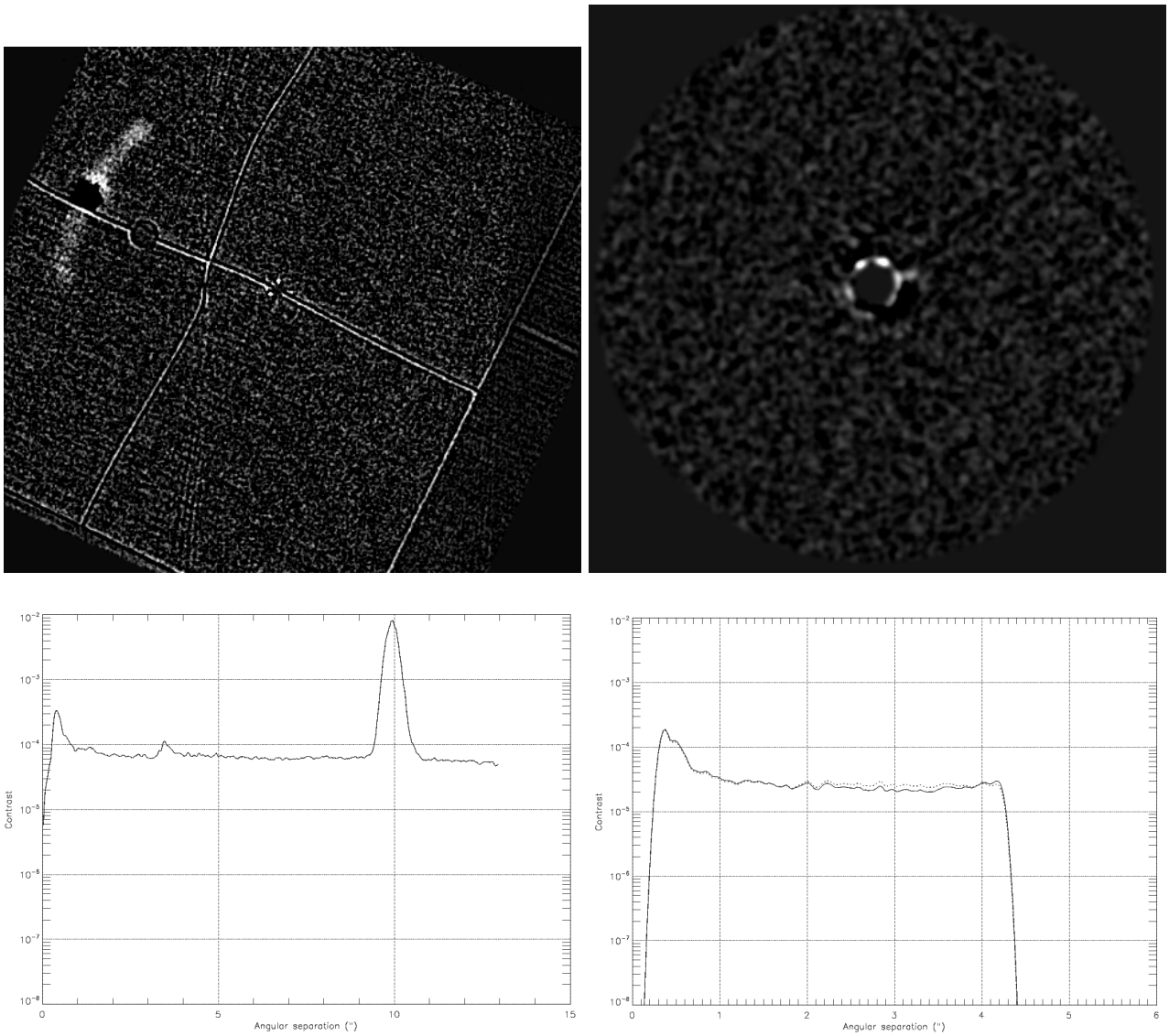

Figure 4.6: HIP 58451. The binary companion is clearly seen from the ADI image and its contrast curve. The faint peak in the middle of the contrast curve is interpreted as the bright central part of the vertical bar of the coronagraph. Nothing is found in the field of LOCI.

n_g = 356 $t_{int,tot}$ = 1780 s Δp = -144.48 °

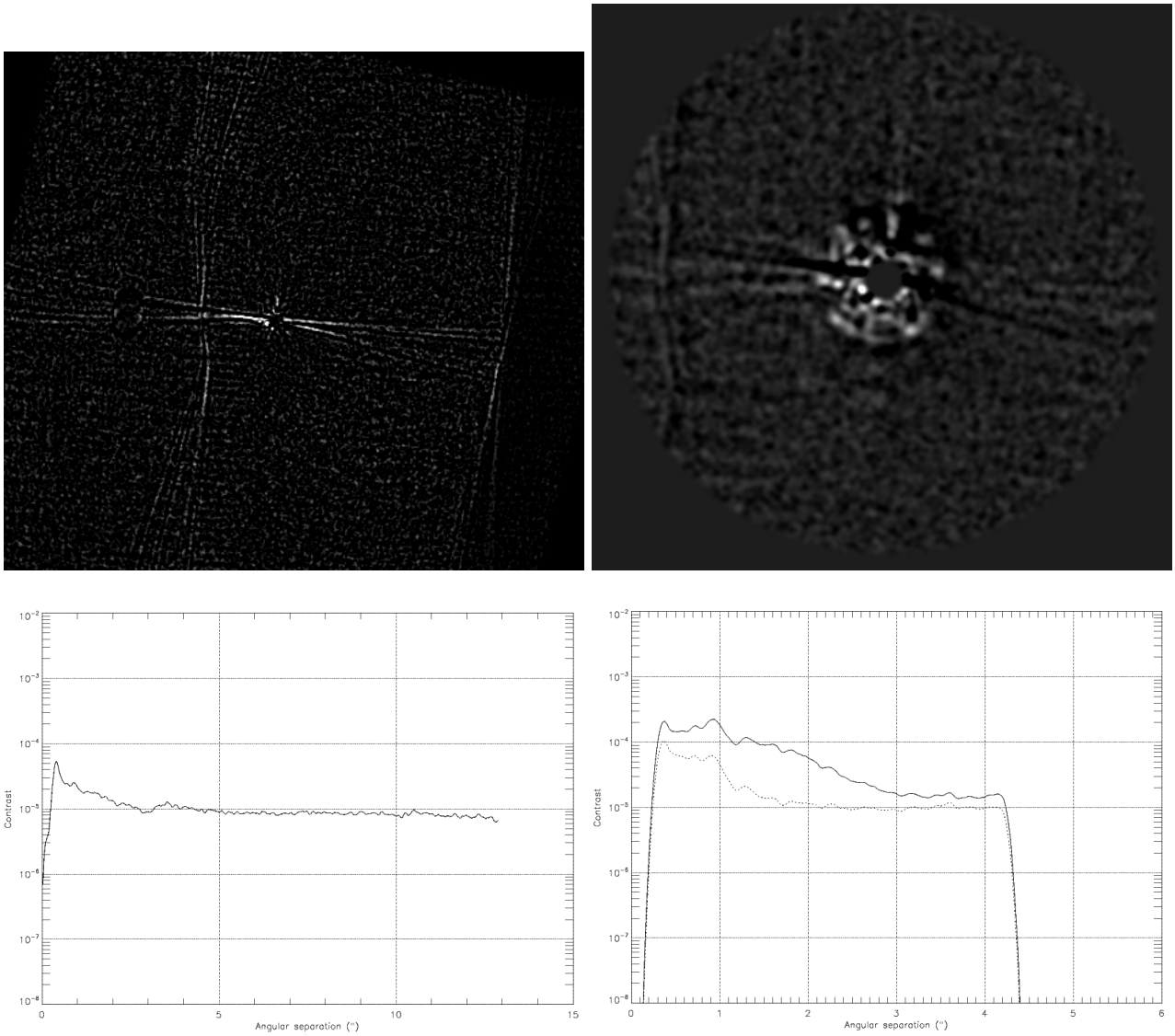

Figure 4.7: HIP 74975. Nothing is found by ADI. In the field of LOCI, we see this time a pattern of speckles around the star. Indeed, we notice in table 4.1 that the L-band magnitude of HIP 74975 is significantly brighter than former stars, hence triggering brighter quasi-static speckles. In this case, we face the classical problem induced by speckles, as we cannot determine if there is no real companion among the most point-like speckles.

$$n_g = 149 \qquad t_{int,tot} = 745 \text{ s} \qquad \Delta p = \text{-}14.7\ ^\circ$$

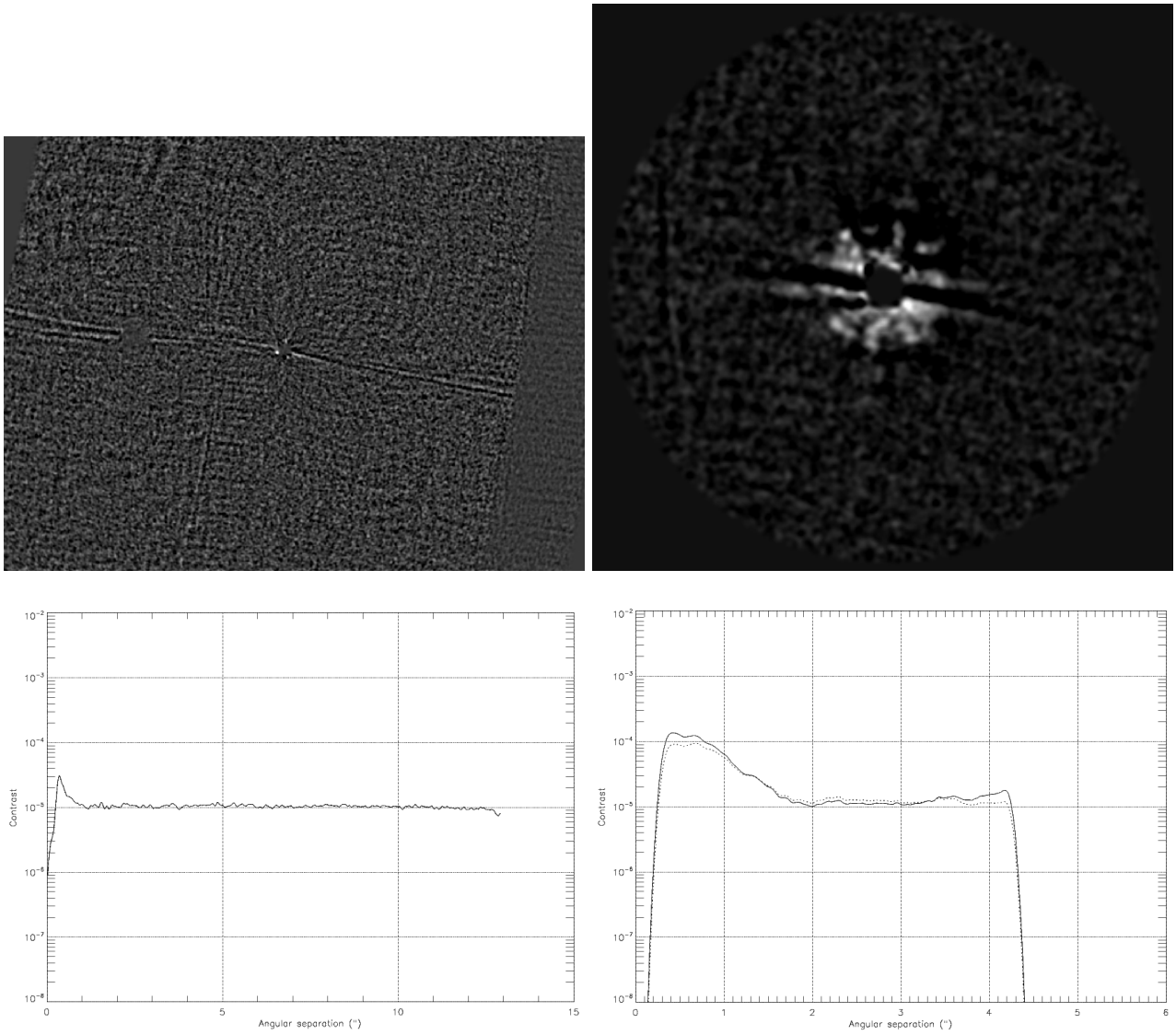

Figure 4.8: HIP 72848. The level of contrast reached by ADI is remarkable, 10^{-5} over the whole radial extent. Indeed, the log indicates that there were good atmospheric conditions at that moment. HIP 72848 also induces a pattern of quasi-static speckles. Again, it would be presumptious to assert that there are companions in it.

$$n_g = 112 \qquad t_{int,tot} = 560 \text{ s} \qquad \Delta p = \text{-}13.2\ ^\circ$$

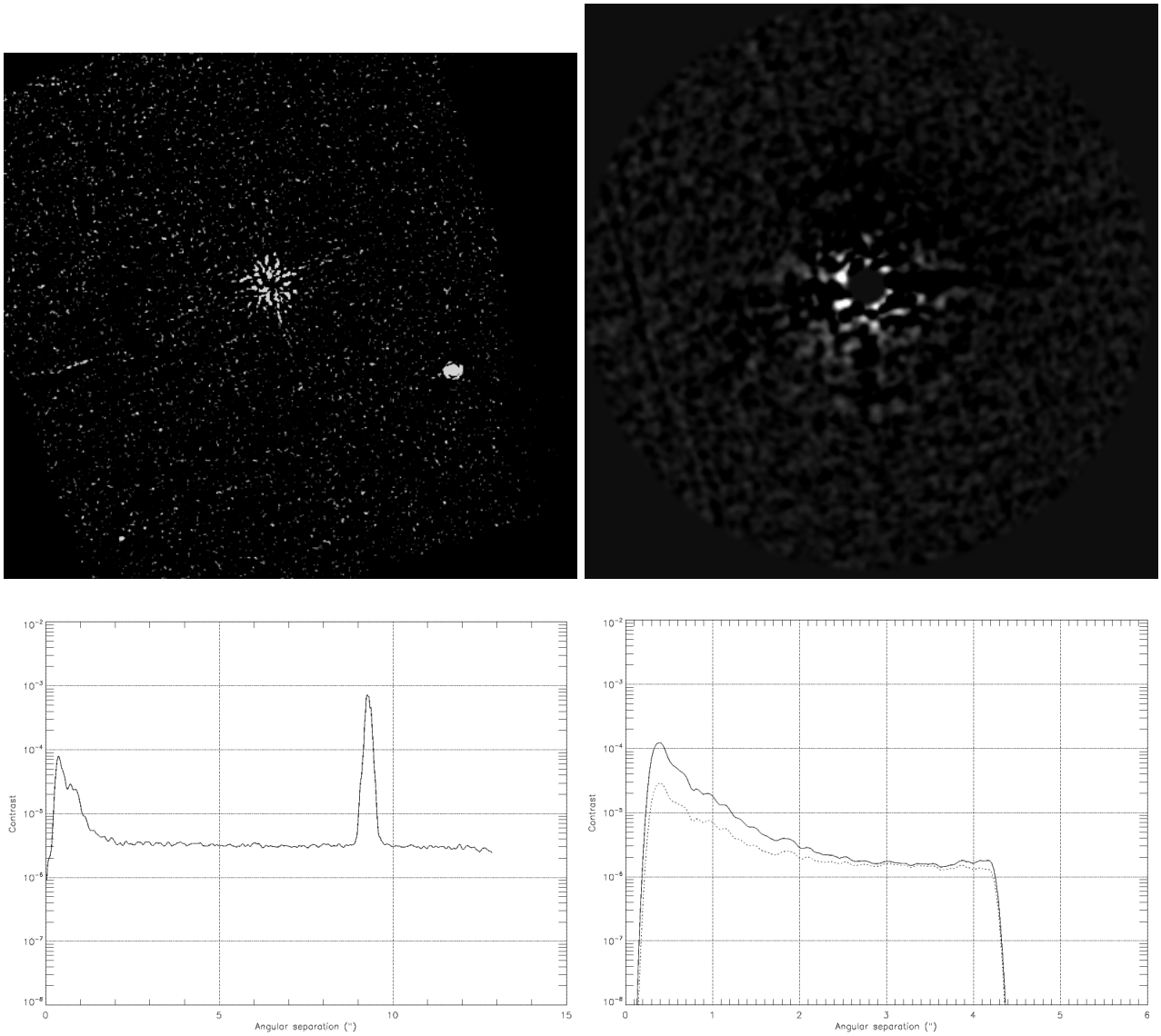

Figure 4.9: HIP 77952. There is obviously a star in the lower right part of the ADI image. At the extreme lower left edge, a possible companion is detected. However, in view of the angular separation involved, it is much more likely to be a background star. Nothing can be said from the LOCI image.

$$n_g = 216 \qquad t_{int,tot} = 1080 \text{ s} \qquad \Delta p = 33.1\ ^\circ$$

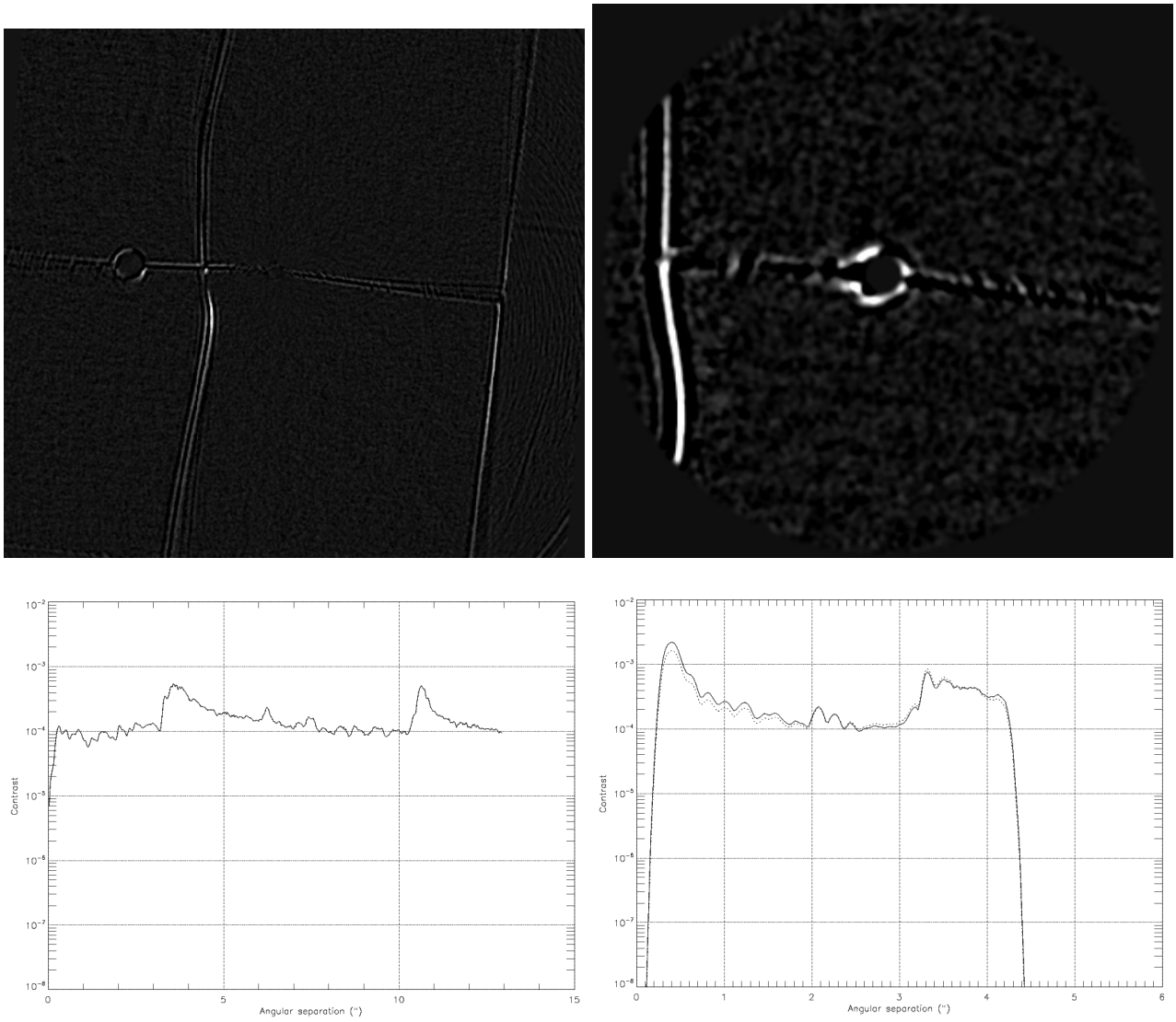

Figure 4.10: HIP 85561. This time, there are some fluctuations in the contrast curves, however they are due to the bars of the coronagraph. The number of good frames and the total parallactic variation are likely to be too small to detect anything.

$n_g = 88$ $t_{int,tot} = 440$ s Δp = -5.3 °

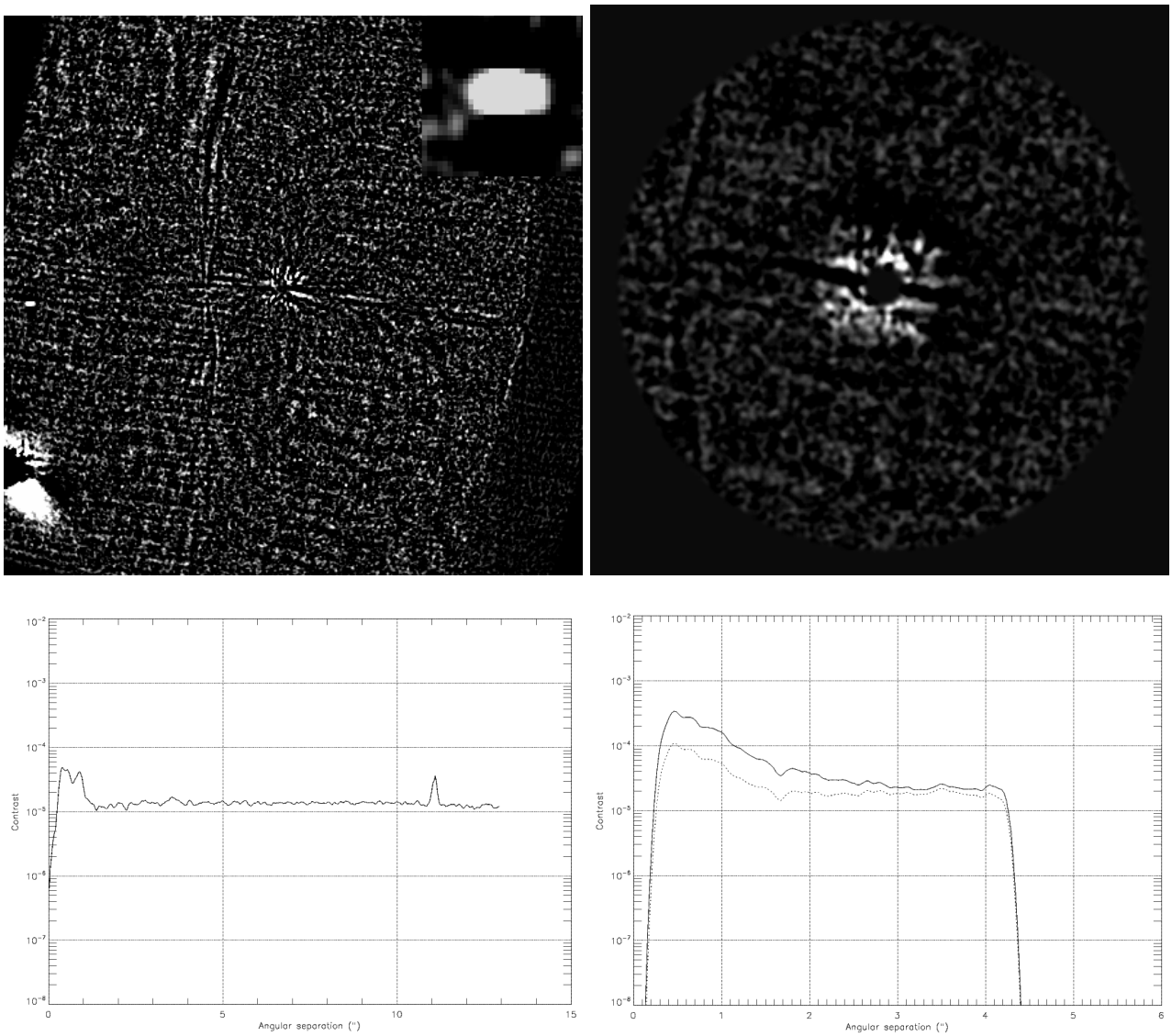

Figure 4.11: GJ 758. The ADI frame is somewhat more interesting. There is first obviously a bright source in the lower left part. A bit upper, one can find an elongated source, which has been re-scaled in the upper-right part for better visibility. There are two hypotheses, either this elongated source is a close binary, whether bound to the central star or not, or it is just an effect of the PT drift problem.

$$n_g = 118 \qquad t_{int,tot} = 590 \text{ s} \qquad \Delta p = \text{-}16.6\ ^\circ$$

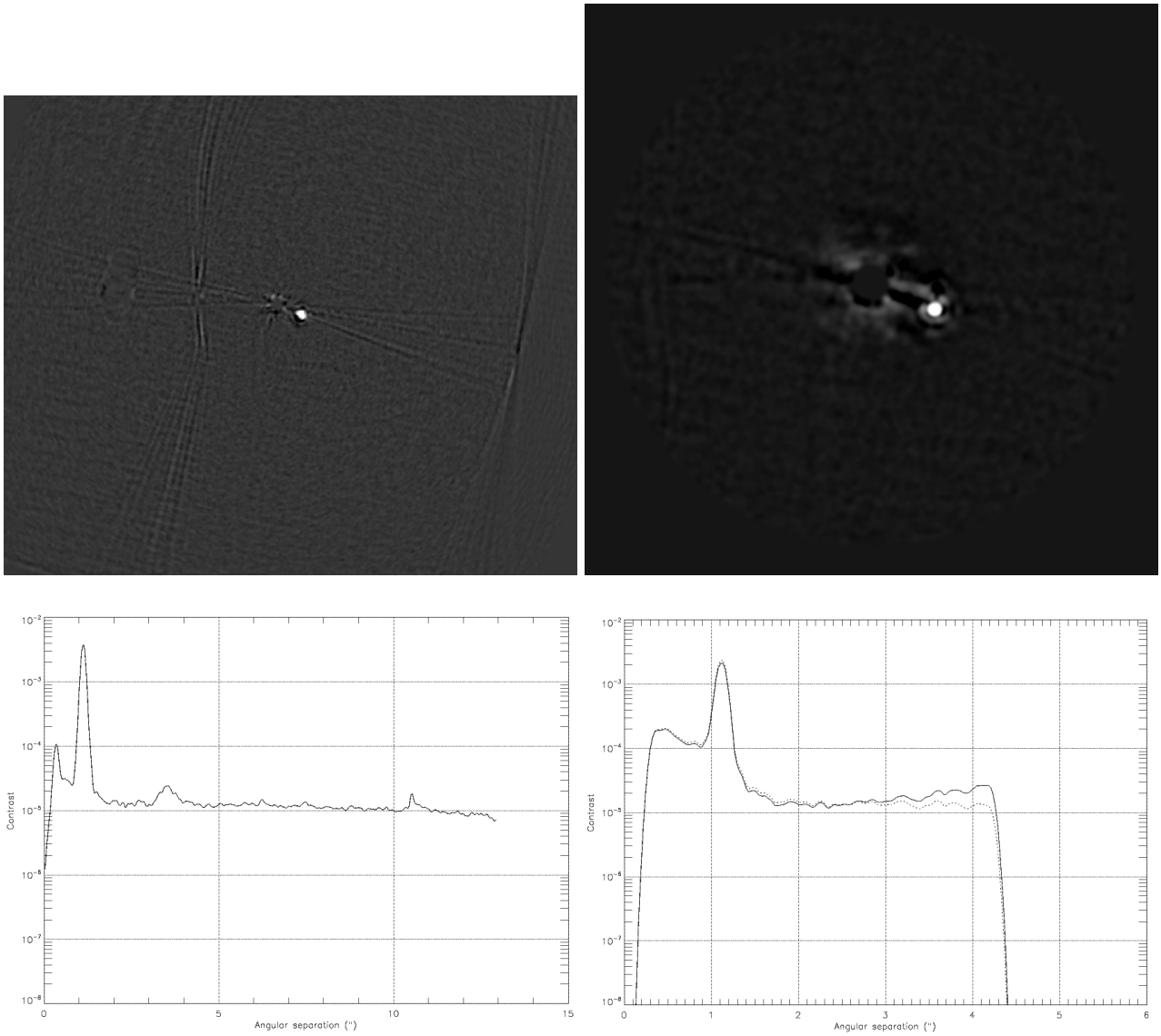

Figure 4.12: HIP 58576. It is clear from all the frames and contrast curves that we are facing a binary system. The small feature in the contrast curve at about 10.5" seems to be due to bright edges of the other mask of the coronagraph.

$n_g = 64$ $t_{int,tot} = 320$ s $\Delta p =$ -19.29 °

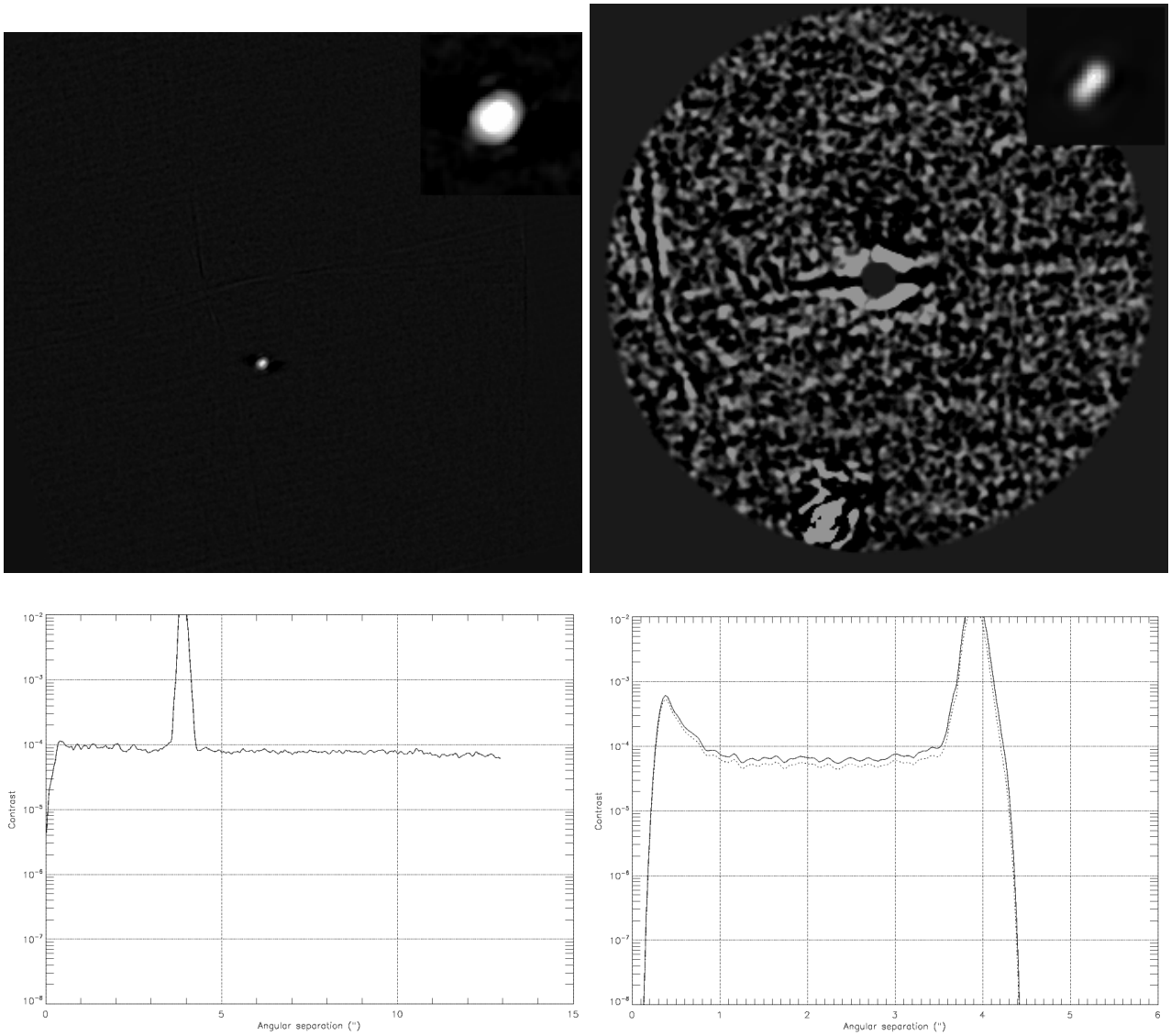

Figure 4.13: HIP 73633. Finally, this last target of the first set is also revealing a binary, or maybe a triple one as the re-scaled images show again an elongation which could be interpreted as a close binary.

$$n_g = 170 \qquad t_{int,tot} = 850 \text{ s} \qquad \Delta p = 19.7\ ^\circ$$

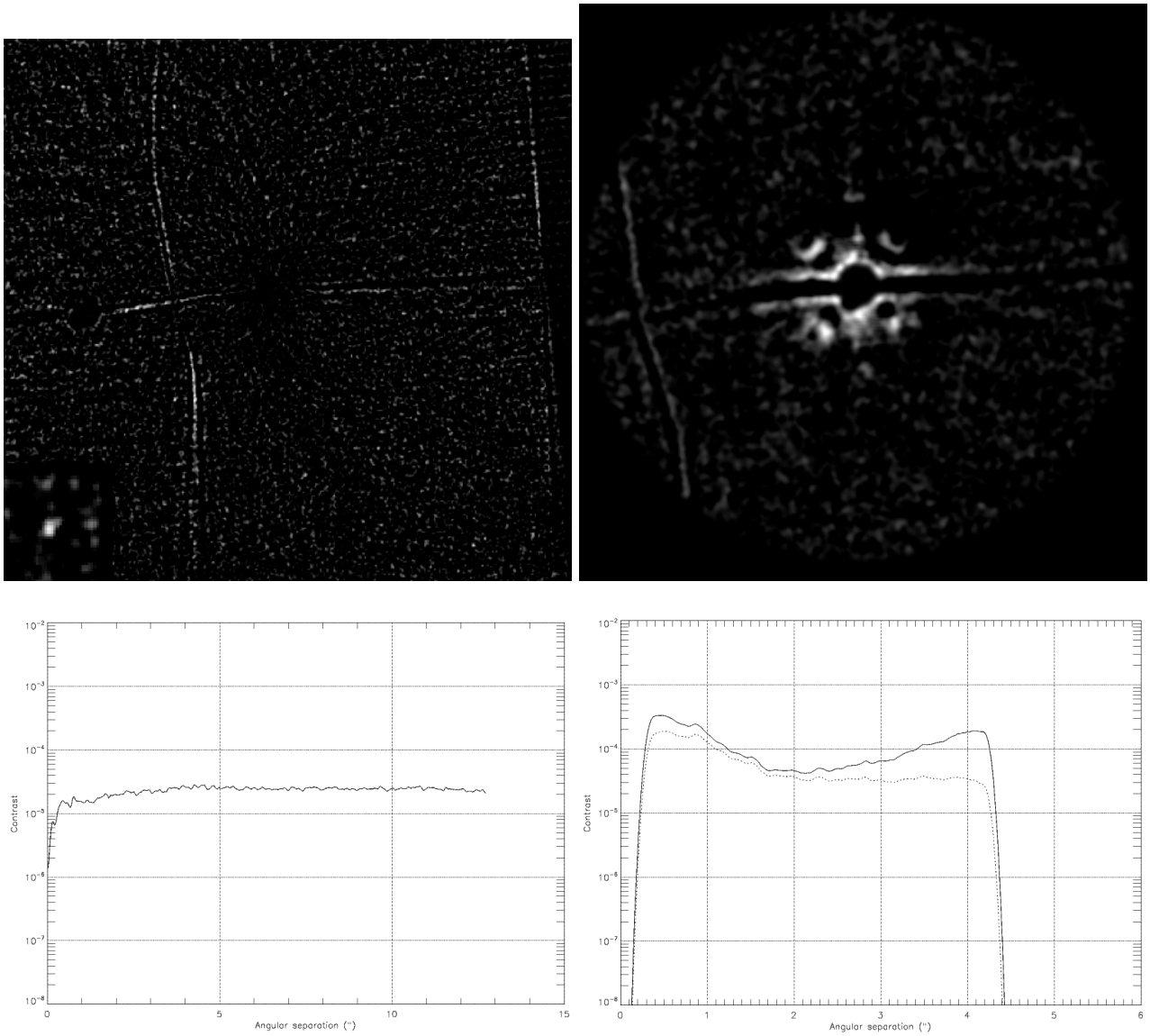

Figure 4.14: HIP 105184. The ADI image displays a faint spot on the left of the vertical bar of the coronagraph (which was discerned only thanks to knowledge of Dimitri). This spot is re-scaled in the lower-left corner of the image for better visibility. The LOCI image displays the same spurious pattern as for HD135599.

$$n_g = 79 \qquad t_{int,tot} = 474 \text{ s} \qquad \Delta p = 5.2\ ^\circ$$

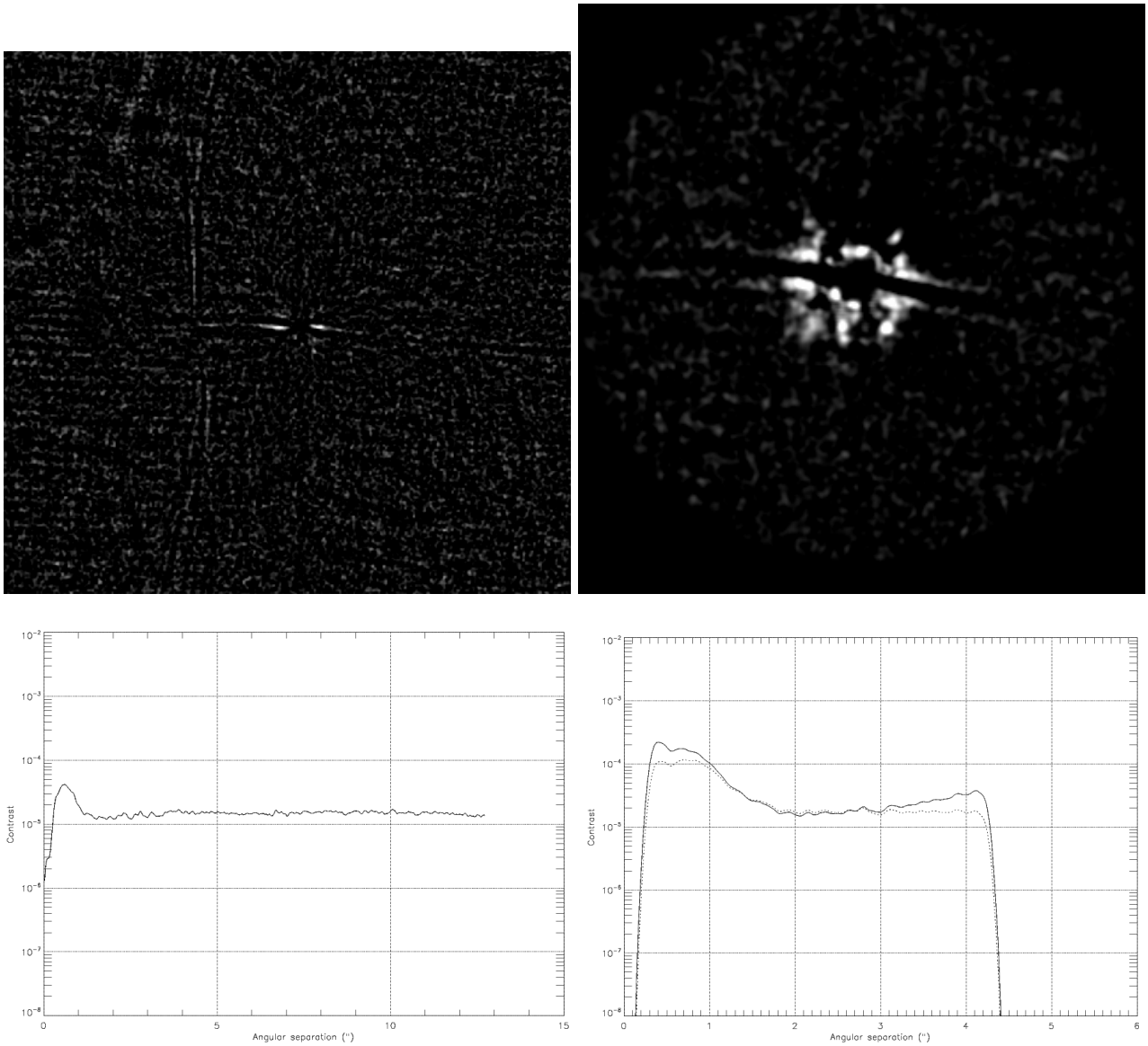

Figure 4.15: HIP 1499. Nothing to declare with ADI. As for LOCI, the quasi-speckles curb again the detection, though the bright spot at the lower-right part could be considered a candidate.

$n_g = 125$ $t_{int,tot} = 750$ s $\Delta p =$ -9.1 °

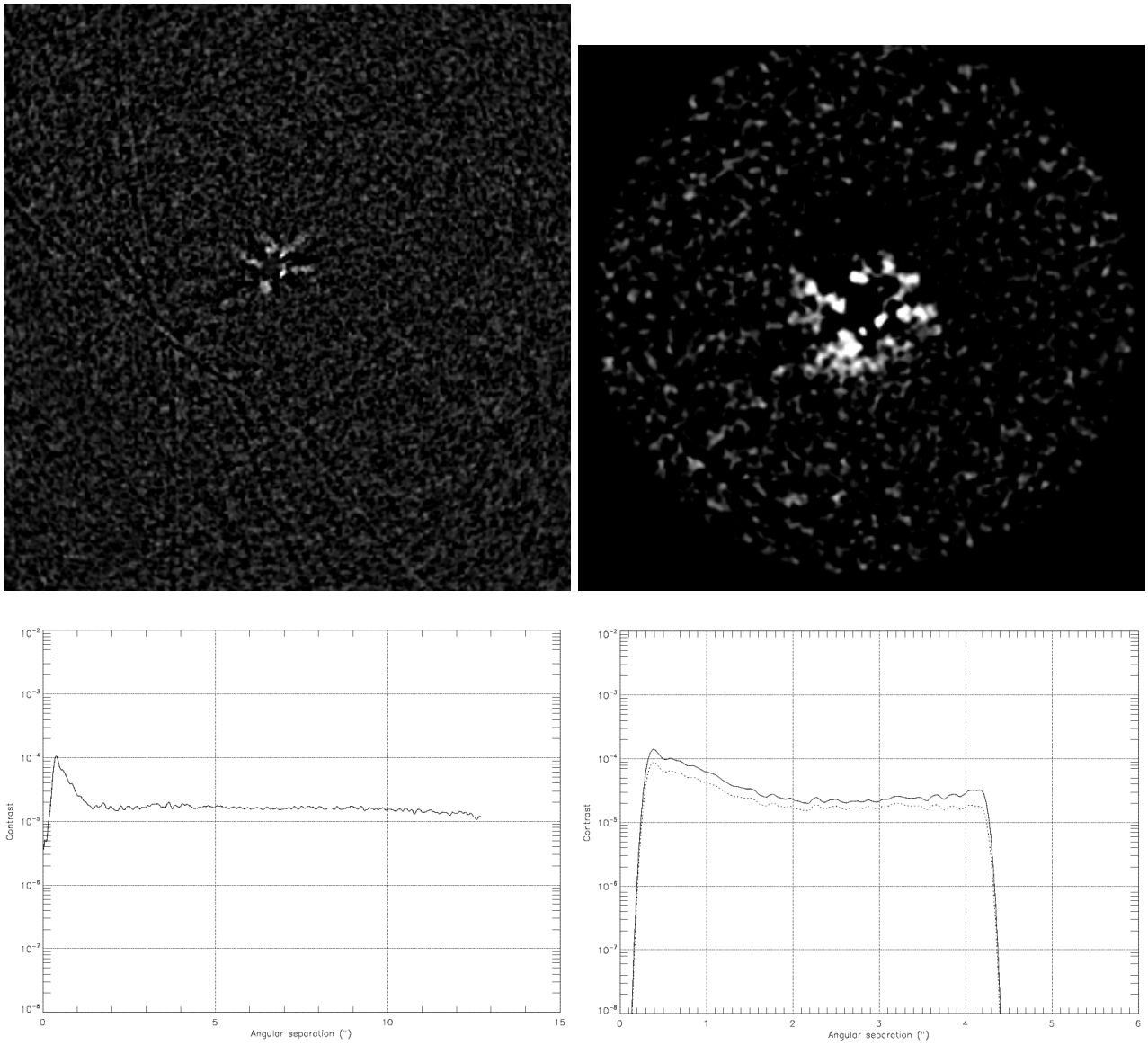

Figure 4.16: HIP 17439. Nothing to declare though the parallactic variation is excellent. The contrast curves are very flat out of the central part.

$$n_g = 116 \qquad t_{int,tot} = 696 \text{ s} \qquad \Delta p = 50.3\ ^\circ$$

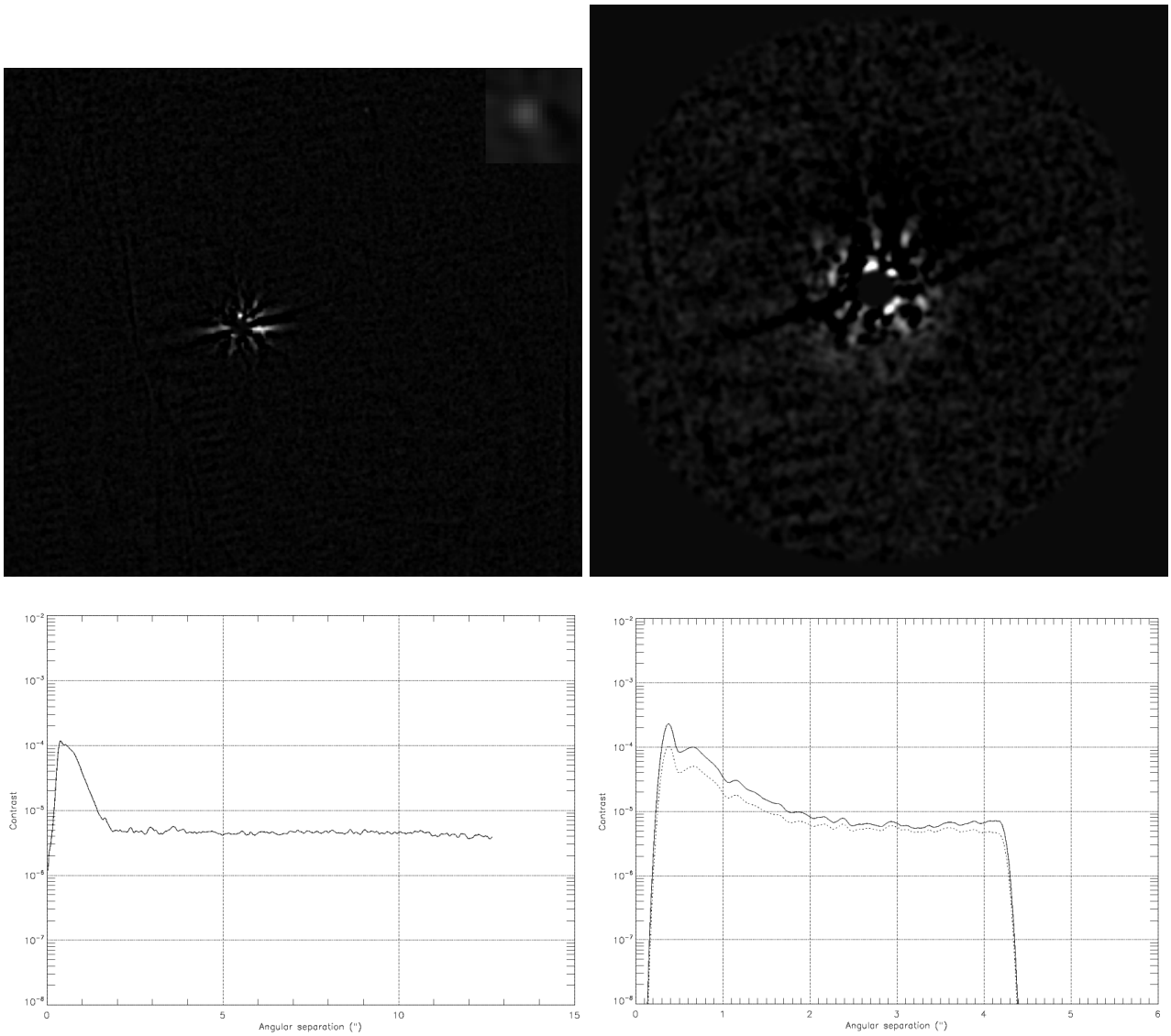

Figure 4.17: HIP 19893. An object is found far of the star, at the upper edge of the frame, a little to the right, at more than 10". It is rescaled on the top right corner. Again, there is low probability it is indeed a bound companion. Nothing to declare with LOCI.

$$n_g = 116 \qquad t_{int,tot} = 696 \text{ s} \qquad \Delta p = 22.4\ ^\circ$$

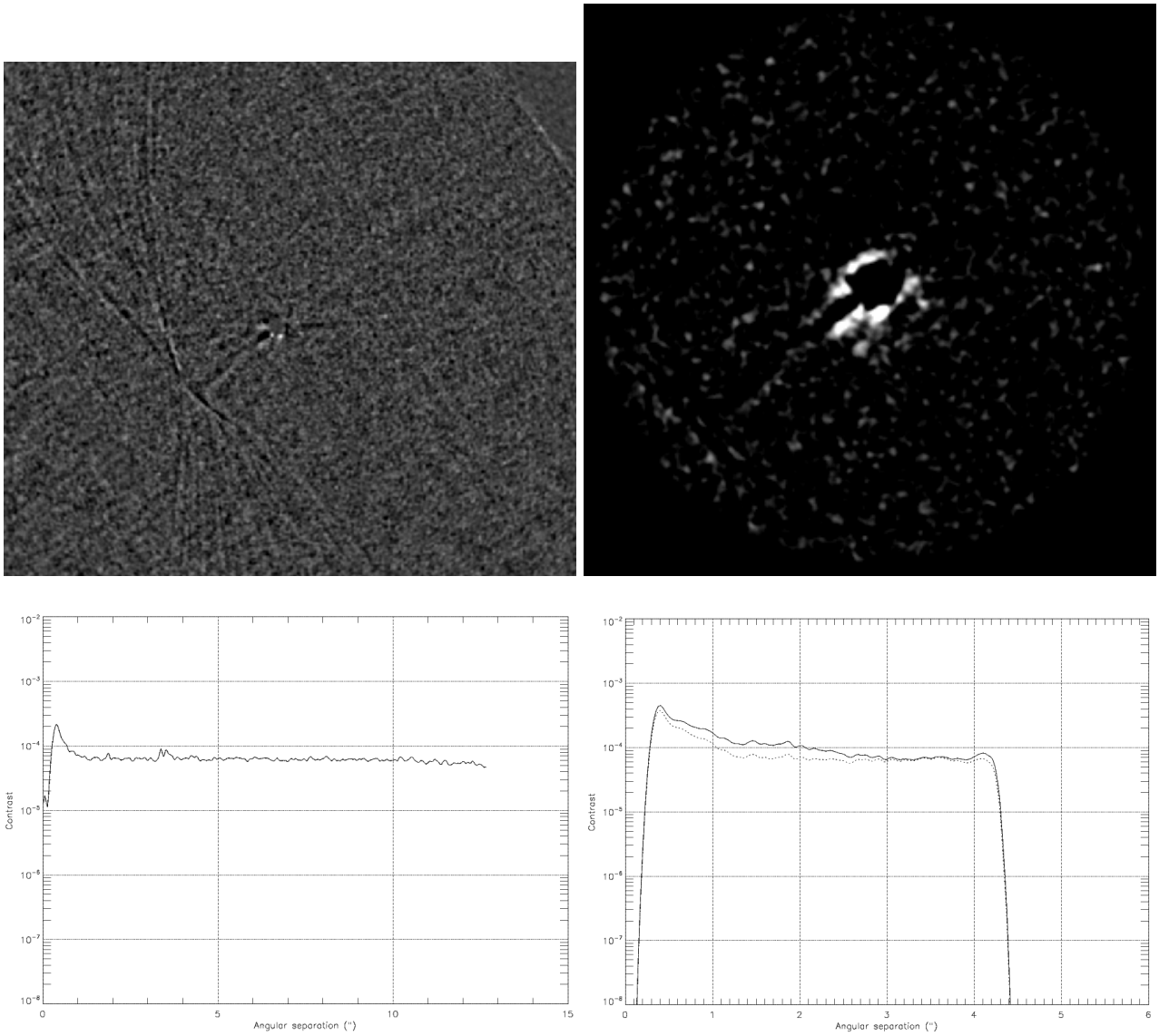

Figure 4.18: HIP 25775. Nothing to declare, albeit there is a good parallactic variation.

$$n_g = 97 \qquad t_{int,tot} = 582 \text{ s} \qquad \Delta p = 46.2\ ^\circ$$

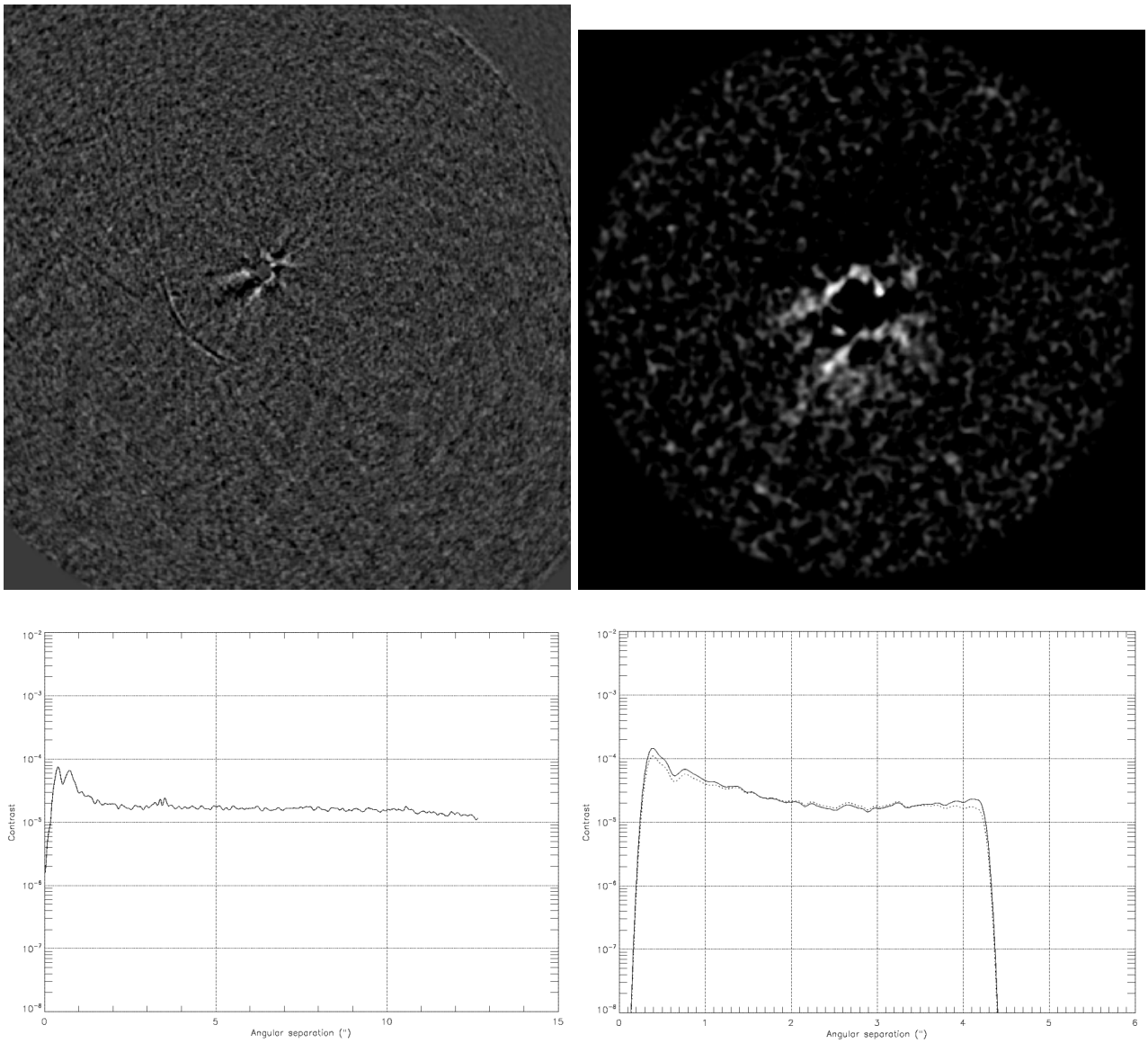

Figure 4.19: HD 59967. Whereas a background star had been immediately detected from the observations of HD 59967 during the first run, this time, it is not visible, though the parallactic variation is greater.

$$n_g = 124 \qquad t_{int,tot} = 744 \text{ s} \qquad \Delta p = 58.6\ ^\circ$$

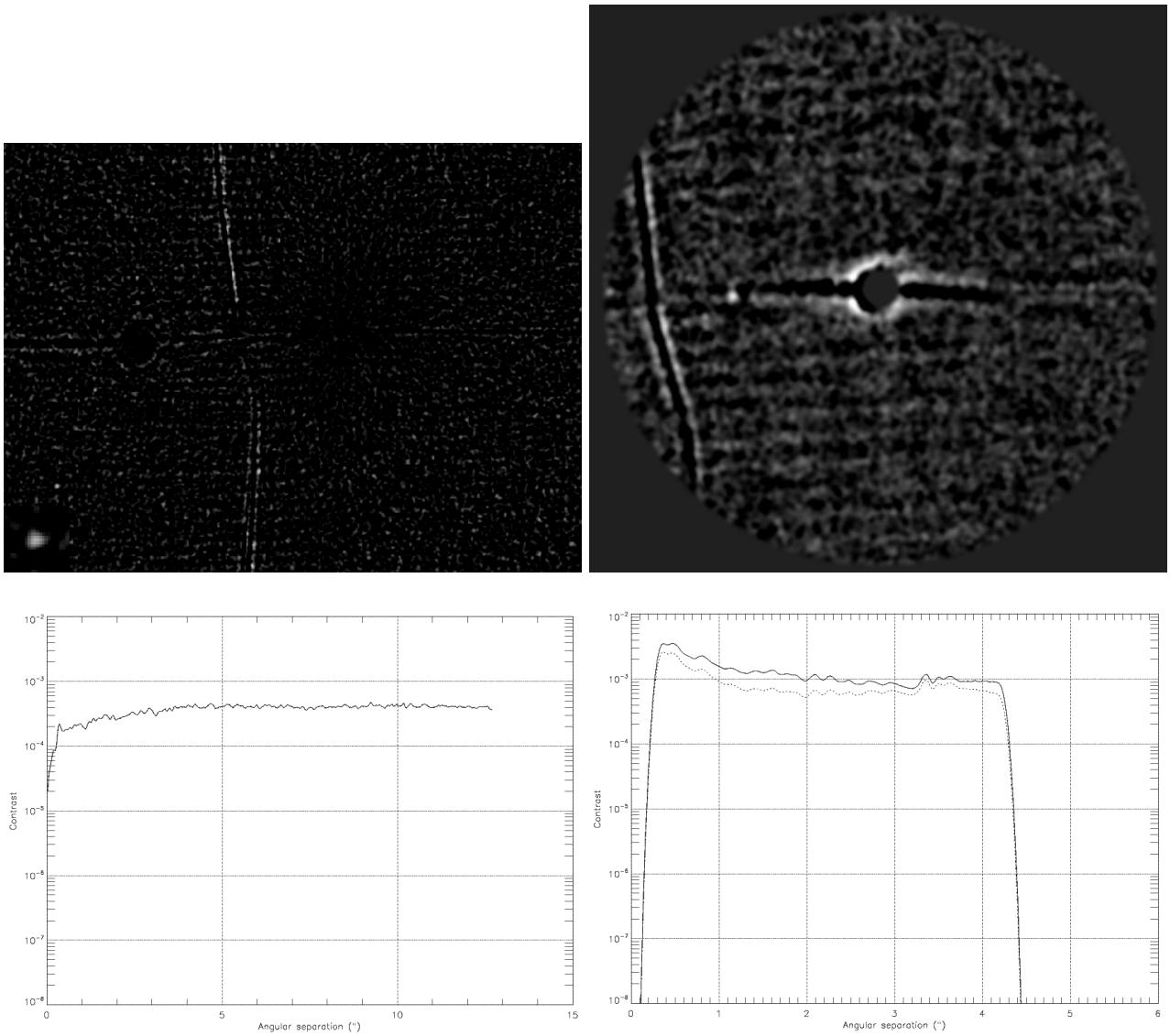

Figure 4.20: HIP 43860. The atmospheric conditions are getting bad as both the log and the level of the contrast curves testify. Nonetheless, an object is found by ADI far to the bottom-left, close to the corner. It is re-scaled for better visibility. In view of the very small amount of frames and parallactic variation, this object must be intrisically very bright. In view of both its angular separation and brightness, it is much more likely to be a background star.

$$n_g = 35 \qquad t_{int,tot} = 210 \text{ s} \qquad \Delta p = 3.9\ ^\circ$$

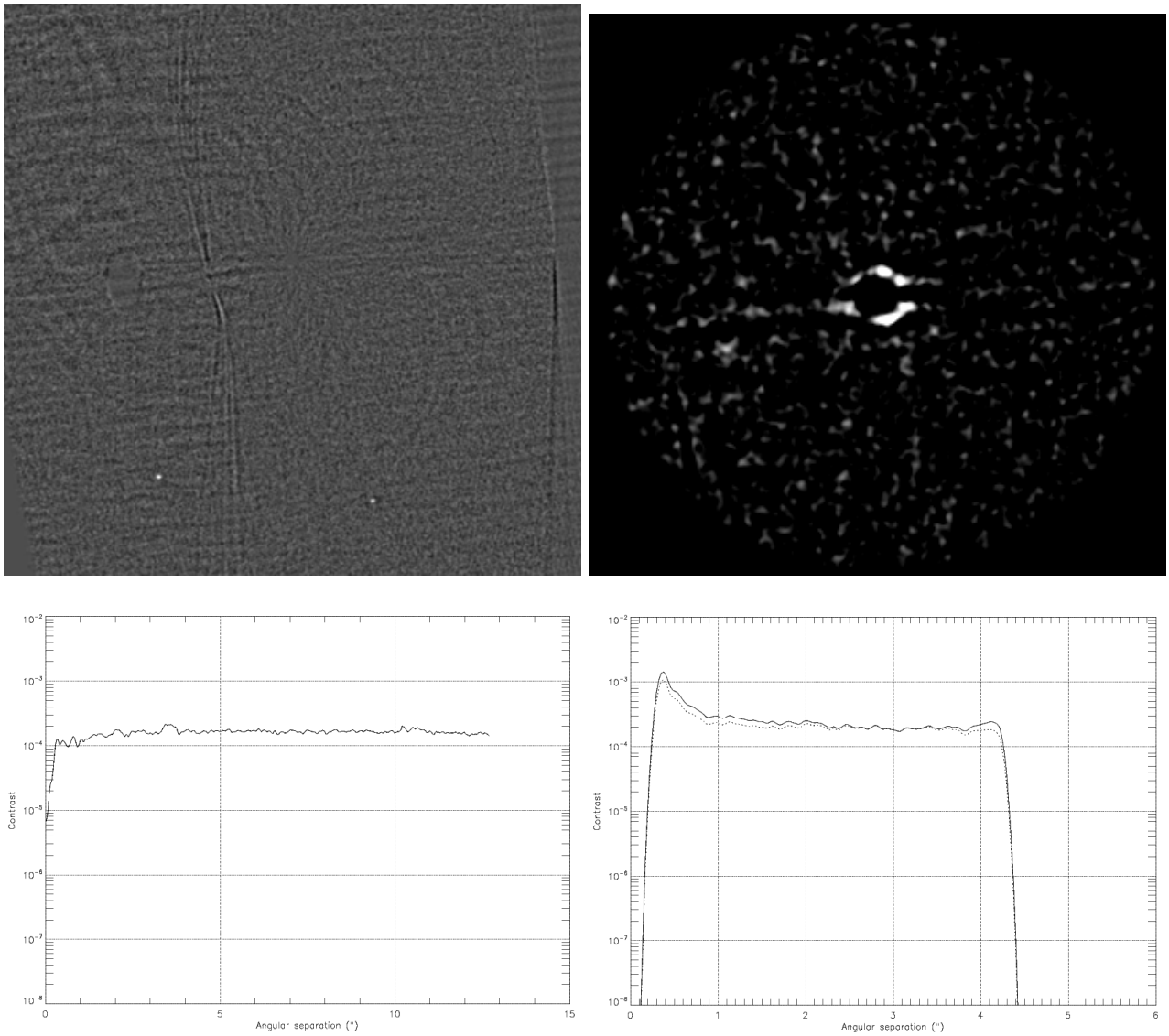

Figure 4.21: HIP 108598. Two candidates are found in the bottom part of ADI image. Nothing for LOCI.

$$n_g = 124 \qquad t_{int,tot} = 744 \text{ s} \qquad \Delta p = 11.5\ ^\circ$$

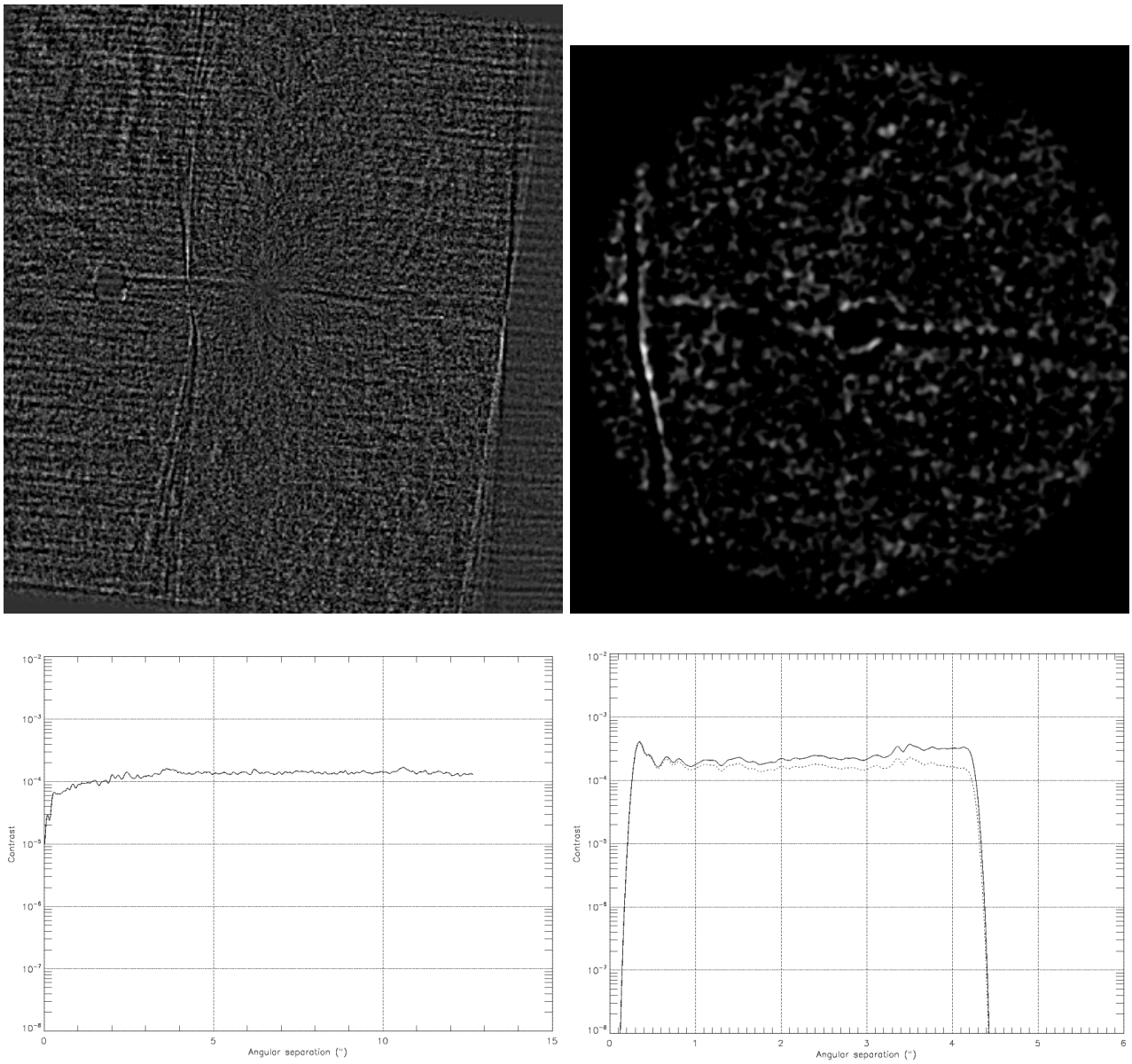

Figure 4.22: TYC-635-90-1. Nothing is found. Again, the small number of frames and parallactic variation contribute to the non detection of candidate.

$$n_g = 45 \qquad t_{int,tot} = 270 \text{ s} \qquad \Delta p = \text{-}6.9\ ^\circ$$

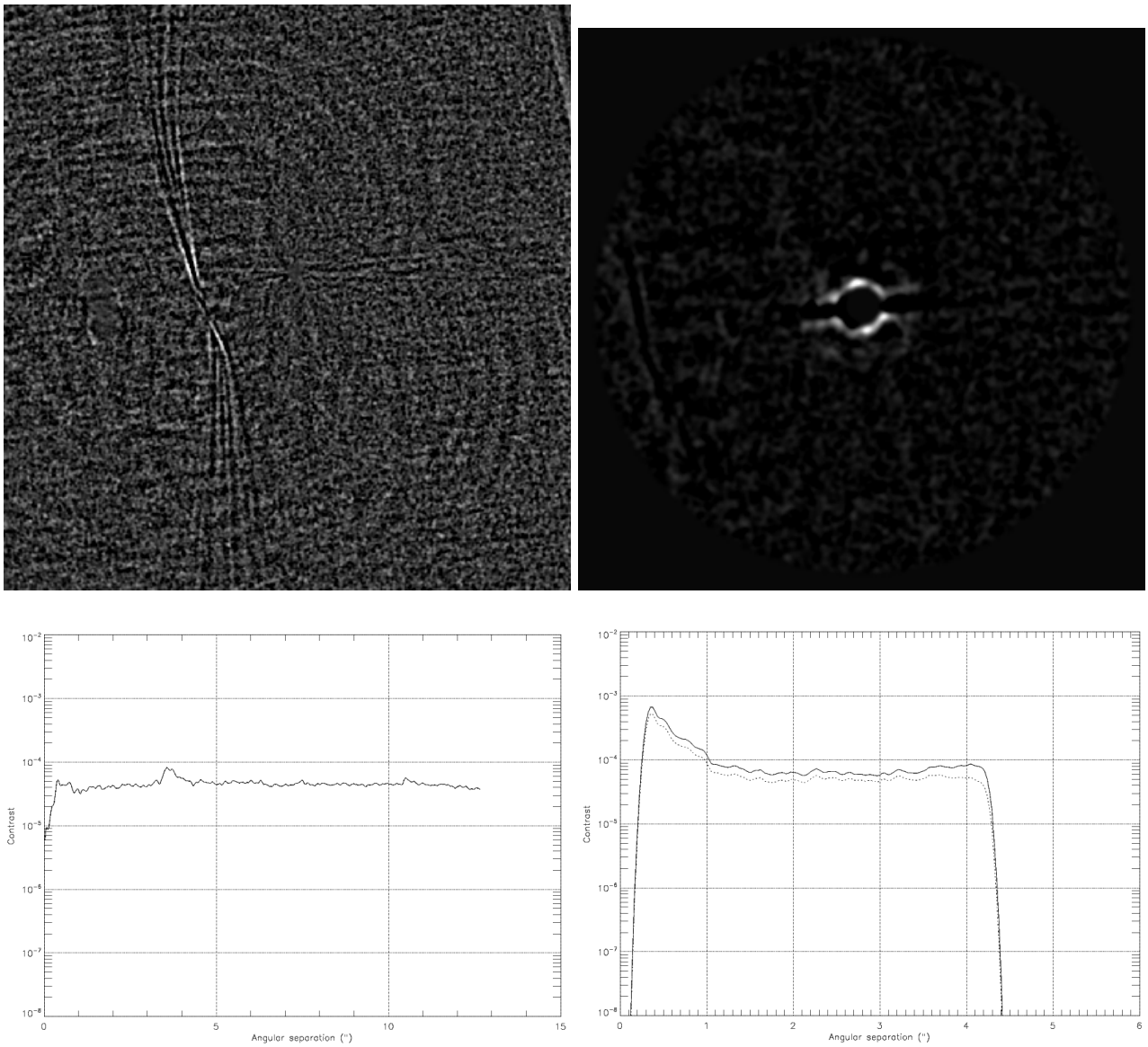

Figure 4.23: HIP 7699. Nothing to declare. Number of frames and parallactic variation are average.

$$n_g = 113 \qquad t_{int,tot} = 678 \text{ s} \qquad \Delta p = 15.4\ ^\circ$$

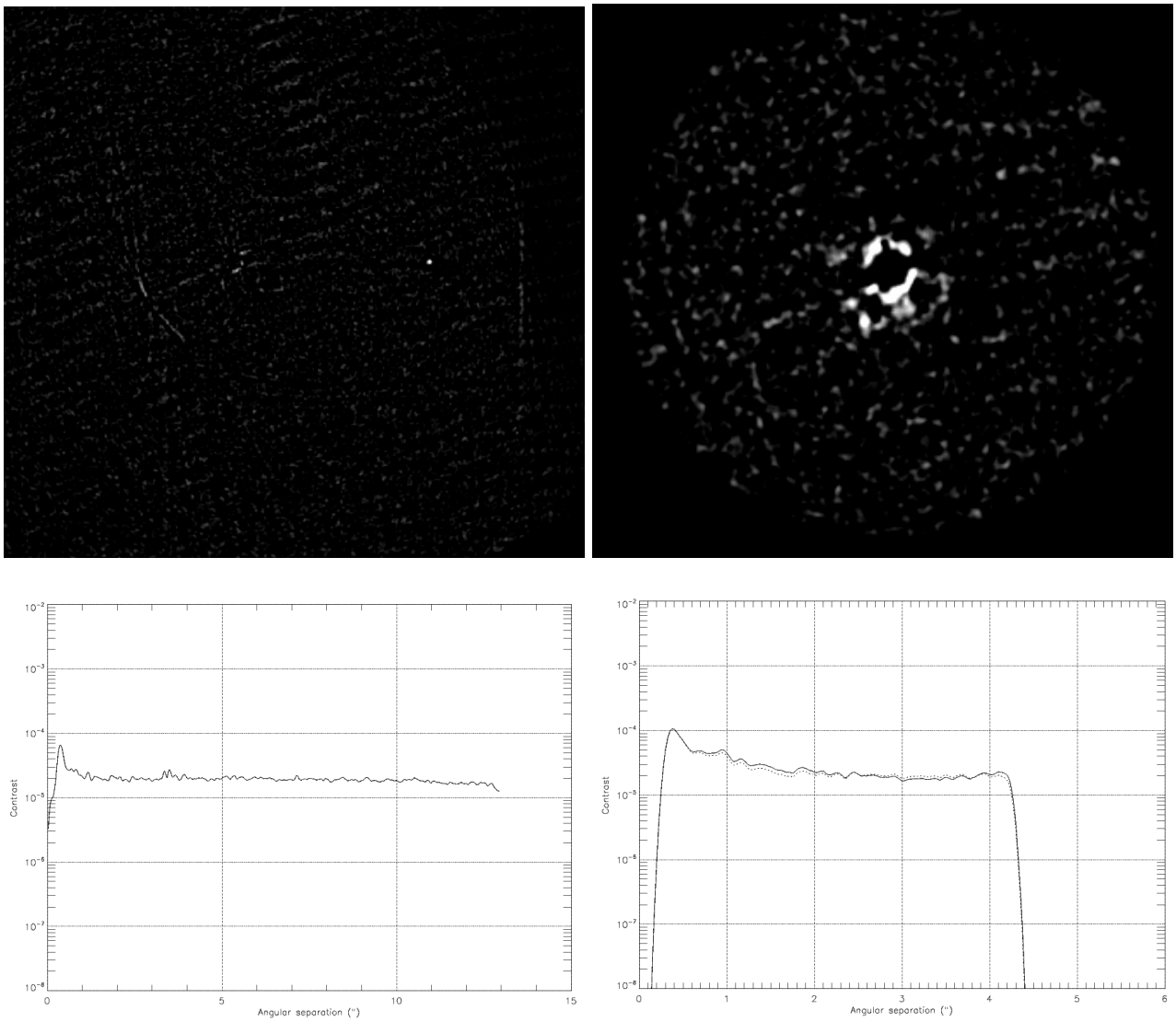

Figure 4.24: HIP 30503. A candidate is found by ADI on the right of the image, albeit the total parallactic variation is small. For LOCI, it is more difficult to decide.

$$n_g = 121 \qquad t_{int,tot} = 726 \text{ s} \qquad \Delta p = 6.0\ ^\circ$$

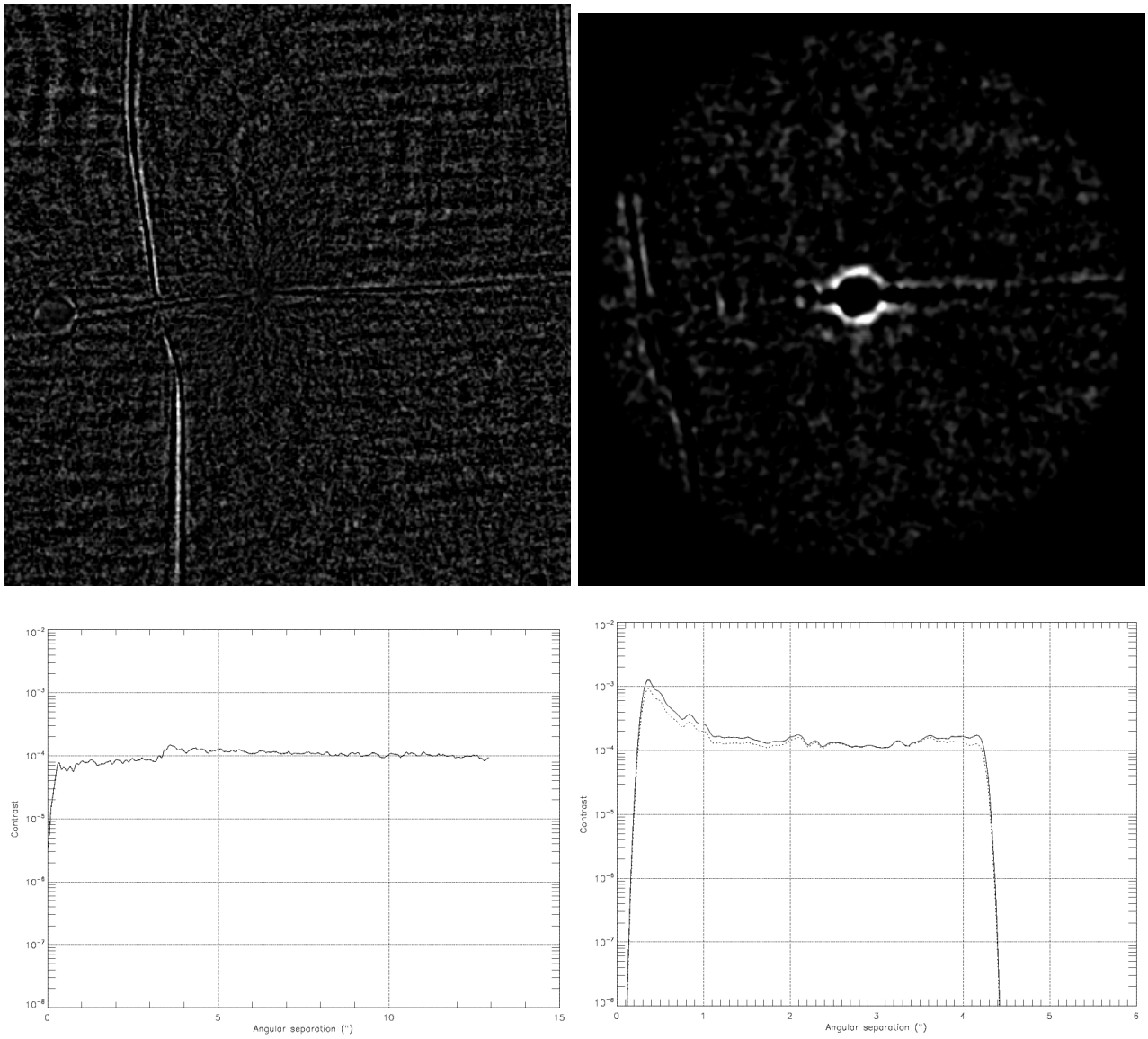

Figure 4.25: HIP 30729. Finally, there is nothing to declare for this last target neither, whose total parallactic variation is also small.

$$n_g = 99 \qquad t_{int,tot} = 594 \text{ s} \qquad \Delta p = 7.3\ ^\circ$$

4.3 Conclusions and suggestions for further investigations

A first common point that can be noted from all the frames (also in the second set) is that the images are all background limited, i.e. they are not limited by the quasi-static speckles (or, so little). This fact results in a very flat contrast curve. It is noticeworthy that all detections made with ADI-data and reduction with LOCI reported in the litterature (see e.g. Marois, Macintosh, et al., 2008; Marois et al., 2010) correspond on the contrary to its application to saturated regimes of speckles. In addition, our observations had globally not enough field rotation/total parallactic angle variation for ADI, only 20° in general, to be compared e.g. to the 54-100° used by (Marois et al., 2006) for its different targets. Our detection limits varied between 10^{-5} and $10^{-2.5}$, they are strongly dependent on this total parallactic variation, but also on the atmosphere conditions and number of frames available.

In total, we have found ~ 5 candidates from our 2 sets of observations, excluding the one that was known from Dimitri to be a background star. However, most are either very far (at about 10" from their star, i.e. if they were bound they would orbit at 200 AU for a star at 20 pc), so that effective chance that they are indeed bound to their star is rather low. This sample of 26 companions led thus to a non-result for giant planets between 5-10 [1] and 200 AU. Nonetheless, this non-result has to be balanced by the fact that our parallactic variation was not often substantial, favoring the detection of candidates at very large angular distance.

Nevertheless, 200 AU is the lengthscale at which the first giant planets/brown dwarfs to be detected were found from their star, so that an astrometric follow-up for the candidates should be performed by caution. Given the proximity of our star sample (<25 pc), a significant proper motion is expected so that a baseline of a few months should be sufficient to confirm companionship. If it was to be proved that some of these candidates are indeed bound to the star, a thorough study in order to determine the age of the star accurately can be endeavored. Knowing the age of the star, its spectral type and measured luminosity, along with the exoplanet or brown dwarf luminosity, enables finally to estimate a mass for this companion through the use of a start model, as mentioned in section 4.1.

Nonetheless, in order to further discriminate their status readily, the use of IDL function `aper.pro` is indicated, as it enables to calculate their signal to noise ratio based on a kernel set by the user, typically to λ/D in pixels. From this signal to noise ratio, it is then possible to derive the confidence level of the specific candidate. This concept could then be pushed even further by the implementation of an algorithm seeking automatically any kernel of size λ/D of level higher than $5 - \sigma/N$, which would have the strong advantage to be much more sensitive than detection at the naked eye, and enable possibly to highlight some other candidates unseen from the naked eye analysis of the images. These features are currently the subject of exploration by the writer as well as the test of our targets with `ADI_s` and `LOCI_s` in order to find signature of the disks.

Finally, a second run of the two targets displaying possible close binaries is necessary: the code will be re-run with the keyword `\centering` in order to have a better idea of their true status (PT drift or close binary).

[1] Assuming the level of the LOCI contrast curve was of order 10^{-4} down to 0.5-1" for targets in good atmospheric conditions.

Conclusions and perspectives

In this work, we summarized the scientific context as well as the different observational tools relevant in the field of high-contrast and high angular resolution imaging of exoplanets, insisting notably on the reduction aspect for ADI-data. Personal contributions to an existing code, upgrading it to a whole-in-one versatile code, were then presented. The idea of injecting fake companions for determining the loss due to LOCI, albeit not original, has been implemented from its very first steps, in an IDL code. The optimization of the different parameters was then attempted, although this part led to a rather disappointing result.

This comprehensive code was then tested on two sets of observations, confirming its viability and allowing us to discover some unknown objects (probably background stars, but possibly physical companions) to be further characterized. Of course, it would have been better to detect more serious candidates. Nevertheless, the global non-result of the search for giant planets on wide orbit around young and close stars surrounded by debris disks constitutes a result in itself. It is an argument in favor of the core accretion model as, from what is observed, giant planet formation seems difficult beyond $\sim$ 5-10 AU from the central star, at least for F-, G- and K-type stars. It is noteworthy that our result is consistent with the statistical bayesian analysis of a dedicated survey of nearby young F-, G- and K-type stars of Lafrenière, Doyon, et al. (2007), which indicated that exoplanets are relatively rare at separations greater than 20 AU. Nonetheless, the $\sim$ 5 candidates found at very large distance should be followed up in order to determine if they are gravitationally bound to the star. With an estimate of the age of the central star, the choice of an evolutionnary model (e.g. Baraffe et al., Burrows et al.) enables to estimate the mass of the companion, and hence assess if it is a giant exoplanet or a brown dwarf. An example of thorough investigation for a serious candidate around T-Tauri star IM Lup is given in (Mawet, Absil, et al., 2012), so that it would contitute an itinerary to follow. In the case of IM Lup, it led alas to the rejection of the bound hypothesis, although many favorable clues had accumulated.

It should be pointed out that successful direct detections of giant planets happened almost exclusively around A stars (e.g. HR8799, β Pic) so far, although their higher stellar luminosity is offering a less favorable planet-to-star contrast. To compensate, the higher-mass A stars have the advantage of being capable of retaining heavier and more extended disks (Mannings & Sargent, 1997) and thus might form massive planets at wide separations, probably with the mechanism of gravitational instability (Dodson-Robinson et al., 2009), making their planets easier to detect. The fact that debris disks are more common around younger A stars (Rieke et al., 2005) is undubitably correlated. In

comparison, debris disks are found around 10% of F-, G- and K-type stars (Trilling et al., 2008), and are rare around M stars (Gautier et al., 2007).

Finally, the global non-result of our small survey should be put together with results from other similar surveys in order to form a statistically significant ensemble before concluding too hastily. This is planned and could be the subject of an upcoming article, which could have a subtantial impact on the current debate between the core accretion and gravitational fragmentation paradigms.

While the contribution of this manuscript appears, all things considered, relatively modest, this work was from a personal point of view extremely rewarding. It allowed me to have a global picture of the wide field which is high-contrast and high angular resolution imaging in the context of exoplanet science, about which my knowledge was relatively limited at the very beginning of this work. I discovered the long process required when carrying observations: choice of an optimal observation strategy, data acquisition, data reduction, scientific interpretation. Finally, for want of being grateful, hours of debugging trained me to an expert level in IDL-language.

Again, I acknowledge sincerely all the people that contributed, directly or indirectly, to my progression in this work.

References

Absil, O., Le Bouquin, J.-B., Berger, J.-P., Lagrange, A.-M., Chauvin, G., Lazareff, B., et al. (2011, November). Searching for faint companions with VLTI/PIONIER. I. Method and first results. A&A, *535*, A68.

Absil, O., & Mawet, D. (2010, July). Formation and evolution of planetary systems: the impact of high-angular resolution optical techniques. A&A Rev., *18*, 317-382.

Absil, O., Mennesson, B., Le Bouquin, J.-B., Di Folco, E., Kervella, P., & Augereau, J.-C. (2009, October). An Interferometric Study of the Fomalhaut Inner Debris Disk. I. Near-Infrared Detection of Hot Dust with VLTI/VINCI. ApJ, *704*, 150-160.

Aime, C., Soummer, R., & Ferrari, A. (2002, July). Total coronagraphic extinction of rectangular apertures using linear prolate apodizations. A&A, *389*, 334-344.

Alexander, R. D., Clarke, C. J., & Pringle, J. E. (2006, June). Photoevaporation of protoplanetary discs - II. Evolutionary models and observable properties. MNRAS, *369*, 229-239.

Alibert, Y., Mordasini, C., & Benz, W. (2004, April). Migration and giant planet formation. A&A, *417*, L25-L28.

Allen, W. H. (2005, July). Serendipitous Discovery of an Eclipsing Binary Star. In C. Sterken (Ed.), *The light-time effect in astrophysics: Causes and cures of the o-c diagram* (Vol. 335, p. 349).

Amara, A., & Quanz, S. (2012, July). PynPoint: An Image Processing Package for Finding Exoplanets. *ArXiv e-prints*.

Andrews, S. M., & Williams, J. P. (2005, October). Circumstellar Dust Disks in Taurus-Auriga: The Submillimeter Perspective. ApJ, *631*, 1134-1160.

Aumann, H. H., Beichman, C. A., Gillett, F. C., de Jong, T., Houck, J. R., Low, F. J., et al. (1984, March). Discovery of a shell around Alpha Lyrae. ApJ, *278*, L23-L27.

Auvergne, M., Bodin, P., Boisnard, L., Buey, J.-T., Chaintreuil, S., Epstein, G., et al. (2009, October). The CoRoT satellite in flight: description and performance. A&A, *506*, 411-424.

Backman, D. E., & Paresce, F. (1993). Main-sequence stars with circumstellar solid material - The VEGA phenomenon. In E. H. Levy & J. I. Lunine (Eds.), *Protostars and planets iii* (p. 1253-1304).

Baraffe, I., Chabrier, G., Allard, F., & Hauschildt, P. H. (1998, September). Evolutionary models for solar metallicity low-mass stars: mass-magnitude relationships and color-magnitude diagrams. A&A, *337*, 403-412.

Baraffe, I., Chabrier, G., Allard, F., & Hauschildt, P. H. (2002, February). Evolutionary models for low-mass stars and brown dwarfs: Uncertainties and limits at very young ages. A&A, *382*, 563-572.

Baraffe, I., Chabrier, G., Barman, T. S., Allard, F., & Hauschildt, P. H. (2003, May). Evolutionary models for cool brown dwarfs and extrasolar giant planets. The case of HD 209458. A&A, *402*, 701-712.

Baranne, A., Queloz, D., Mayor, M., Adrianzyk, G., Knispel, G., Kohler, D., et al. (1996, October). ELODIE: A spectrograph for accurate radial velocity measurements. A&AS, *119*, 373-390.

Batalha, N. M., Borucki, W. J., Bryson, S. T., Buchhave, L. A., Caldwell, D. A., Christensen-Dalsgaard, J., et al. (2011, March). Kepler's First Rocky Planet: Kepler-10b. ApJ, *729*, 27.

Baudoz, P., Rabbia, Y., & Gay, J. (2000, January). Achromatic interfero coronagraphy I. Theoretical capabilities for ground-based observations. A&AS, *141*, 319-329.

Bean, J. L., Seifahrt, A., Hartman, H., Nilsson, H., Reiners, A., Dreizler, S., et al. (2009, December). The CRIRES Search for Planets Around the Lowest-Mass Stars. II. The Proposed Giant Planet Orbiting VB10 Does Not Exist. *ArXiv e-prints*.

Beichman, C. A., Woolf, N. J., & Lindensmith, C. A. (1999). *The Terrestrial Planet Finder (TPF) : a NASA Origins Program to search for habitable planets*.

Benedict, G. F., McArthur, B. E., Forveille, T., Delfosse, X., Nelan, E., Butler, R. P., et al. (2002, December). A Mass for the Extrasolar Planet Gliese 876b Determined from Hubble Space Telescope Fine Guidance Sensor 3 Astrometry and High-Precision Radial Velocities. ApJ, *581*, L115-L118.

Beust, H. (2003, March). Symplectic integration of hierarchical stellar systems. A&A, *400*, 1129-1144.

Beust, H. (2006, March). Modélisation des disques de débris. *Ecole de Goutelas*, *28*, 155-189.

Beust, H. (2010, January). Dynamical Processes in Debris Disks. In T. Montmerle, D. Ehrenreich, & A.-M. Lagrange (Eds.), *Eas publications series* (Vol. 41, p. 219-230).

Beuzit, J.-L., Hubin, N., Gendron, E., Demailly, L., Gigan, P., Lacombe, F., et al. (1994, May). ADONIS: a user-friendly adaptive optics system for the ESO 3.6-m telescope. In M. A. Ealey & F. Merkle (Eds.), *Society of photo-optical instrumentation engineers (spie) conference series* (Vol. 2201, p. 955-961).

Birnstiel, T., Ormel, C. W., & Dullemond, C. P. (2011, January). Dust size distributions in coagulation/fragmentation equilibrium: numerical solutions and analytical fits. A&A, *525*, A11.

Blanc, A., Fusco, T., Hartung, M., Mugnier, L. M., & Rousset, G. (2003, February). Calibration of NAOS and CONICA static aberrations. Application of the phase diversity technique. A&A, *399*, 373-383.

Boccaletti, A., Augereau, J.-C., Lagrange, A.-M., Milli, J., Baudoz, P., Mawet, D., et al. (2012, August). Morphology of the very inclined debris disk around HD 32297. A&A, *544*, A85.

Boley, A. C. (2009, April). The Two Modes of Gas Giant Planet Formation. ApJ, *695*, L53-L57.

Boley, A. C., Payne, M. J., Corder, S., Dent, W. R. F., Ford, E. B., & Shabram, M. (2012, May). Constraining the Planetary System of Fomalhaut Using High-resolution ALMA Observations. ApJ, *750*, L21.

Bonnet, H., Ströbele, S., Biancat-Marchet, F., Brynnel, J., Conzelmann, R. D., Delabre, B., et al. (2003, February). Implementation of MACAO for SINFONI at the VLT, in NGS and LGS modes. In P. L. Wizinowich & D. Bonaccini (Eds.), *Society of photo-optical instrumentation engineers (spie) conference series* (Vol. 4839, p. 329-343).

Borucki, W., Koch, D., Boss, A., Dunham, E., Dupree, A., Geary, J., et al. (2004, January). The

Kepler mission: a technical overview. In F. Favata, S. Aigrain, & A. Wilson (Eds.), *Stellar structure and habitable planet finding* (Vol. 538, p. 177-182).

Borucki, W. J., Koch, D., Jenkins, J., Sasselov, D., Gilliland, R., Batalha, N., et al. (2009, August). Kepler's Optical Phase Curve of the Exoplanet HAT-P-7b. *Science*, *325*, 709-.

Boss, A. P. (1997). Giant planet formation by gravitational instability. *Science*, *276*, 1836-1839.

Boss, A. P. (2000, June). Possible Rapid Gas Giant Planet Formation in the Solar Nebula and Other Protoplanetary Disks. ApJ, *536*, L101-L104.

Bouchy, F., Pepe, F., & Queloz, D. (2001, August). Fundamental photon noise limit to radial velocity measurements. A&A, *374*, 733-739.

Bowler, B. P., Liu, M. C., Dupuy, T. J., & Cushing, M. C. (2010, November). Near-infrared Spectroscopy of the Extrasolar Planet HR 8799 b. ApJ, *723*, 850-868.

Bracewell, R. N., & MacPhie, R. H. (1979, April). Searching for nonsolar planets. Icarus, *38*, 136-147.

Buenzli, E., Thalmann, C., Vigan, A., Boccaletti, A., Chauvin, G., Augereau, J. C., et al. (2010, December). Dissecting the Moth: discovery of an off-centered ring in the HD 61005 debris disk with high-resolution imaging. A&A, *524*, L1.

Burke, D., & Devaney, N. (2010, September). Enhanced faint companion photometry and astrometry using wavelength diversity. *Journal of the Optical Society of America A*, *27*(26), A260000.

Burrows, A., Hubbard, W. B., Lunine, J. I., & Liebert, J. (2001, July). The theory of brown dwarfs and extrasolar giant planets. *Reviews of Modern Physics*, *73*, 719-765.

Burrows, A., Hubbard, W. B., Saumon, D., & Lunine, J. I. (1993, March). An expanded set of brown dwarf and very low mass star models. ApJ, *406*, 158-171.

Cameron, A. G. W. (1973, March). Accumulation processes in the primitive solar nebula. Icarus, *18*, 407-450.

Carreras, R. A., Restaino, S. R., & Duneman, D. C. (1994, September). Laboratory experiment using phase diversity to extract higher order Zernike coefficients. In T. J. Schulz & D. L. Snyder (Eds.), *Society of photo-optical instrumentation engineers (spie) conference series* (Vol. 2302, p. 323-329).

Cassan, A., Kubas, D., Beaulieu, J.-P., Dominik, M., Horne, K., Greenhill, J., et al. (2012, January). One or more bound planets per Milky Way star from microlensing observations. Nature, *481*, 167-169.

Chabrier, G., Baraffe, I., Allard, F., & Hauschildt, P. (2000, October). Evolutionary Models for Very Low-Mass Stars and Brown Dwarfs with Dusty Atmospheres. ApJ, *542*, 464-472.

Charbonneau, D., Brown, T. M., Latham, D. W., & Mayor, M. (2000, January). Detection of Planetary Transits Across a Sun-like Star. ApJ, *529*, L45-L48.

Chauvin, G., Lagrange, A.-M., Dumas, C., Zuckerman, B., Mouillet, D., Song, I., et al. (2005, August). Giant planet companion to 2MASSW J1207334-393254. A&A, *438*, L25-L28.

Chiang, E., & Murray-Clay, R. (2007, September). Inside-out evacuation of transitional protoplanetary discs by the magneto-rotational instability. *Nature Physics*, *3*, 604-608.

Christiaens, V. (2012). *Internship report at ESO: Optimization of the VLT/NaCo alignment procedure to reduce the non-common path errors* (Tech. Rep.). University of Liège & ESO.

Clarke, C. J., Gendrin, A., & Sotomayor, M. (2001, December). The dispersal of circumstellar discs: the role of the ultraviolet switch. MNRAS, *328*, 485-491.

Codona, J. L., Kenworthy, M. A., Hinz, P. M., Angel, J. R. P., & Woolf, N. J. (2006, July). A

high-contrast coronagraph for the MMT using phase apodization: design and observations at 5 microns and 2 λ/D radius. In *Society of photo-optical instrumentation engineers (spie) conference series* (Vol. 6269).

Crepp, J. R., Pueyo, L., Brenner, D., Oppenheimer, B. R., Zimmerman, N., Hinkley, S., et al. (2011, March). Speckle Suppression with the Project 1640 Integral Field Spectrograph. ApJ, *729*, 132.

Currie, T., Rodigas, T. J., Debes, J., Plavchan, P., Kuchner, M., Jang-Condell, H., et al. (2012, June). Keck/NIRC2 Imaging of the Warped, Asymmetric Debris Disk around HD 32297. *ArXiv e-prints*.

Deeg, H. J., Doyle, L. R., Kozhevnikov, V. P., Blue, J. E., Martín, E. L., & Schneider, J. (2000, June). A search for Jovian-mass planets around CM Draconis using eclipse minima timing. A&A, *358*, L5-L8.

Dodson-Robinson, S. E., Veras, D., Ford, E. B., & Beichman, C. A. (2009, December). The Formation Mechanism of Gas Giants on Wide Orbits. ApJ, *707*, 79-88.

Dominik, C., & Decin, G. (2003, November). Age Dependence of the Vega Phenomenon: Theory. ApJ, *598*, 626-635.

Dong, S., DePoy, D. L., Gaudi, B. S., Gould, A., Han, C., Park, B.-G., et al. (2006, May). Planetary Detection Efficiency of the Magnification 3000 Microlensing Event OGLE-2004-BLG-343. ApJ, *642*, 842-860.

Drake, A. J. (2003, June). On the Selection of Photometric Planetary Transits. ApJ, *589*, 1020-1026.

Dullemond, C. P., & Dominik, C. (2005, May). Dust coagulation in protoplanetary disks: A rapid depletion of small grains. A&A, *434*, 971-986.

Esposito, S., Riccardi, A., Pinna, E., Puglisi, A., Quirós-Pacheco, F., Arcidiacono, C., et al. (2011, September). Large Binocular Telescope Adaptive Optics System: new achievements and perspectives in adaptive optics. In *Society of photo-optical instrumentation engineers (spie) conference series* (Vol. 8149).

Fitzgerald, M. P., & Graham, J. R. (2006, January). Speckle Statistics in Adaptively Corrected Images. ApJ, *637*, 541-547.

Fortney, J. J., Marley, M. S., Saumon, D., & Lodders, K. (2008, August). Synthetic Spectra and Colors of Young Giant Planet Atmospheres: Effects of Initial Conditions and Atmospheric Metallicity. ApJ, *683*, 1104-1116.

Freistetter, F., Krivov, A. V., & Löhne, T. (2007, April). Planets of β Pictoris revisited. A&A, *466*, 389-393.

Fressin, F., Torres, G., Rowe, J. F., Charbonneau, D., Rogers, L. A., Ballard, S., et al. (2012, February). Two Earth-sized planets orbiting Kepler-20. Nature, *482*, 195-198.

Fried, D. L. (1966, October). Optical Resolution Through a Randomly Inhomogeneous Medium for Very Long and Very Short Exposures. *Journal of the Optical Society of America (1917-1983)*, *56*, 1372.

Fusco, T., Petit, C., Rousset, G., Sauvage, J.-F., Dohlen, K., Mouillet, D., et al. (2006, July). Design of the extreme AO system for SPHERE, the planet finder instrument of the VLT. In *Society of photo-optical instrumentation engineers (spie) conference series* (Vol. 6272).

G. Rauw. (2010-2011). Cours d'etoiles variables [Computer software manual].

Gautier, T. N., III, Rieke, G. H., Stansberry, J., Bryden, G. C., Stapelfeldt, K. R., Werner, M. W., et al. (2007, September). Far-Infrared Properties of M Dwarfs. ApJ, *667*, 527-536.

Girard, J. (2011, June). Very Large Telescope NaCo User Manual [Computer software manual]. Karl-Schwarzschild-Str.2, 85748 Garching bei Munchen, Germany.

Gladysz, S., Yaitskova, N., & Christou, J. C. (2010, November). Statistics of intensity in adaptive-optics images and their usefulness for detection and photometry of exoplanets. *Journal of the Optical Society of America A*, *27*(26), A260000-A75.

Gosset, E. (2011-2012). Cours d'analyse de séries temporelles [Computer software manual].

Greenwood, D. P. (1977, March). Bandwidth specification for adaptive optics systems. *Journal of the Optical Society of America (1917-1983)*, *67*, 390-393.

Gullbring, E., Hartmann, L., Briceno, C., & Calvet, N. (1998, January). Disk Accretion Rates for T Tauri Stars. ApJ, *492*, 323.

Guyon, O. (2003, June). Phase-induced amplitude apodization of telescope pupils for extrasolar terrestrial planet imaging. A&A, *404*, 379-387.

Guyon, O., Pluzhnik, E. A., Galicher, R., Martinache, F., Ridgway, S. T., & Woodruff, R. A. (2005, March). Exoplanet Imaging with a Phase-induced Amplitude Apodization Coronagraph. I. Principle. ApJ, *622*, 744-758.

Guyon, O., Roddier, C., Graves, J. E., Roddier, F., Cuevas, S., Espejo, C., et al. (1999, October). The Nulling Stellar Coronagraph: Laboratory Tests and Performance Evaluation. PASP, *111*, 1321-1330.

Haisch, K. E., Jr., Lada, E. A., & Lada, C. J. (2001, June). Disk Frequencies and Lifetimes in Young Clusters. ApJ, *553*, L153-L156.

Hartmann, J. (1900, June). Remarks on the Construction and Adjustment of Spectrographs. I. ApJ, *11*, 400.

Hartmann, L., Ballesteros-Paredes, J., & Bergin, E. A. (2001, December). Rapid Formation of Molecular Clouds and Stars in the Solar Neighborhood. ApJ, *562*, 852-868.

Hartung, M., Blanc, A., Fusco, T., Lacombe, F., Mugnier, L. M., Rousset, G., et al. (2003, February). Calibration of NAOS and CONICA static aberrations. Experimental results. A&A, *399*, 385-394.

Heap, S. R., Lindler, D. J., Lanz, T. M., Cornett, R. H., Hubeny, I., Maran, S. P., et al. (2000, August). Space Telescope Imaging Spectrograph Coronagraphic Observations of β Pictoris. ApJ, *539*, 435-444.

Herriot, G., & Morris, S. (1997, March). Gemini Adaptive Optics System. In A. L. Ardeberg (Ed.), *Society of photo-optical instrumentation engineers (spie) conference series* (Vol. 2871, p. 816-826).

Hinkley, S., Oppenheimer, B. R., Soummer, R., Sivaramakrishnan, A., Roberts, L. C., Jr., Kuhn, J., et al. (2007, January). Temporal Evolution of Coronagraphic Dynamic Range and Constraints on Companions to Vega. ApJ, *654*, 633-640.

Huygens, C. (1698). *The celestial worlds discover'd:*.

Ida, S., & Lin, D. N. C. (2004, March). Toward a Deterministic Model of Planetary Formation. I. A Desert in the Mass and Semimajor Axis Distributions of Extrasolar Planets. ApJ, *604*, 388-413.

Janson, M., Bergfors, C., Goto, M., Brandner, W., & Lafrenière, D. (2010, February). Spatially Resolved Spectroscopy of the Exoplanet HR 8799 c. ApJ, *710*, L35-L38.

Janson, M., Carson, J. C., Lafrenière, D., Spiegel, D. S., Bent, J. R., & Wong, P. (2012, March). Infrared Non-detection of Fomalhaut b: Implications for the Planet Interpretation. ApJ, *747*,

116.

Jorissen, A., Mayor, M., & Udry, S. (2001, December). The distribution of exoplanet masses. A&A, *379*, 992-998.

Kalas, P., Graham, J. R., Chiang, E., Fitzgerald, M. P., Clampin, M., Kite, E. S., et al. (2008, November). Optical Images of an Exosolar Planet 25 Light-Years from Earth. *Science*, *322*, 1345-.

Kalas, P., Graham, J. R., & Clampin, M. (2005, June). A planetary system as the origin of structure in Fomalhaut's dust belt. Nature, *435*, 1067-1070.

Kendrick, R. L., Acton, D. S., & Duncan, A. L. (1994, September). Phase-diversity wave-front sensor for imaging systems. Appl. Opt., *33*, 6533-6546.

Kern, P., Lena, P., Gigan, P., Fontanella, J.-C., & Rousset, G. (1989, September). COME-ON - an adaptive optics prototype dedicated to infrared astronomy. In F. J. Roddier (Ed.), *Society of photo-optical instrumentation engineers (spie) conference series* (Vol. 1114, p. 54-64).

Koerner, D. W., Kim, S., Trilling, D. E., Larson, H., Cotera, A., Stapelfeldt, K. R., et al. (2010, February). New Debris Disk Candidates Around 49 Nearby Stars. ApJ, *710*, L26-L29.

Kuhn, J. R., Potter, D., & Parise, B. (2001, June). Imaging Polarimetric Observations of a New Circumstellar Disk System. ApJ, *553*, L189-L191.

Labeyrie, A. (1995, June). Images of exo-planets obtainable from dark speckles in adaptive telescopes. A&A, *298*, 544.

Lafrenière, D., Doyon, R., Marois, C., Nadeau, D., Oppenheimer, B. R., Roche, P. F., et al. (2007, December). The Gemini Deep Planet Survey. ApJ, *670*, 1367-1390.

Lafrenière, D., Jayawardhana, R., & van Kerkwijk, M. H. (2008, December). Direct Imaging and Spectroscopy of a Planetary-Mass Candidate Companion to a Young Solar Analog. ApJ, *689*, L153-L156.

Lafrenière, D., Jayawardhana, R., & van Kerkwijk, M. H. (2010, August). The Directly Imaged Planet Around the Young Solar Analog 1RXS J160929.1 - 210524: Confirmation of Common Proper Motion, Temperature, and Mass. ApJ, *719*, 497-504.

Lafrenière, D., Marois, C., Doyon, R., Nadeau, D., & Artigau, É. (2007, May). A New Algorithm for Point-Spread Function Subtraction in High-Contrast Imaging: A Demonstration with Angular Differential Imaging. ApJ, *660*, 770-780.

Lagrange, A.-M., Boccaletti, A., Milli, J., Chauvin, G., Bonnefoy, M., Mouillet, D., et al. (2012, June). The position of β Pictoris b position relative to the debris disk. A&A, *542*, A40.

Lagrange, A.-M., Bonnefoy, M., Chauvin, G., Apai, D., Ehrenreich, D., Boccaletti, A., et al. (2010, July). A Giant Planet Imaged in the Disk of the Young Star β Pictoris. *Science*, *329*, 57-.

Lagrange, A.-M., Gratadour, D., Chauvin, G., Fusco, T., Ehrenreich, D., Mouillet, D., et al. (2009, January). A probable giant planet imaged in the β Pictoris disk. VLT/NaCo deep L'-band imaging. A&A, *493*, L21-L25.

Lenzen, R., Close, L., Brandner, W., Biller, B., & Hartung, M. (2004, September). A novel simultaneous differential imager for the direct imaging of giant planets. In A. F. M. Moorwood & M. Iye (Eds.), *Society of photo-optical instrumentation engineers (spie) conference series* (Vol. 5492, p. 970-977).

Lissauer, J. J. (1993). Planet formation. ARA&A, *31*, 129-174.

Lodders, K. (2003, July). Solar System Abundances and Condensation Temperatures of the Elements.

ApJ, *591*, 1220-1247.

Lyot. (1930). La couronne solaire étudiée en dehors des éclipses. *Bulletin Astronomique*, *6*, 305-316.

Macintosh, B., Poyneer, L., Sivaramakrishnan, A., & Marois, C. (2005, August). Speckle lifetimes in high-contrast adaptive optics. In R. K. Tyson & M. Lloyd-Hart (Eds.), *Society of photo-optical instrumentation engineers (spie) conference series* (Vol. 5903, p. 170-177).

Mahajan, V. N. (1981). Zernike annular polynomials for imaging systems with annular pupils. *Journal of the Optical Society of America (1917-1983)*, *71*, 75-85.

Mamajek, E. E. (2009, August). Initial Conditions of Planet Formation: Lifetimes of Primordial Disks. In T. Usuda, M. Tamura, & M. Ishii (Eds.), *American institute of physics conference series* (Vol. 1158, p. 3-10).

Mandushev, G., Torres, G., Latham, D. W., Charbonneau, D., Alonso, R., White, R. J., et al. (2005, March). The Challenge of Wide-Field Transit Surveys: The Case of GSC 01944-02289. ApJ, *621*, 1061-1071.

Mannings, V., & Sargent, A. I. (1997, December). A High-Resolution Study of Gas and Dust around Young Intermediate-Mass Stars: Evidence for Circumstellar Disks in Herbig AE Systems. ApJ, *490*, 792.

Mao, S., & Paczynski, B. (1991, June). Gravitational microlensing by double stars and planetary systems. ApJ, *374*, L37-L40.

Marcy, G. W., Butler, R. P., Vogt, S. S., Liu, M. C., Laughlin, G., Apps, K., et al. (2001, July). Two Substellar Companions Orbiting HD 168443. ApJ, *555*, 418-425.

Marechal, Y., Coulomb, J. L., Meunier, G., & Touzot, G. (1994, September). Use of the diffuse approximation method for electromagnetic field computation. *IEEE Transactions on Magnetics*, *30*, 3558-3561.

Marley, M. S., Saumon, D., Cushing, M., Ackerman, A. S., Fortney, J. J., & Freedman, R. (2012, August). Masses, Radii, and Cloud Properties of the HR 8799 Planets. ApJ, *754*, 135.

Marois, C., Doyon, R., Nadeau, D., Racine, R., Riopel, M., Vallée, P., et al. (2005, July). TRIDENT: An Infrared Differential Imaging Camera Optimized for the Detection of Methanated Substellar Companions. PASP, *117*, 745-756.

Marois, C., Doyon, R., Racine, R., & Nadeau, D. (2000, January). Efficient Speckle Noise Attenuation in Faint Companion Imaging. PASP, *112*, 91-96.

Marois, C., Lafrenière, D., Doyon, R., Macintosh, B., & Nadeau, D. (2006, April). Angular Differential Imaging: A Powerful High-Contrast Imaging Technique. ApJ, *641*, 556-564.

Marois, C., Lafrenière, D., Macintosh, B., & Doyon, R. (2008, January). Confidence Level and Sensitivity Limits in High-Contrast Imaging. ApJ, *673*, 647-656.

Marois, C., Macintosh, B., Barman, T., Zuckerman, B., Song, I., Patience, J., et al. (2008, November). Direct Imaging of Multiple Planets Orbiting the Star HR 8799. *Science*, *322*, 1348-.

Marois, C., Zuckerman, B., Konopacky, Q. M., Macintosh, B., & Barman, T. (2010, December). Images of a fourth planet orbiting HR 8799. Nature, *468*, 1080-1083.

Mawet, D., Absil, O., Montagnier, G., Riaud, P., Surdej, J., Ducourant, C., et al. (2012, July). Direct imaging of extra-solar planets in star forming regions: Lessons learned from a false positive around IM Lup. *ArXiv e-prints*.

Mawet, D., Mennesson, B., Serabyn, E., Stapelfeldt, K., & Absil, O. (2011, September). A Dim Candidate Companion to epsilon Cephei. ApJ, *738*, L12.

Mawet, D., Pueyo, L., Lawson, P., Mugnier, L., Traub, W., Boccaletti, A., et al. (2012, July). Review of small-angle coronagraphic techniques in the wake of ground-based second-generation adaptive optics systems. *ArXiv e-prints*.

Mawet, D., Riaud, P., Absil, O., & Surdej, J. (2005, November). Annular Groove Phase Mask Coronagraph. ApJ, *633*, 1191-1200.

Mawet, D., Serabyn, E., Liewer, K., Burruss, R., Hickey, J., & Shemo, D. (2010, January). The Vector Vortex Coronagraph: Laboratory Results and First Light at Palomar Observatory. ApJ, *709*, 53-57.

Mayor, M., & Queloz, D. (1995, November). A Jupiter-mass companion to a solar-type star. Nature, *378*, 355-359.

Mayor, M., Udry, S., Naef, D., Pepe, F., Queloz, D., Santos, N. C., et al. (2004, February). The CORALIE survey for southern extra-solar planets. XII. Orbital solutions for 16 extra-solar planets discovered with CORALIE. A&A, *415*, 391-402.

McCaughrean, M. J., & O'dell, C. R. (1996, May). Direct Imaging of Circumstellar Disks in the Orion Nebula. AJ, *111*, 1977.

McElwain, M. W., Metchev, S. A., Larkin, J. E., Barczys, M., Iserlohe, C., Krabbe, A., et al. (2007, February). First High-Contrast Science with an Integral Field Spectrograph: The Substellar Companion to GQ Lupi. ApJ, *656*, 505-514.

Mennesson, B., & Mariotti, J. M. (1997, July). Array Configurations for a Space Infrared Nulling Interferometer Dedicated to the Search for Earthlike Extrasolar Planets. Icarus, *128*, 202-212.

Milli, J., Mouillet, D., Lagrange, A. M., Boccaletti, A., Mawet, D., Chauvin, G., et al. (2012, July). Impact of angular differential imaging on circumstellar disk images. *ArXiv e-prints*.

Monnier, J. D. (2003). Astrophysics with Closure Phases. In G. Perrin & F. Malbet (Eds.), *Eas publications series* (Vol. 6, p. 213).

Mouillet, D., Lagrange, A. M., Beuzit, J.-L., Moutou, C., Saisse, M., Ferrari, M., et al. (2004, December). High Contrast Imaging from the Ground: VLT/Planet Finder. In J. Beaulieu, A. Lecavelier Des Etangs, & C. Terquem (Eds.), *Extrasolar planets: Today and tomorrow* (Vol. 321, p. 39).

Mugnier, L. M., Cornia, A., Sauvage, J.-F., Rousset, G., Fusco, T., & Védrenne, N. (2009, May). Optimal method for exoplanet detection by angular differential imaging. *Journal of the Optical Society of America A*, *26*, 1326.

Nakagawa, Y., Nakazawa, K., & Hayashi, C. (1981, March). Growth and sedimentation of dust grains in the primordial solar nebula. Icarus, *45*, 517-528.

Nelder & Mead. (1965). Downhill simplex method. *Computer Journal*, *Vol 7*, 308-313.

Nelson, R. P., & Papaloizou, J. C. B. (2003, March). The interaction of a giant planet with a disc with MHD turbulence - II. The interaction of the planet with the disc. MNRAS, *339*, 993-1005.

Nero, D. J. (2010). *Radiative cooling in disks and its effects on the formation of giant planets via the gravitational instability.* Unpublished doctoral dissertation, The University of Toledo.

Nichols, J. D. (2011, July). Magnetosphere-ionosphere coupling at Jupiter-like exoplanets with internal plasma sources: implications for detectability of auroral radio emissions. MNRAS, *414*, 2125-2138.

Noll, R. J. (1976, March). Zernike polynomials and atmospheric turbulence. *Journal of the Optical Society of America (1917-1983)*, *66*, 207-211.

Obukhov, A. M. (1959). Description of Turbulence in Terms of Lagrangian Variables. *Advances in*

Geophysics, *6*, 113.

O'dell, C. R., Wen, Z., & Hu, X. (1993, June). Discovery of new objects in the Orion nebula on HST images - Shocks, compact sources, and protoplanetary disks. ApJ, *410*, 696-700.

Paczynski, B. (1996). Gravitational Microlensing in the Local Group. ARA&A, *34*, 419-460.

Papaloizou, J. C. B., & Terquem, C. (1999, August). Critical Protoplanetary Core Masses in Protoplanetary Disks and the Formation of Short-Period Giant Planets. ApJ, *521*, 823-838.

Pascucci, I., Gorti, U., Hollenbach, D., Najita, J., Meyer, M. R., Carpenter, J. M., et al. (2006, November). Formation and Evolution of Planetary Systems: Upper Limits to the Gas Mass in Disks around Sun-like Stars. ApJ, *651*, 1177-1193.

Patience, J., King, R. R., de Rosa, R. J., & Marois, C. (2010, July). The highest resolution near infrared spectrum of the imaged planetary mass companion 2M1207 b. A&A, *517*, A76.

Pepe, F., Mayor, M., Galland, F., Naef, D., Queloz, D., Santos, N. C., et al. (2002, June). The CORALIE survey for southern extra-solar planets VII. Two short-period Saturnian companions to ¡ASTROBJ¿HD 108147¡/ASTROBJ¿ and ¡ASTROBJ¿HD 168746¡/ASTROBJ¿. A&A, *388*, 632-638.

Perri, F., & Cameron, A. G. W. (1974, August). Hydrodynamic instability of the solar nebula in the presence of a planetary core. Icarus, *22*, 416-425.

Plavchan, P., Werner, M. W., Chen, C. H., Stapelfeldt, K. R., Su, K. Y. L., Stauffer, J. R., et al. (2009, June). New Debris Disks Around Young, Low-Mass Stars Discovered with the Spitzer Space Telescope. ApJ, *698*, 1068-1094.

Pollack, J. B., Hubickyj, O., Bodenheimer, P., Lissauer, J. J., Podolak, M., & Greenzweig, Y. (1996, November). Formation of the Giant Planets by Concurrent Accretion of Solids and Gas. Icarus, *124*, 62-85.

Pont, F., Melo, C. H. F., Bouchy, F., Udry, S., Queloz, D., Mayor, M., et al. (2005, April). A planet-sized transiting star around OGLE-TR-122. Accurate mass and radius near the hydrogen-burning limit. A&A, *433*, L21-L24.

Pont, F., Moutou, C., Bouchy, F., Behrend, R., Mayor, M., Udry, S., et al. (2006, March). Radius and mass of a transiting M dwarf near the hydrogen-burning limit. OGLE-TR-123. A&A, *447*, 1035-1039.

Poynting, J. H. (1904). Radiation in the Solar System: Its Effect on Temperature and Its Pressure on Small Bodies. *Royal Society of London Philosophical Transactions Series A*, *202*, 525-552.

Pravdo, S. H., & Shaklan, S. B. (2009, July). An ultracool Star's Candidate Planet. ApJ, *700*, 623-632.

Pueyo, L., Crepp, J. R., Vasisht, G., Brenner, D., Oppenheimer, B. R., Zimmerman, N., et al. (2012, March). Application of a Damped Locally Optimized Combination of Images Method to the Spectral Characterization of Faint Companions Using an Integral Field Spectrograph. ApJS, *199*, 6.

Quillen, A. C. (2006, October). Predictions for a planet just inside Fomalhaut's eccentric ring. MNRAS, *372*, L14-L18.

Ragazzoni, R., & Farinato, J. (1999, October). Sensitivity of a pyramidic Wave Front sensor in closed loop Adaptive Optics. A&A, *350*, L23-L26.

Rice, W. K. M., Armitage, P. J., Bate, M. R., & Bonnell, I. A. (2003, March). The effect of cooling on the global stability of self-gravitating protoplanetary discs. MNRAS, *339*, 1025-1030.

Rieke, G. H., Su, K. Y. L., Stansberry, J. A., Trilling, D., Bryden, G., Muzerolle, J., et al. (2005, February). Decay of Planetary Debris Disks. ApJ, *620*, 1010-1026.

Roberts, L. C., Jr., Perrin, M. D., Marchis, F., Sivaramakrishnan, A., Makidon, R. B., Christou, J. C., et al. (2004, October). Is that really your Strehl ratio? In D. Bonaccini Calia, B. L. Ellerbroek, & R. Ragazzoni (Eds.), *Society of photo-optical instrumentation engineers (spie) conference series* (Vol. 5490, p. 504-515).

Roddier, C., Roddier, F., Stockton, A., Pickles, A., & Roddier, N. (1990, July). Testing of telescope optics - A new approach. In L. D. Barr (Ed.), *Society of photo-optical instrumentation engineers (spie) conference series* (Vol. 1236, p. 756-766).

Roddier, F. (1988, April). Curvature sensing and compensation: a new concept in adaptive optics. Appl. Opt., *27*, 1223-1225.

Roddier, F., Gilli, J. M., & Vernin, J. (1982). On the isoplanatic patch size in stellar speckle interferometry. *Journal of Optics*, *13*, 63-70.

Roddier, F., & Roddier, C. (1997, July). Stellar Coronograph with Phase Mask. PASP, *109*, 815-820.

Ronchi, V. (1964, April). Forty years of history of a grating interferometer. Appl. Opt., *3*, 437.

Rouan, D., Riaud, P., Boccaletti, A., Clénet, Y., & Labeyrie, A. (2000, November). The Four-Quadrant Phase-Mask Coronagraph. I. Principle. PASP, *112*, 1479-1486.

Rousset, G., Lacombe, F., Puget, P., Hubin, N. N., Gendron, E., Fusco, T., et al. (2003, February). NAOS, the first AO system of the VLT: on-sky performance. In P. L. Wizinowich & D. Bonaccini (Eds.), *Society of photo-optical instrumentation engineers (spie) conference series* (Vol. 4839, p. 140-149).

Sahlmann, J., Ségransan, D., Queloz, D., Udry, S., Santos, N. C., Marmier, M., et al. (2011, January). Search for brown-dwarf companions of stars. A&A, *525*, A95.

Santos, N. C., Israelian, G., & Mayor, M. (2004, March). Spectroscopic [Fe/H] for 98 extra-solar planet-host stars. Exploring the probability of planet formation. A&A, *415*, 1153-1166.

Santos, N. C., Israelian, G., Mayor, M., Rebolo, R., & Udry, S. (2003, January). Statistical properties of exoplanets. II. Metallicity, orbital parameters, and space velocities. A&A, *398*, 363-376.

Schmid, H. M., Beuzit, J.-L., Feldt, M., Gisler, D., Gratton, R., Henning, T., et al. (2006). Search and investigation of extra-solar planets with polarimetry. In C. Aime & F. Vakili (Eds.), *Iau colloq. 200: Direct imaging of exoplanets: Science techniques* (p. 165-170).

Schneider, G., & Silverstone, M. (2003, February). Coronagraphy with HST: detectability is a sensitive issue. In A. B. Schultz (Ed.), *Society of photo-optical instrumentation engineers (spie) conference series* (Vol. 4860, p. 1-9).

Schneider, J. (2012). *L'Encyclopédie des Planètes Extra-Solaires.* Available from `http://exoplanet.eu/catalog.php/` (checked for the last time on July 13th (2012))

Schneider, J., Dedieu, C., Le Sidaner, P., Savalle, R., & Zolotukhin, I. (2011, August). Defining and cataloging exoplanets: the exoplanet.eu database. A&A, *532*, A79. Available from `http://exoplanet.eu/catalog.php/` (The online database was checked for the last time on 2012, June 30th.)

Seager, S., & Mallén-Ornelas, G. (2003, March). A Unique Solution of Planet and Star Parameters from an Extrasolar Planet Transit Light Curve. ApJ, *585*, 1038-1055.

Selsis, F., Commeyras, A., Dobrijévic, M., & Martin, H. (2003, April). Atmospheric levels of NOx and O2 on the prebiotic Earth and their possible role in the origin of life. In *Egs - agu - eug*

joint assembly (p. 254).

Shack, R. B., & Platt, B. C. (1971). Lenticular Hartmann-screen. *J. Opt. Soc. Am. A*, *61*, 656.

Smith, B. A., & Terrile, R. J. (1984, December). A circumstellar disk around Beta Pictoris. *Science*, *226*, 1421-1424.

Snellen, I. A. G., de Mooij, E. J. W., & Albrecht, S. (2009, May). The changing phases of extrasolar planet CoRoT-1b. Nature, *459*, 543-545.

Soummer, R. (2005, January). Apodized Pupil Lyot Coronagraphs for Arbitrary Telescope Apertures. ApJ, *618*, L161-L164.

Soummer, R., Aime, C., & Falloon, P. E. (2003, January). Stellar coronagraphy with prolate apodized circular apertures. A&A, *397*, 1161-1172.

Soummer, R., Brendan Hagan, J., Pueyo, L., Thormann, A., Rajan, A., & Marois, C. (2011, November). Orbital Motion of HR 8799 b, c, d Using Hubble Space Telescope Data from 1998: Constraints on Inclination, Eccentricity, and Stability. ApJ, *741*, 55.

Soummer, R., Pueyo, L., & Larkin, J. (2012, August). Detection and Characterization of Exoplanets and Disks Using Projections on Karhunen-Loève Eigenimages. ApJ, *755*, L28.

Stapelfeldt, K. R., Holmes, E. K., Chen, C., Rieke, G. H., Su, K. Y. L., Hines, D. C., et al. (2004, September). First Look at the Fomalhaut Debris Disk with the Spitzer Space Telescope. ApJS, *154*, 458-462.

Sterken, C., & Manfroid, J. (1992). *Astronomical Photometry, A Guide* (Vol. 175).

Stevenson, D. J. (1982, August). Formation of the giant planets. Planet. Space Sci., *30*, 755-764.

Su, K. Y. L., Rieke, G. H., Stapelfeldt, K. R., Malhotra, R., Bryden, G., Smith, P. S., et al. (2009, November). The Debris Disk Around HR 8799. ApJ, *705*, 314-327.

Telesco, C. M., Fisher, R. S., Wyatt, M. C., Dermott, S. F., Kehoe, T. J. J., Novotny, S., et al. (2005, January). Mid-infrared images of β Pictoris and the possible role of planetesimal collisions in the central disk. Nature, *433*, 133-136.

Thalmann, C., Carson, J., Janson, M., Goto, M., McElwain, M., Egner, S., et al. (2009, December). Discovery of the Coldest Imaged Companion of a Sun-like Star. ApJ, *707*, L123-L127.

Thomas, S. J., Soummer, R., Dillon, D., Macintosh, B., Gavel, D., & Sivaramakrishnan, A. (2011, October). Testing the Apodized Pupil Lyot Coronagraph on the Laboratory for Adaptive Optics Extreme Adaptive Optics Testbed. AJ, *142*, 119.

Tingley, B., & Sackett, P. D. (2005, July). A Photometric Diagnostic to Aid in the Identification of Transiting Extrasolar Planets. ApJ, *627*, 1011-1018.

Torres, G., Konacki, M., Sasselov, D. D., & Jha, S. (2004, July). New Data and Improved Parameters for the Extrasolar Transiting Planet OGLE-TR-56b. ApJ, *609*, 1071-1075.

Trauger, J., Moody, D., Gordon, B., Krist, J., & Mawet, D. (2011, September). A hybrid Lyot coronagraph for the direct imaging and spectroscopy of exoplanet systems: recent results and prospects. In *Society of photo-optical instrumentation engineers (spie) conference series* (Vol. 8151).

Trilling, D. E., Bryden, G., Beichman, C. A., Rieke, G. H., Su, K. Y. L., Stansberry, J. A., et al. (2008, February). Debris Disks around Sun-like Stars. ApJ, *674*, 1086-1105.

Udry, S. (2010, October). Detection and characterization of exoplanets: from gaseous giants to super-Earths. In *In the spirit of lyot 2010.*

van Dam, M. A., Le Mignant, D., & Macintosh, B. A. (2004, October). Performance of the Keck

Observatory Adaptive-Optics System. Appl. Opt., *43*, 5458-5467.

Wambsganss, J. (2006). Part 4: Gravitational microlensing. In G. Meylan, P. Jetzer, P. North, P. Schneider, C. S. Kochanek, & J. Wambsganss (Eds.), *Saas-fee advanced course 33: Gravitational lensing: Strong, weak and micro* (p. 453-540).

Watkins, S. J., Bhattal, A. S., Boffin, H. M. J., Francis, N., & Whitworth, A. P. (1998a, November). Numerical simulations of protostellar encounters - II. Coplanar disc-disc encounters. MNRAS, *300*, 1205-1213.

Watkins, S. J., Bhattal, A. S., Boffin, H. M. J., Francis, N., & Whitworth, A. P. (1998b, November). Numerical simulations of protostellar encounters - III. Non-coplanar disc-disc encounters. MNRAS, *300*, 1214-1224.

Weidenschilling, S. J. (1980, October). Dust to planetesimals - Settling and coagulation in the solar nebula. Icarus, *44*, 172-189.

Wetherill, G. W. (1980). Formation of the terrestrial planets. ARA&A, *18*, 77-113.

Wolszczan, A. (1994, April). Confirmation of Earth-Mass Planets Orbiting the Millisecond Pulsar PSR B1257+12. *Science*, *264*, 538-542.

Wolszczan, A., & Frail, D. A. (1992, January). A planetary system around the millisecond pulsar PSR1257 + 12. Nature, *355*, 145-147.

Wyatt, M. C. (2008, September). Evolution of Debris Disks. ARA&A, *46*, 339-383.

Zernike, F. (1934, May). Beugungstheorie des schneidenver-fahrens und seiner verbesserten form, der phasenkontrastmethode. *Physica*, *1*, 689-704.

Zimmerman, N., Oppenheimer, B. R., Hinkley, S., Brenner, D., Parry, I. R., Sivaramakrishnan, A., et al. (2010, February). Parallactic Motion for Companion Discovery: An M-Dwarf Orbiting Alcor. ApJ, *709*, 733-740.

Appendices

Appendix A
Main program of the data reduction code

We do not provide the exact code of our main program (let alone the whole code), as it is not the point and would not help the reader in his understanding of it. Instead, we give an outline of its main steps. The steps that are marked with a `!NEW!` are added improvements of the original version of the code.

```
pro reduce_naco_nirc2_v11, cx, cy, st_ob, nd_ob, sigma, mag_L=mag_L, naco=naco,
nirc2=nirc2, basic=basic, adi_s=adi_s, adi_f=adi_f,loci_s=loci_s,loci_f=loci_f,
contrast_curve=contrast_curve, centering=centering, concat=concat


print,'!!!!!!!!!!!!!!!!!!!!!!!!!!!!!!!!!!!!!!!!!!!!!!!!!!!!!!!!!!!!!!!!!!!!!!'
print,'!!!!                          WARNING                                !!!!'
print,'Change LOCI parameters in the script with caution (advanced users only)'
print,'!!!!!!!!!!!!!!!!!!!!!!!!!!!!!!!!!!!!!!!!!!!!!!!!!!!!!!!!!!!!!!!!!!!!!!'


Definition of environment variables for NaCo and Nirc2 format


Reading information about target from its first file
-----------------------------------------------------

   Exposure time
   Number of exposures
   Filter
   Plate

Creation of a new directory with the name of the specific target, this is where
all the files created will be saved
```

```
Global parameters
-----------------

   Plate scale
   Diameter of the telescope
   Image dimension

   Filters
      J --> lambda = 1.1e-6
      H -->lambda = 1.65e-6
      K, Ks, K' --> lambda = 2.15e-6
      L'-->lambda = 3.8e-6

   FWHM = (206265*lambda)/(diameter*plsc) ; in pixels

   Filtering parameters
      cutoff_low = 4 * fwhm
      cutoff_high = 'none'


Basic treatment (if 'basic' keyword is ON)
---------------
   For Naco:
      red_naco_lyot_v3.pro
         It does all the steps described in sec. 2.4.1 and 2.4.2, and creates 2
         basic-treated datacubes, 1 for ADI: max 190 frames - computers
         usually won't have enough memory to treat a datacube greater than
         1024x1024x190, and 1 for LOCI: with all the frames but croped to keep
         only a disk of 400 px centered on the star.
   For Nirc2:
      make_ff_nirc2.pro (make flat field file if not existing)
      make_basic_nirc2_v4.pro (does all the steps in sec. 2.4.1 and 2.4.2)


Concatenation (if 'concat' = vector_concat) !NEW!
-------------
   For LOCI_s or LOCI_f -->  concat_v1.pro
         It replaces the datacube and vectors created by the basic treatment
         with theirselves but concatenated, i.e. it reassembles and resizes
         datacube to keeping only the good frames given in vector_concat.
   For ADI_s or ADI_f  -->  concat_v1.pro
         It does the same to the basic-treated datacube created for ADI (i.e.
         truncated at max. 190 frames.
```

```
Simple ADI (if 'ADI_s' keyword is ON)
----------
   adi_naco_nirc2_v5.pro
      It performs a simple c-ADI reduction.
   If contrast_curve keyword --> contrast_curve_v4.pro


Simple ADI with high-pass filter (if 'ADI_f' keyword is ON)
--------------------------------
mfilter_v4.pro
   It performs the spatial high-pass filtering, taking as parameter
   the above-defined cutoff_l.
adi_naco_nirc2_v5.pro
If contrast_curve keyword --> contrast_curve_v4.pro


LOCI (if 'LOCI_s' or 'LOCI_f' keyword is ON)
----
   Specific LOCI input parameters
   ------------------------------
      delta = 1.0 (delta in FWHM for reference image exclusion)
      truncate_init=20 (truncate the ref. image pool sorted by correlation)
      dim   = 400  (output image size)
      Na    = 100  (number of FWHM inside the optimization zone)
      g     = 1.0  (geometry of the optimization zone)
      rin_init=3  (inner radius where LOCI starts, in FWHM)
      step_init=0.5  (radial step size for the section S in FWHM)

   Parameters used for introduction of fake companions (hereafter fcp) !NEW!
   ------------------------------------------------------------------
      n_rad= 4 (number of fcp along the radius)
      n_br = 6 (number of branches of the pattern used to place our fcp)

   Run LOCI: initial pass, no fake companion
   ---------------------------------------
      If LOCI_f --> mfilter_v4.pro
      loci_adi_v19.pro
         It is classical loci. It uses dim, FWHM, rin_init, step_init,
         truncate_init, Na, g, delta, (/svd, /nnls or /bvls)
      If contrast_curve --> contrast_curve_v4.pro
```

```
   Second pass, inject fake companion at sigma * residual noise  !NEW!
   ------------------------------------------------------------
      Level of injected fake companions is estimated
      fcp_v4.pro
         It computes the snowflake pattern (cf. section 3.2.1),
         estimates the noise level and inserts the fcp (cf. section 3.2.2.).
      If LOCI_f --> mfilter_v4.pro
      loci_adi_v19
         We re-run LOCI, this time with fcp injected

   Analyze fake companion throughput => alphar(r)  !NEW!
   ------------------------------------------------
      alpha_r_v4.pro
         The ratio between the signal output by LOCI after injection of the
         fcp and the known signal of the fcp before injection are calculated
         at their respective position (cf. section 3.2.3). Its azimuthal mean
         is then calculated and used to create an interpolation of the
         attenuation pattern.

   Normalisation of the contrast curve : 5N(r)/alpha(r)  !NEW!
   ----------------------------------------------------
      contrast_curve_v4.pro
         This time it is run with keyword /alpha. It plots the initial
         contrast curve and the normalized one.

END
```